Experimentelle Physik

Dielectron Performance of the Compressed Baryonic Matter Experiment

Inaugural-Dissertation
zur Erlangung des Doktorgrades (Dr. rer. nat.)
der Naturwissenschaften im Fachbereich Physik
der Mathematisch-Naturwissenschaftlichen Fakultät
der Universität Münster

vorgelegt von
Adrian Meyer-Ahrens
aus Leverkusen

-2025-

Dekan:	Prof. Dr. Rudolf Bratschitsch
Erster Gutachter:	Prof. Dr. Anton Andronic
Zweite Gutachterin:	Prof. Dr. Tetyana Galatyuk
Tag der mündlichen Prüfung:	.....
Tag der Promotion:	.....

"That's how you know you're home, I think, no matter how far you've gone from it or how long you've been in some other place. Home is where they want you to stay longer."

Stephen King [1]

Contents

1. Introduction

Experiments in particle physics, in particular at ion colliders, are characterized by extremes: Accelerators like the Large Hadron Collider (LHC) at Conseil Européen pour la Recherche Nucléaire (CERN) with its circumference of 27 km [2] are among the largest and most complex machines built by humanity, while the objects being studied with them have diameters in the fm scale, or, in some cases, do not exhibit any spatial dimensions at all, thus spanning a gap of at least 18 orders of magnitude in size. However, not only the scales of these experiments are impressive but also the conditions in which the particles are placed with these machines: In heavy ion collisions, temperatures in the order of 10^{12} K [3] can be achieved, which is more than 100000 times higher than the temperature of the center of our sun [4]. Depending on the setup of the collision, the density of the produced matter can reach values similar to the ones most likely existing at the core of neutron stars, which are among the densest objects in the universe [5].
Another interesting aspect of these experiments is their complexity: For a successful operation, knowledge of almost every field of physics has to be utilized. From electromagnetism to accelerate and focus the ion beam, to relativity, quantum mechanics and even thermo- or hydrodynamics to describe the collision system. Detectors are based on various different mechanisms ranging from silicon to PhotoMultiplier Tubes (PMTs) and gas-filled volumes with strong electric fields. Phenomena which one might consider interesting but ultimately useless „quirks of nature“ like Cherenkov or Transition Radiation (TR) are utilized to differentiate between otherwise indistinguishable particles. Not only state-of-the-art physics is required, heavy-ion experiments are also stunning achievements in engineering, signal processing and computing. The detectors have to be sturdy but lightweight, the readout system has to be fast and precise but also operate at an environment with extreme radiation exposure, and petabytes of data have to be analyzed to find rare signals like needles in a haystack. Due to their complexity and the associated costs, only a handful of facilities for heavy-ion collision experiments exist in the world, most notably the aforementioned LHC at CERN in Switzerland/France, or the Relativistic Heavy Ion Collider (RHIC) at Brookhaven National Laboratory (BNL) in the United States. A new entry in this list will be the SchwerIonenSynchrotron (SIS) 100 at the Facility for Antiproton and Ion Research (FAIR), which is currently under construction in Darmstadt, Germany and will start operation in 2028, extending the already existing

Gesellschaft für SchwerIonenforschung (GSI) facility and providing the infrastructure for several new experiments. One of these is the Compressed Baryonic Matter (CBM) experiment, operated in the so-called „fixed-target“ mode, in which collisions are realized by shooting ion beams onto a stationary target. Its main goal is to study nuclear matter at the extreme conditions achieved in such collisions, in particular at high densities. There, the protons and neutrons in the ions dissolve, forming a state in which their constituents, the *quarks* and *gluons*, become the relevant degrees of freedom, called the Quark-Gluon Plasma (QGP). A key question which CBM aims to answer is the nature of the phase transition between the QGP and „ordinary“ nuclear matter, in which the quarks and gluons are bound in protons, neutrons or other particles.
A challenge however is that the QGP is extremely short lived, with estimated lifetimes in the order of 10^{-23} s [6, 7], as it quickly expands and cools off. It is therefore not possible to study the QGP directly, and one resorts to measuring the particles produced in the collisions and draw conclusions regarding its nature from their specific composition and properties. Since the particles range in mass from electrons ($\sim 0.5\,\mathrm{MeV/c^2}$), to pions ($\sim 140\,\mathrm{MeV/c^2}$) and even up to light nuclei such as ^{4}He ($\sim 3700\,\mathrm{MeV/c^2}$), the devices needed to detect and accurately identify them are highly complex, consisting of various specialized subsystems and need years or even decades of research and development. One might imagine needing to construct a scale which can precisely measure the weight of both a pigeon and an elephant.
The detector for the CBM experiment is no exception, comprised of eight subsystems in three different configurations and developed in time scale of 25 years between its first official collaboration meeting in 2003[1] and its realization in 2028. Two crucial methods in the development process of such a device are on the one hand simulations of the physics and the detector on the computer, and on the other hand tests of components and prototypes in the laboratory. Simulations provide the freedom to experiment with different layouts and configurations in a controlled environment, to be able to test and optimize the planned detector setup and develop and refine analysis methods before the experiment itself is constructed and operational, and to give estimates about the expected performance. Tests in laboratories are necessary to check if the assumptions made in the simulations hold true under realistic conditions, identify pit-falls and provide feedback to the detector design. As the interplay between simulations and lab tests is very important for the development process, the people involved often partake in both disciplines, as is done in this work, covering prototype tests of one of the subsystems, the Transition Radiation Detector for the CBM Experiment (CBM-TRD), as well as simulation studies of the measurements with the full foreseen detector setup.

[1] https://indico.gsi.de/event/4156/

This thesis is structured into seven chapters: After this brief introduction (Chapter 1), the theoretical background needed for the subsequent parts is layed out in Chapter 2, explaining the current understanding of strongly interacting matter at extreme conditions and focusing on thermal dielectrons as experimental probes in heavy-ion collisions. Afterwards, CBM is described in Chapter 3, showing its unique potential compared to other heavy-ion experiments and providing an overview over its various subsystems. Here, the working principle and design of the CBM-TRD is illustrated in greater detail, as it is of major importance for Chapter 4, in which the analysis of a test beam campaign conducted at Deutsches Elektronen-SYnchrotron (DESY) in 2019 using CBM-TRD prototypes is described, with the aim of the reconstruction of the energy deposited in the detector. In Chapter 5 data simulated for the entire foreseen CBM setup is analyzed in regard to the dielectron decay channel of thermal radiation. After describing the input to the simulation, various methods for the rejection of the different background sources are studied and the resulting spectra shown and compared. Finally, a summary is given in English (Chapter 6) and German (Chapter 7).

2. Theoretical Background

2.1. Strongly Interacting Matter

The so-called *strong interaction* is one of the four fundamental forces of nature, with the other ones being the *weak*, *electromagnetic* and *gravitational* interactions [8]. All except gravity can be described in the framework of the Standard Model (SM) of particle physics, in which they are realized as gauge particles (*Gauge Bosons*), carrying the forces between the interacting constituents of matter (*Quarks* and *Leptons*). In case of the strong interaction, the gauge bosons are the *Gluons*, which can couple to quarks as well as themselves. The theoretical description of the strong interaction in the SM is called Quantum Chromodynamics (QCD) [9].

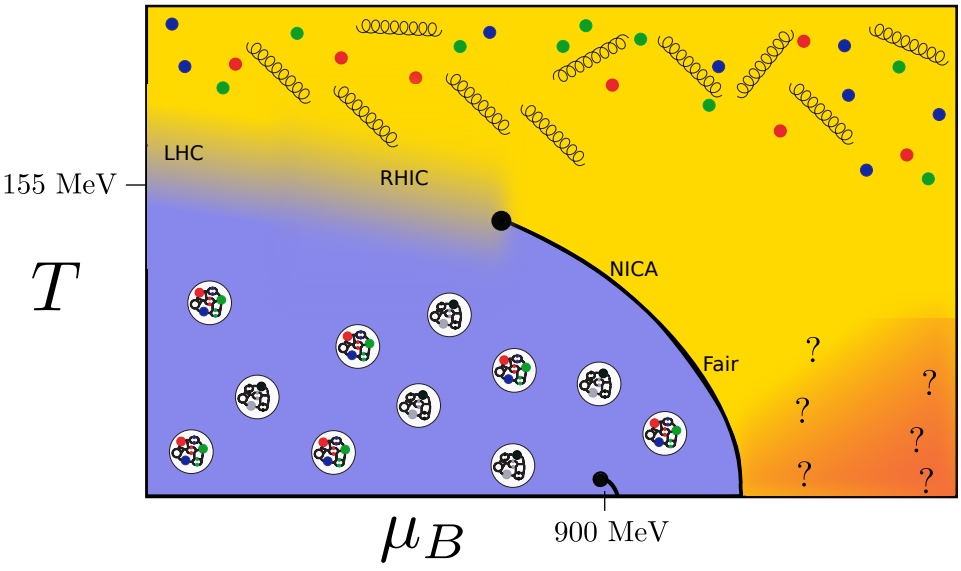

Figure 2.1.: Diagram showing the different phases of QCD matter in dependence of the temperature and baryon chemical potential μ_B [10].

For strongly interacting matter QCD predicts the existence of different phases depending on the thermodynamical properties of the given system. Figure 2.1 summarizes these in the most common representation of the QCD phase diagram, with temperature and baryon chemical potential μ_B on the axes. At low temperatures and μ_B, quarks and gluons are always bound in

color neutral states, namely hadrons. However, for larger values of temperature and/or μ_B the density of quarks per hadronic volume can become so high that individual quarks cannot be identified as partners in specific bound states, thus forming a deconfined medium of color-charged quarks and gluons, the QGP. For lower temperatures but very high baryon chemical potentials on the other hand, QCD predicts a so-called *color superconducting* state of matter [11].

Of particular interest are not only the different confined and deconfined phases themselves, but also the transitions between them, which are studied extensively both with theoretical and experimental methods. Currently best understood is the transition between QGP and hadron gas at vanishing μ_B, hence along the y-axis of the diagram in Figure 2.1. Here, lattice QCD calculations predict a smooth crossover between the two phases at a pseudo-critical temperature $T_c \sim 156\,\text{MeV}$ [12]. Experimentally, this region of the phase diagram has been (and still is) explored most prominently by A Large Ion Collider Experiment (ALICE) at the LHC, where the temperature at which quarks and gluons in a cooling and expanding QGP form hadrons again (the so-called *chemical freeze-out*) has been determined to be $T_{\text{cf}} = 156.5 \pm 1.5\,\text{MeV}$ at vanishing μ_B, in remarkable agreement with the lattice results [3].

When moving away from the y-axis into the regime of finite μ_B, making quantitative predictions becomes increasingly difficult, since direct simulations with lattice QCD are not possible due to the so-called *sign problem*. Hence, results at finite μ_B have to be obtained by extrapolation for which various techniques are being studied [10]. For large μ_B, several model calculations predict a first order phase transition, which would imply the existence of a critical endpoint, where the crossover and the first order phase transition meet [13]. Both the critical point and the first order phase transition have yet to be confirmed experimentally, which might be possible at future experiments at Nuclotron-based Ion Collider Facility (NICA) and FAIR [14].

2.2. Heavy-Ion Collisions

To study the phase transitions mentioned in the previous section in a lab environment, ultra-relativistic heavy ion collisions are currently the only viable approach to create the extreme conditions necessary for these transitions to occur. These collisions can be realized either by accelerating two ion beams in opposite directions and letting them collide head-on (*collider mode*), or accelerating only one ion beam and shooting it onto a stationary target (*fixed-target mode*).

2.2.1. Spacetime Evolution

The spacetime evolution of such a collision is depicted in Figure 2.2. What

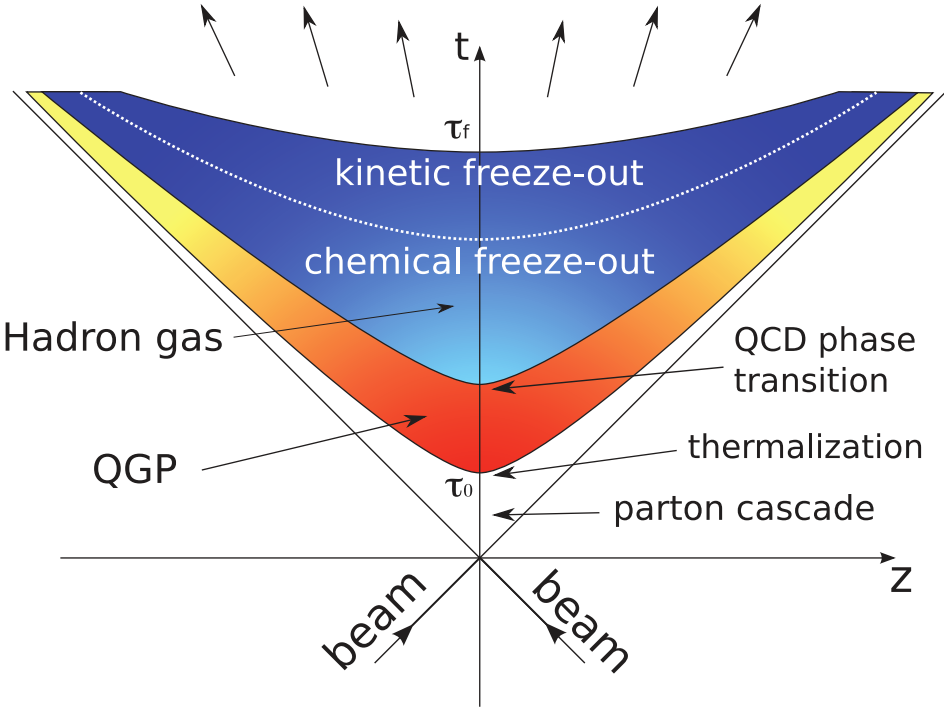

Figure 2.2.: Diagram of the spacetime evolution of a heavy ion collision. Even though both colliding nuclei are denoted as *beam*, the figure applies also to collisions in fixed-target mode as it is just a change of the reference system [15].

starts with two colliding Lorentz-contracted nuclei ends with large quantities of newly produced as well as already existing particles flying in various directions. In between, the matter will undergo several stages in very short time with typical timescales from the initial collision to kinetic freeze-out being in the order of several tenths of fm/c [6, 7].

After the initial collision, a hot and dense system of quarks and gluons is formed, which at first is not in thermal equilibrium. The particle production at this stage can be described with different frameworks such as the *parton cascade* or the *color glass condensate* model [16]. In any case, the matter thermalizes rapidly with an equilibration time of $\tau_{\text{therm}} < 1\,\text{fm/c}$, as indicated by results from RHIC [17]. This locally thermalized, deconfined matter of quarks and gluons is what is usually referred to as QGP [18]. The QGP will subsequently expand and cool down in a way which can be described by relativistic perfect-fluid hydrodynamics, until it undergoes a phase transition to hadronic matter [16]. As discussed in Section 2.1, the nature of this phase

transition and the temperature at which it occurs depends on the baryon chemical potential, which itself depends on the collision energy (see Section 2.2.2). After the phase transition, the hadrons gas continues to expand and cool down. At first, the hadrons still undergo both elastic and inelastic collisions with each other. Due to the continuous expansion, the mean free path of the particles λ_{mfp} increases, and along with it the collision timescale $\tau_{\mathrm{coll}} \sim \lambda_{\mathrm{mfp}}$. Once the timescale of inelastic collisions becomes larger than the expansion timescale $\tau_{\mathrm{coll,in}} \geq \tau_{\mathrm{exp}}$, the so-called *chemical freeze-out* is reached and inelastic collisions cease (dotted white line in Figure 2.2). At this point the abundances of the hadrons are *frozen* as elastic collisions may only change their kinetic parameters. Subsequently also these are fixed at the *kinetic* (or *thermal*) *freeze-out* when $\tau_{\mathrm{coll,el}} \geq \tau_{\mathrm{exp}}$ [16].

2.2.2. Mapping the Phase Diagram

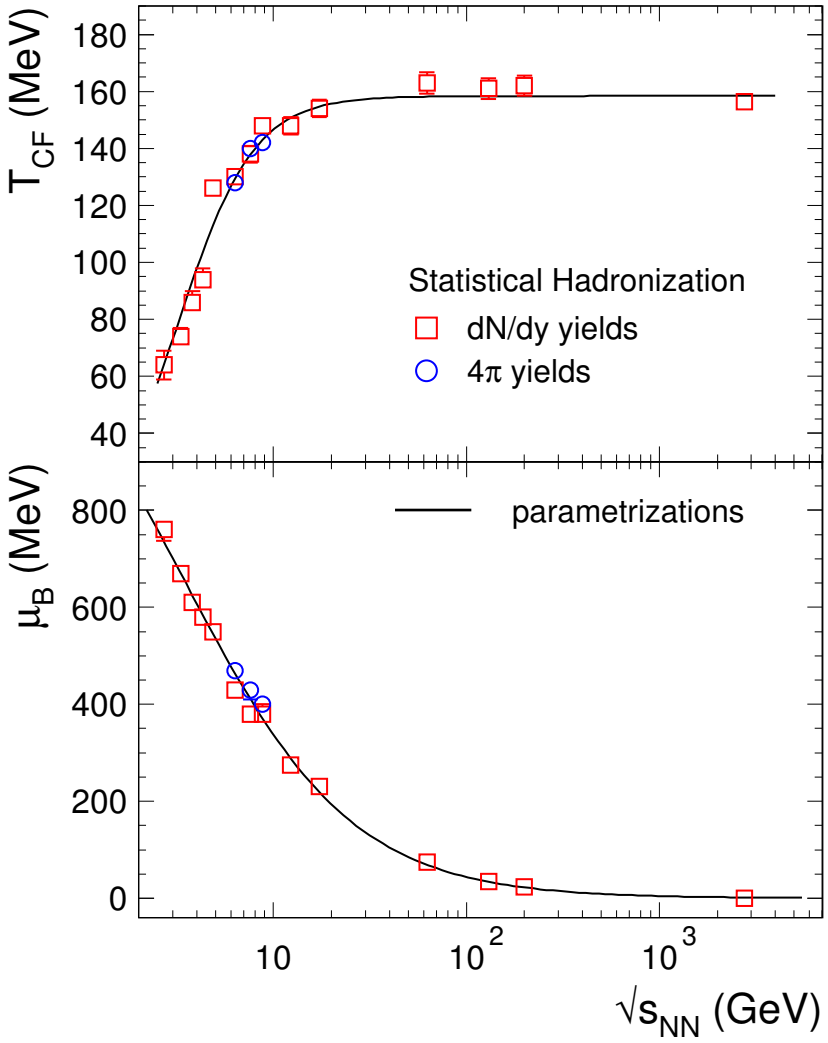

Figure 2.3.: Temperature (upper panel) and baryon chemical potential (lower panel) at chemical freeze-out in dependence of the collision energy, as obtained with the Statistical Hadronization Model (SHM) [3].

To probe different regions of the QCD phase diagram, the main free parameter for experimentalists to vary is the collision energy. Figure 2.3 shows its influence on μ_B and T_{cf} extracted with the SHM. As can be seen in the lower panel, the baryon chemical potential decreases with increasing energy, which is caused by the collisions becoming more and more transparent. This means that at high energies the colliding nuclei pass through each other without being slowed down and therefore the matter created in the central region has

to consist of (mostly) the same number of quarks and anti-quarks. At lower energies on the other hand, baryons from the incoming nuclei are stopped, leading to an increased baryon number of the created matter [16]. As shown in the upper panel of Figure 2.3, the T_{cf} first rises with the collision energy, as more energy is brought into the system, and then saturates. It is important to note that the statistical model can only determine the temperature at chemical freeze-out and not at previous stages such as the QGP or the hadron gas before its yields are frozen. This is possible using dilepton yields, as described in Section 2.3.[2]

2.3. Dileptons in Heavy-Ion Collisions

Lepton pairs stemming from the decays of virtual photons ($\gamma^* \rightarrow l^+l^-$ with $l = e$ or μ) are typically referred to as *dileptons* and exhibit various properties which make them an especially useful probe in heavy-ion collisions. For once, photons do not partake in the strong interaction and are therefore able to leave the medium in which they are produced without further scattering. In contrast to real photons, virtual photons (and thus dileptons) also carry additional information with their invariant mass [19]. Another important feature of dileptons is the fact that they are produced throughout the whole evolution of the collision, which, together with their ability to leave the medium, gives the possibility to probe properties of the hot and dense matter at various evolution stages [20].

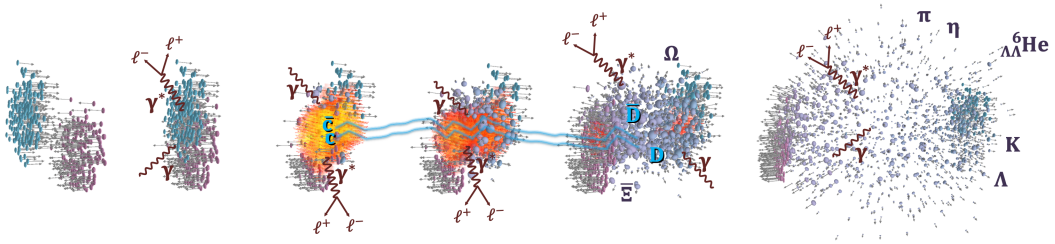

Figure 2.4.: Simulation showing dilepton emission at various stages of a heavy ion collision [21].

Figure 2.4 shows dilepton production at different stages of the fireball evolution in a heavy ion collision. At first, in the initial hard collisions, the so called Drell-Yan process may occur, in which a quark of one nucleon annihilates with an antiquark of another nucleon thus forming a virtual photon (or Z boson) and subsequently a dilepton pair: $q\bar{q} \rightarrow \gamma^* \rightarrow l^+l^-$ [22]. After

[2] Note: This should not imply that one method is superior to the other, but rather that they are complementary.

thermalization, thermal dileptons are radiated by the QGP as well as the hot and dense hadronic matter after the phase transition. Finally, many dileptons are produced in the decays of various meson decays after the chemical freeze-out.

2.3.1. Thermal Dilepton Production

In thermal equilibrium, the local dilepton emission rate can be calculated as follows [19, 23]:

$$\frac{\mathrm{d}N_{ll}}{\mathrm{d}^4x\mathrm{d}^4q} = -\frac{\alpha_{\mathrm{EM}}^2}{M^2\pi^3} L(M^2) f^B(q_0;T)\,\mathrm{Im}\Pi_{\mathrm{EM}}(M,q;\mu_B,T) \tag{2.1}$$

Here, α_{EM} is the ElectroMagnetic (EM) coupling constant, $M^2 = q_0^2 - q^2$ the invariant mass squared of the virtual photon, $L(M^2)$ the lepton phase-space factor, $f^B(q_0;T)$ the thermal Bose distribution in the rest frame of the emitting matter, and $\mathrm{Im}\Pi_{\mathrm{EM}}$ the imaginary part of the EM current-current correlation function, which is usually referred to as *EM spectral function*. While rather complex, the EM spectral function can be measured accurately in the vacuum since it is directly proportional to the cross section of $e^+e^- \to$ hadrons (see Figure 2.5).

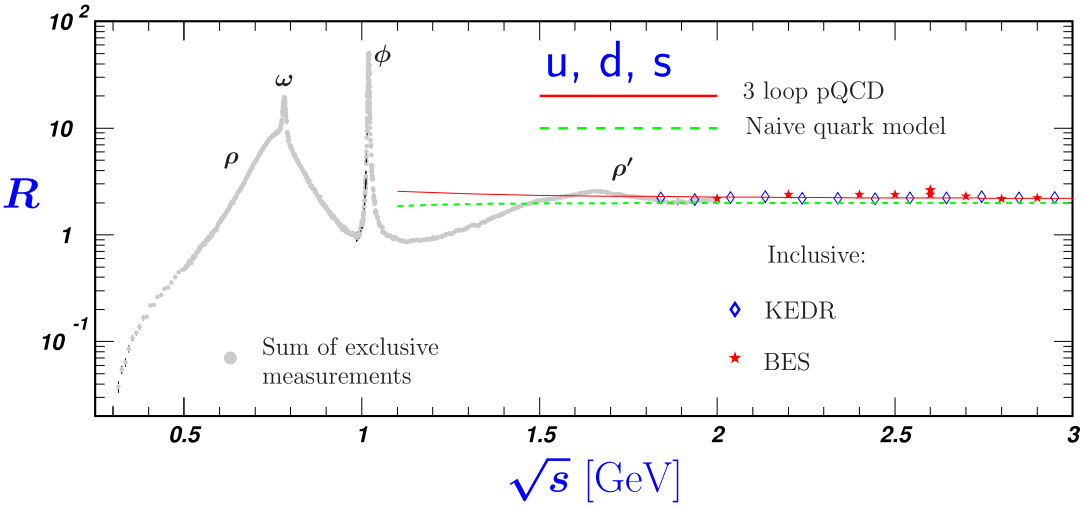

Figure 2.5.: Ratio $R = \sigma(e^+e^- \to \text{hadrons})/\sigma(e^+e^- \to \mu^+\mu^-)$ plotted against the collision energy [24][edited].

As visible in Figure 2.5, the low-mass vector mesons ρ, ω and ϕ dominate the EM spectral function in the Low Mass Region (LMR) ($M \lesssim 1.1\,\mathrm{GeV}$), while in the Intermediate Mass Region (IMR) ($M \sim 1.5 - 3\,\mathrm{GeV}$) the function exhibits a continuum structure resulting from $q\bar{q}$ annihilation at such short distances that it can be well described perturbatively [19].

In case of heavy-ion collisions, the EM spectral function is no longer measured in the vacuum, but placed inside strongly interacting hot and dense matter giving rise to in-medium modifications. In the IMR continuum these modifications are expected to be small and thus, the dilepton emission rate in this mass region depends mostly on the bulk properties of the fireball and their respective time evolution. In the LMR, on the other hand the spectral shape is expected to be significantly modified by the surrounding medium [19].

2.3.2. Dilepton Spectroscopy

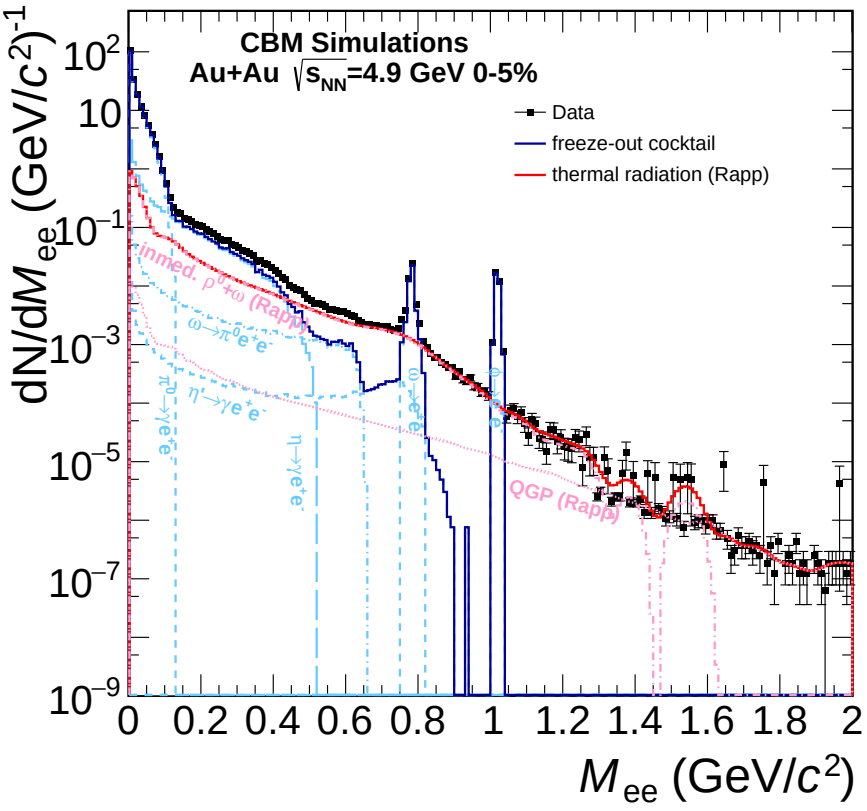

Figure 2.6.: Simulated dielectron spectrum for Au+Au collisions at $\sqrt{s}$ = 4.9 GeV (0-5% most central). The light blue dashed lines indicate the individual contributions of the different meson decays to the freeze-out cocktail, the pink dashed lines differentiate between the parts of the thermal radiation coming from the QGP and from hot and dense hadronic matter [14, 25].

The expected dielectron spectrum for Au+Au collisions at a center-of-mass energy of $\sqrt{s}$ = 4.9 GeV is shown in Figure 2.6. The main contribution comes

from decays of various mesons formed at chemical freeze-out (blue curve) and is therefore typically referred to as *freeze-out cocktail*. Since the amount of dielectrons coming from Drell-Yan processes and open-charm are expected to be small in this energy range, the main additional source is thermal radiation (red curve). Thus, subtracting the freeze-out cocktail gives direct access to the thermal dielectron spectrum produced as described in Section 2.3.1 which can then be used to extract information about the collision *before* freeze-out [26]. For once, dileptons can be used as a fireball thermometer utilizing

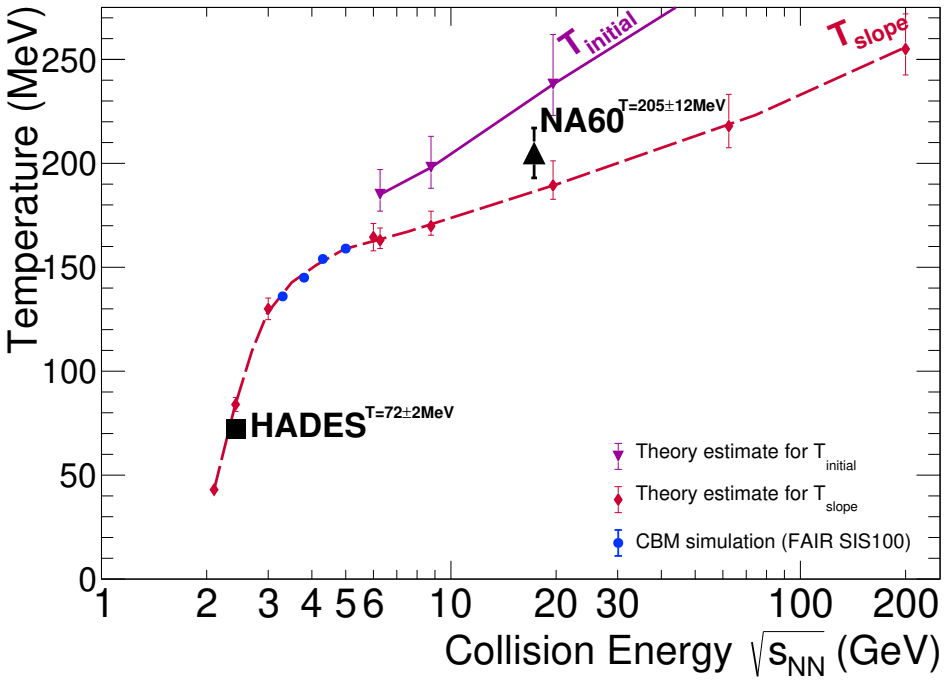

Figure 2.7.: Compilation of measured and estimated fireball temperatures shown as a function of the collision energy. The blue circles indicate future measurements possible with the CBM experiment [27].

the IMR of the spectrum: Due to the smallness of the medium modifications of the EM spectral function in that range ($\mathrm{Im}\Pi_{\mathrm{EM}} \propto M^2$) a nonrelativisitic approximation gives:

$$\frac{\mathrm{d}N_{ll}}{\mathrm{d}M} \propto (MT)^{3/2} e^{-M/T} \tag{2.2}$$

which holds true for about $1.5\,\mathrm{GeV/c^2} \leq M \leq 2.5\,\mathrm{GeV/c^2}$. As can be seen in Figure 2.6, the thermal radiation from the QGP dominates in this range. Therefore, with a fit of the form of Equation 2.2 it is possible to extract the temperature of the deconfined medium before hadronization [26]. By measuring the temperature at different collision energies one can access the „caloric“curve of the medium as shown in Figure 2.7.

The models used for the calculation of T_{slope} (for $\sqrt{s} < 6\,\mathrm{GeV}$ see Ref. [28], for $\sqrt{s} > 6\,\mathrm{GeV}$ see Ref. [26]) do not include a first-order phase transition and thus predict a monotonous increase of the temperature with the collision energy. If the caloric curve on the other hand would exhibit a plateau in a certain energy region, it would provide direct evidence for a first-order phase transition [29]. As shown with the black symbols in Figure 2.7 only two data points for T_{slope} are currently available, measured by the High Acceptance Dielectron Spectrometer (HADES) and the North Area (NA)60 experiment, respectively. Further data will be provided by CBM, as indicated with the blue circles, which may provide evidence for or against the existence of a first-order phase transition in the energy region of $3.2\,\mathrm{GeV} \leq \sqrt{s} \leq 4.9\,\mathrm{GeV}$ [27].

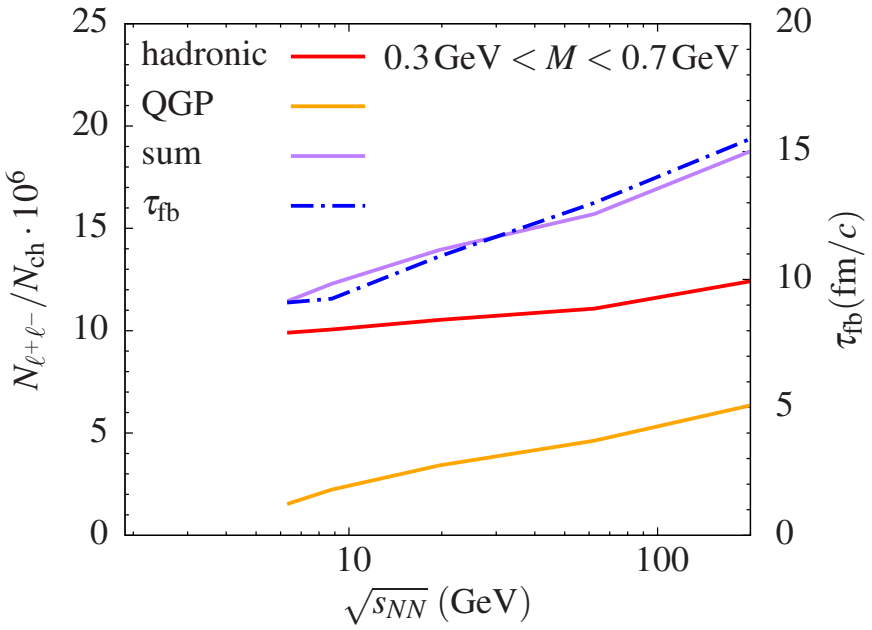

Figure 2.8.: Simulated dielectron excess yield integrated in the mass range of $M = 0.3 - 0.7\,\mathrm{GeV}/c^2$ as a function of the collision energy. The contributions from the hot and dense hadronic matter and the QGP are shown individually (red and orange line, respectively), as well as their sum (purple line). The dot-dashed blue line corresponds to the fireball lifetime, using the y-axis on the right [26].

Another important parameter that can be probed with dileptons is the lifetime of the created fireball. As the thermal radiation is produced throughout its whole evolution, the total yield is directly connected to the lifetime and can be extracted by an integral over an appropriate mass range. Figure 2.8 shows the yields from the thermal components of simulated dielectron spectra in the mass range of $M = 0.3 - 0.7\,\mathrm{GeV}/c^2$ as a function of the collision energy (left y-axis) and the lifetime τ_{fb} of the fireball (right y-axis).

Evidently, the sum of both thermal contributions tracks the lifetime rather well, with an accuracy better than 10% [26]. Further applications for dilepton spectroscopy include the determination of the pressure of the emitting source via transverse momentum spectra [29, 30] or investigation of potential chiral symmetry restoration through the chiral mixing of the ρ_0 and a_1 mesons [31, 32].

3. CBM Experiment at FAIR

The CBM experiment is a future fixed-target heavy-ion experiment which is currently under construction at FAIR in Darmstadt. The new SIS100 acceler-

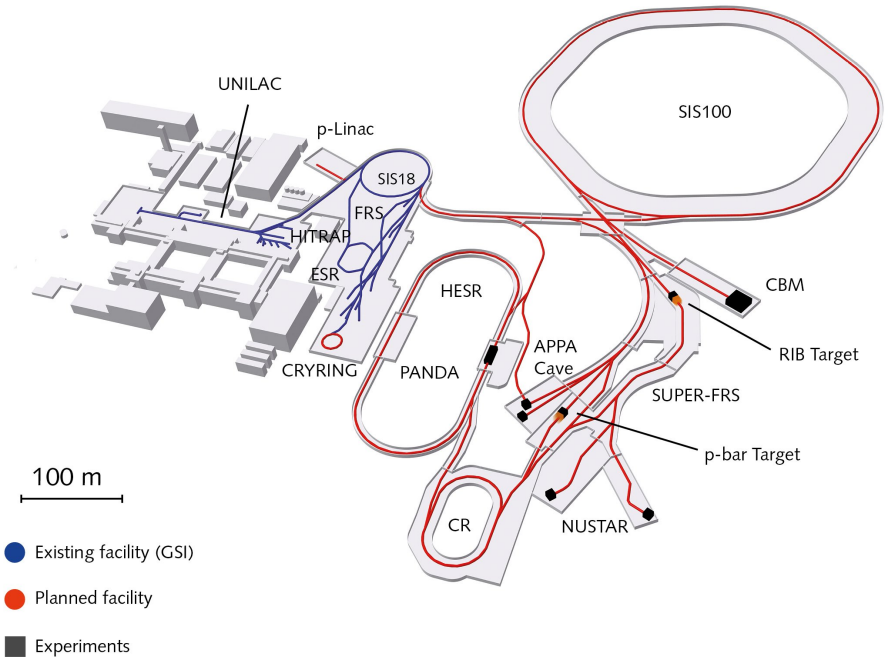

Figure 3.1.: Schematic view of the existing GSI and planned FAIR facility with the CBM experiment located directly downstream of the SIS100 accelerator [33].

ator will deliver ion beams to CBM with energies up to 29 GeV for protons, up to 11 AGeV for Au, and up to 14 AGeV for nuclei with $Z = N$ [34]. At these beam energies, models predict that densities up to 8 times nuclear saturation density ρ_0 can be reached, allowing CBM to study the high net-baryon density region of the QCD phase diagram [14] (see Figure 2.1). A second key feature of the experiment are the high interaction rates of up to 10 MHz, which will give CBM the ability to measure very rare probes, such as thermal dileptons (see Section 2.3.2), with sufficient statistics [14]. As shown in Figure 3.2,

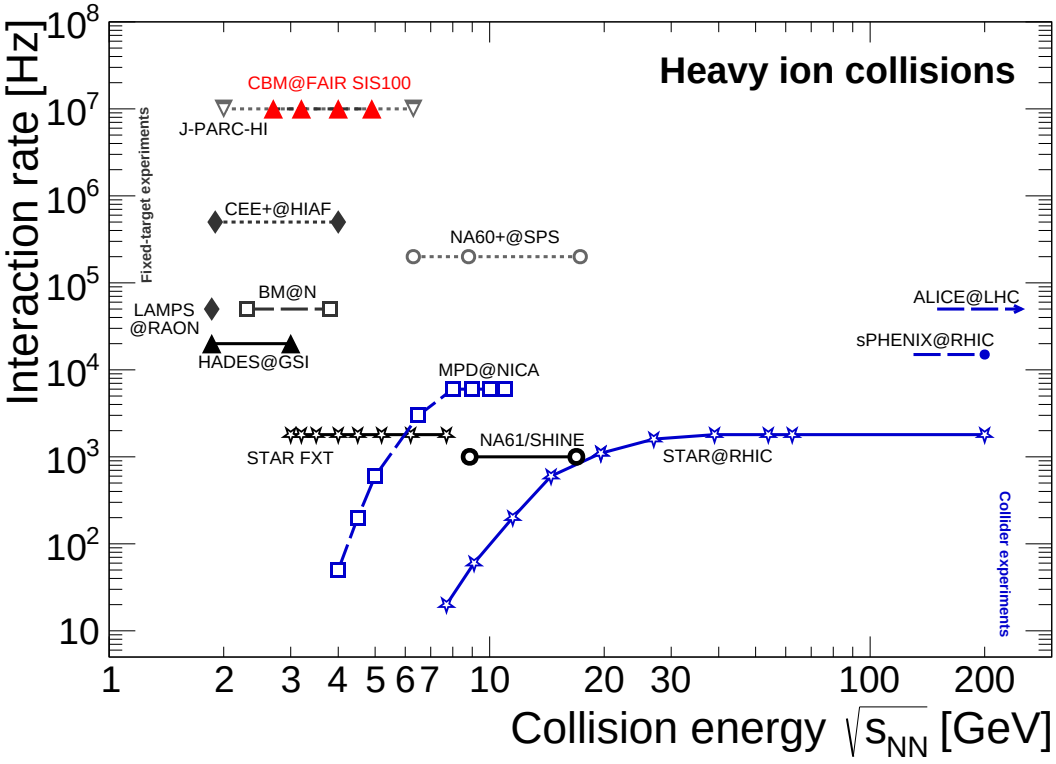

Figure 3.2.: Interaction rates of planned and existing heavy ion collision experiments. CBM (marked in red) is located in the top left at low/moderate energies and high interaction rates [27].

the foreseen interaction rates at CBM are orders of magnitude higher than most existing or planned heavy ion experiments [27]. Naturally, these interaction rates also propose a challenge for the detector and readout systems, as the required rate capability poses a constraint on any design parameter. In the following section (Section 3.1) , an overview of the planned detector for CBM with its various subsystems is given. Subsequently (Section 3.2), one of the subdetectors, the CBM-TRD, is described in greater detail since it is the main focus in the analysis and simulation of Chapter 4.

3.1. CBM Detector

The CBM detector consists of several subsystems, as is shown in Figure 3.3. The setup has a modular design, allowing for exchange or removal of single subdetectors depending on the specific measurement, with the foreseen setup configurations being the electron, hadron and muon setup. The setup relevant for this thesis is the electron setup, which comprises the Micro Vertex Detector (MVD), Silicon Tracking System (STS), Ring Imaging Cheren-

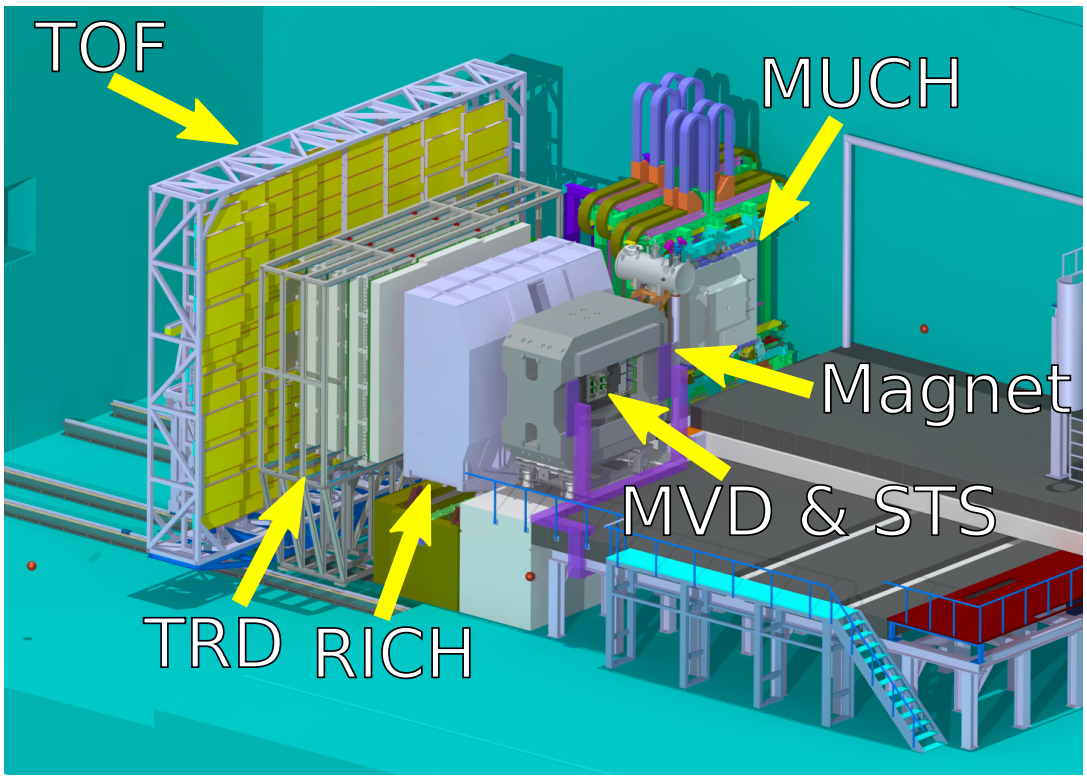

Figure 3.3.: Computer Aided Design (CAD) drawing of the CBM detector in its configuration for electron measurements. The Ring Imaging Cherenkov (RICH) detector is inserted between the magnet and Transition Radiation Detector (TRD), while the Muon Chamber (MUCH) is in parking position. The foreseen Forward Spectator Detector (FSD) will be located downstream of the Time-Of-Flight System (TOF) and is not shown here. The beam enters the setup from the right.

kov (RICH), Transition Radiation Detector (TRD) and Time-Of-Flight System (TOF) [35]. In the following, a brief overview of these subsystems will be given:

Micro Vertex Detector (MVD)

The first downstream detector is the MVD, a silicon pixel detector based on the CMOS-MAPS technology. It is located inside the target vacuum chamber, with a distance of 8 cm to the target and consists of 4 equidistant layers, as shown in Figure 3.4. Its main tasks are the extension of the momentum reconstruction of the STS (see below) of charged particles down to $\sim 300\,\mathrm{MeV/c}$, and secondary vertex reconstruction of weak decays. In dielectron measurements, the MVD is especially useful for the rejection of e^+e^- pairs from pho-

ton conversions and π^0 Dalitz decays based on their decay topology due to its high spatial precision of $\sim 5\,\mu m$ [36].

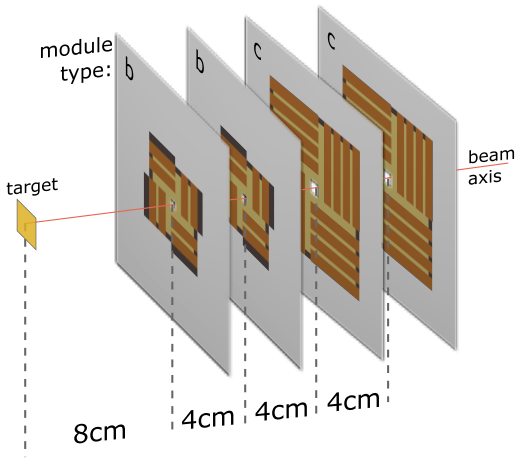

Figure 3.4.: Sketch of the MVD, consisting of four layers placed 8 cm behind the target [36].

Silicon Tracking System (STS)

The STS is CBM's main tracking device. It is positioned behind the MVD, still in the magnetic field but outside of the target vacuum chamber. As shown in Figure 3.5, the STS consists of 8 layers of silicon strip detectors and has an aperture of polar angles θ from 2.5° to 25°. It is designed to provide a momentum resolution of $\Delta p/p \approx 1\,\%$ at a trajectory finding efficiency higher than 95 % for particle momenta above 1 GeV/c [37].

Ring Imaging Cherenkov (RICH) Detector

The RICH detector is located behind the STS, outside of the magnetic field. Its purpose is electron identification and pion suppression at particle momenta below 10 GeV/c by making use of the produced (or lack thereof) Cherenkov radiation of charged particles passing through the detector volume, which is filled with CO_2 as radiator gas. The Cherenkov radiation is then focused and reflected onto a photon detector plane consisting of Multi-anode PhotoMultiplier Tubes (MaPMTs) as shown in the left of Figure 3.6. Below their Cherenkov threshold of $p = 4.65\,\text{GeV/c}$ in CO_2, pions do not produce Cherenkov radiation, but even above the threshold the RICH can contribute to the pion suppression since the Cherenkov opening angle θ_c depends on the Lorentz factor of the particle [38].

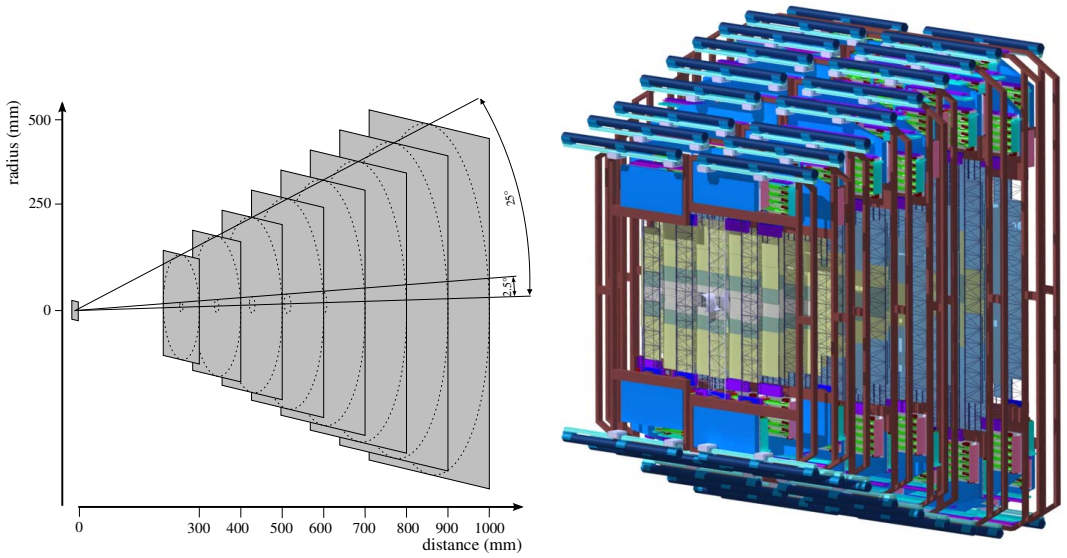

Figure 3.5.: Left: Schematic drawing of the STS with its 8 layers of silicon strip detectors starting at a distance of 30 cm behind the target. The aperture of polar angles θ between 2.5° and 25° is shown. Right: CAD rendering of the full STS including mounting and cooling systems [37].

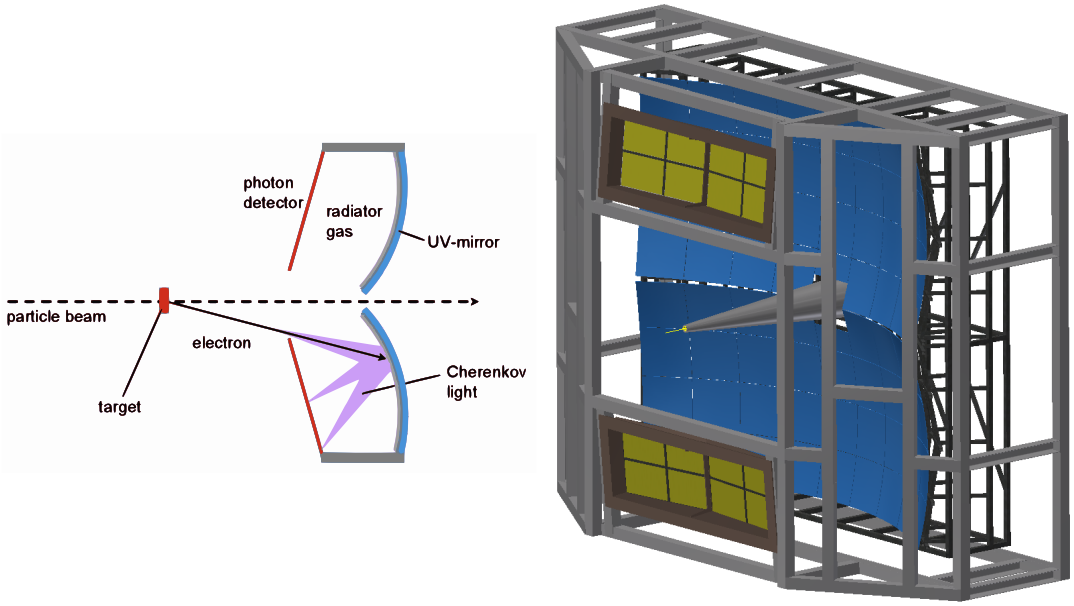

Figure 3.6.: Left: Schematic drawing of the RICH detector. Electrons from the collision produce Cherenkov light in the radiator gas, which is reflected on a photon detector plane via mirrors. Right: CAD rendering of the RICH detector with its mechanical support frame [38].

Transition Radiation Detector (TRD)

Behind the RICH detector the TRD is situated. Its primary task is providing additional electron identification and pion suppression, complementing the RICH. Furthermore, it can be used for intermediate tracking as well as the identification of nuclear fragments. It consists of Multi Wire Proportional Chambers (MWPCs) and PolyEthylene (PE) foam foil radiators, in which the transition radiation is produced [35]. Since the TRD is of major importance for this thesis, its design and working principles are described in more detail in Section 3.2.

Time-Of-Flight System (TOF)

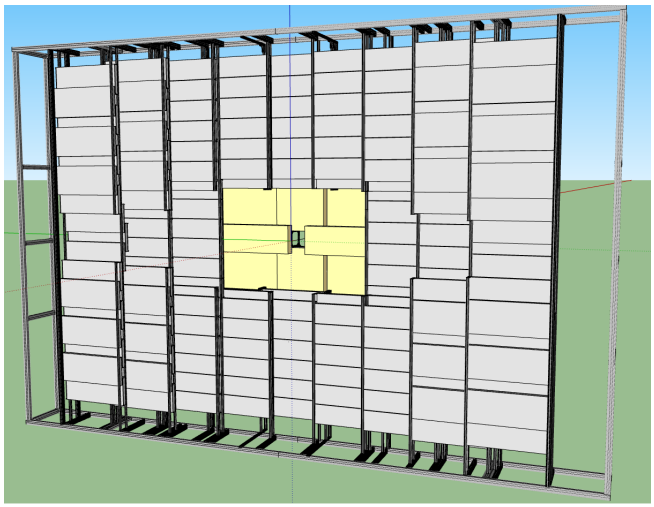

Figure 3.7.: Front view of the TOF detector. Each rectangular module contains several Multi-Gap Resistive-Plate Chambers (MRPCs) [39].

The last detector in the CBM electron setup is the TOF, which measures the arrival time of charged particles with a high resolution in the order of $\sim 60\,\mathrm{ps}$. Together with the momentum information provided by the STS and a reference start time T_0 the mass of the particles can be calculated, allowing their identification. The detector is based on MRPCs, which are arranged in different modules to form a wall as shown in Figure 3.7 [39].

3.2. Transition Radiation Detector for CBM

As stated in the previous section, the CBM-TRD is one of the experiment's subdetectors which is used for electron identification, intermediate tracking and identification of nuclear fragments. It comprises four identical layers

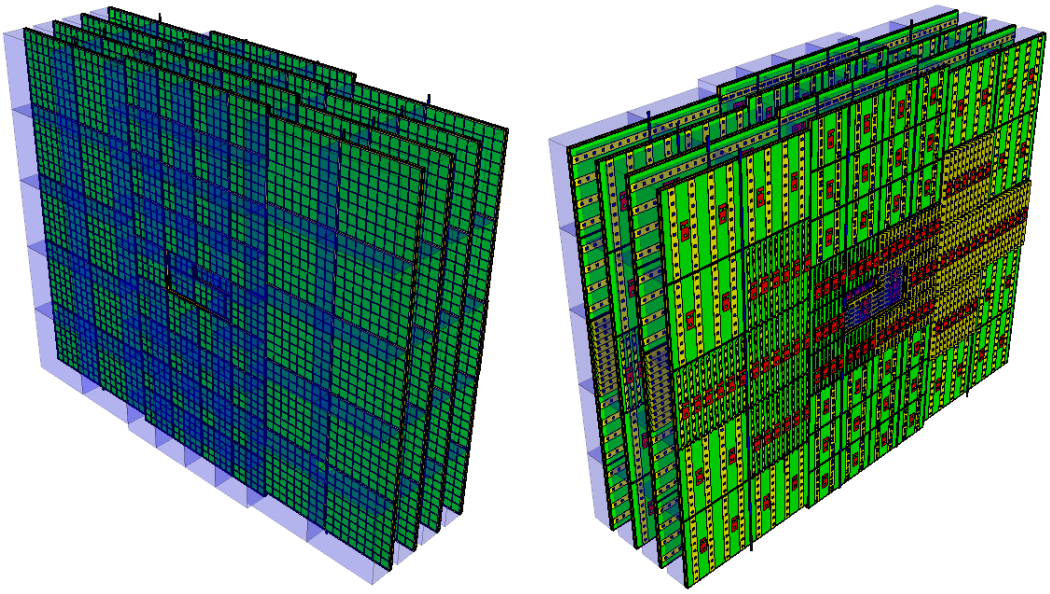

Figure 3.8.: Front view (left) and back view (right) of the CBM-TRD. The radiator boxes are shown as transparent blue boxes and the readout chambers in green. On the back view also the readout electronics are sketched [35].

with modular structure, where each module consists of a radiator and a readout chambers (see Figure 3.8). The general working principle of a CBM-TRD module is illustrated in Figure 3.9. When passing through the readout chamber, charged particles deposit energy via their specific energy loss $\langle dE/dx \rangle$, which is already slightly different for electrons and pions. The radiator in front of the readout chamber causes the traversing electrons to produce TR, while pions and heavier particles with the same momentum do not. By measuring the TR in addition to specific energy loss in the detector gas, electrons can be distinguished from other particles [35].

3.2.1. Readout Chamber

The readout chamber of the CBM-TRD is a so-called Drift-MWPC, which is a gas filled volume with wire grids creating an electric field. The field can be separated into the drift region, where the field lines are parallel, and the amplification region, where they bend towards the anode wires (see Figure 3.9). The detector volume is filled with Xe mixed with CO_2 as a quenching component in a ratio of 85:15 [35].

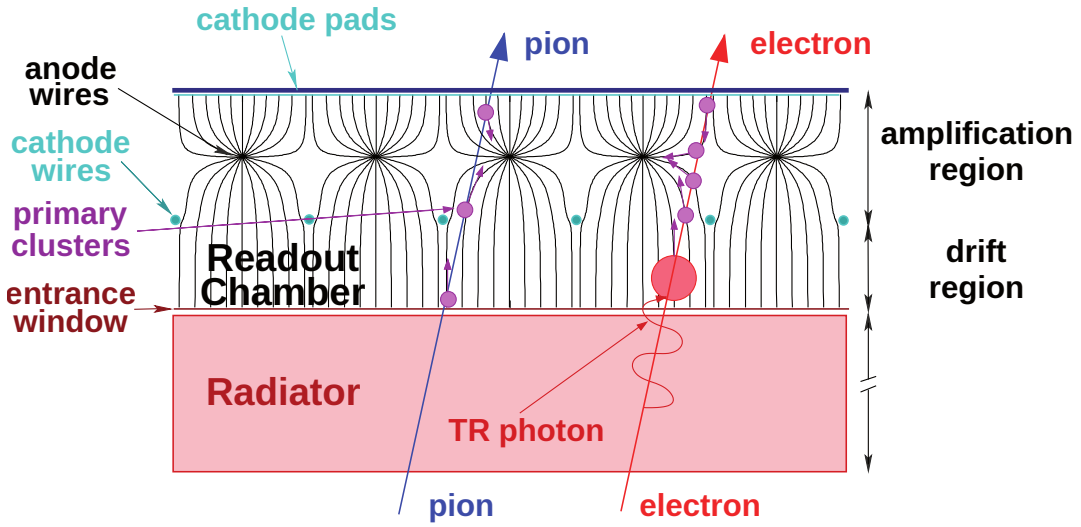

Figure 3.9.: Illustration of the working principle of a CBM-TRD module: Charged particles in general deposit energy in the readout chamber, while electrons additionally generate TR when passing through the radiator. Thus, they can be distinguished via the total energy deposition in the detector [35][edited].

3.2.1.1. Energy Loss of Charged Particles in the Detector Gas

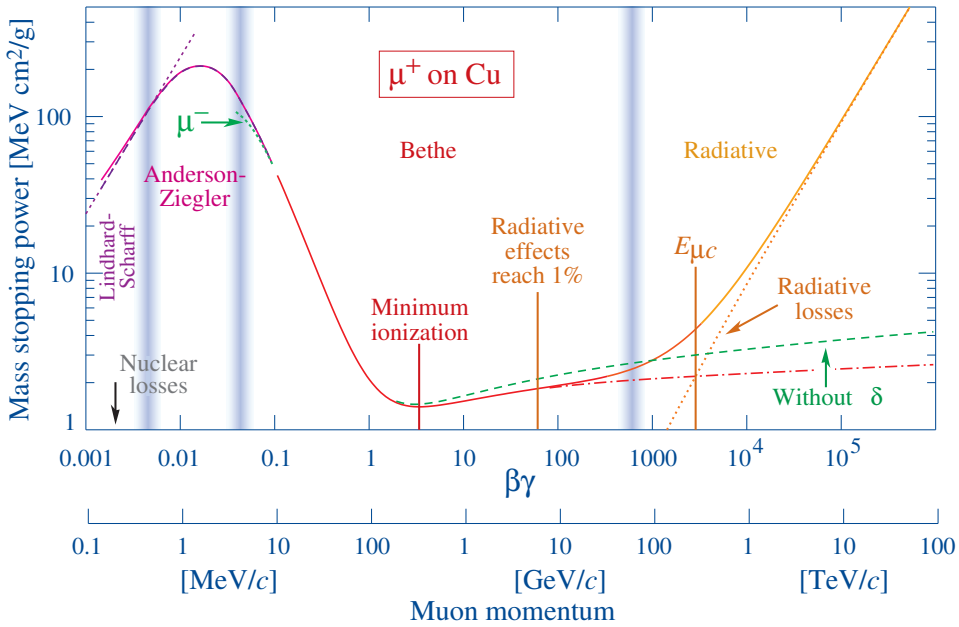

Figure 3.10.: Specific energy loss $\langle dE/dx \rangle$ of a muon passing through Copper ($Z = 29$) in dependence of its $\beta\gamma$. The region in which Equation 3.1 is valid is the *Bethe region* between $0.1 \lesssim \beta\gamma \lesssim 1000$ [24].

A charged particle traversing through a material will deposit energy through single collisions with shell electrons, which can be described by the *Bethe-Equation* [24]:

$$\left\langle -\frac{\mathrm{d}E}{\mathrm{d}x} \right\rangle_{\mathrm{col}} = Kz^2 \frac{Z}{A} \frac{1}{\beta^2} \left[\frac{1}{2} \ln \frac{2m_e c^2 \beta^2 \gamma^2 W_{\max}}{I^2} - \beta^2 - \frac{\delta(\beta\gamma)}{2} \right], \tag{3.1}$$

which is valid in a range of $0.1 \lesssim \beta\gamma \lesssim 1000$ where $\beta = \frac{v}{c}$ and $\gamma = \frac{1}{\sqrt{1-\beta^2}}$. For further variables and constants see Table 3.1.

Table 3.1.: Variables and constants used in 3.1. All values are taken from [24].

Symbol	Definition	Value or (usual) units
K	$4\pi N_{\mathrm{A}} r_e^2 m_e c^2$	$0.31\,\mathrm{MeV\ mol^{-1}\ cm^2}$
N_{A}	Avogadro's number	$6.02 \times 10^{23}\,\mathrm{mol^{-1}}$
r_e	classical electron radius	2.82 fm
$m_e c^2$	electron mass $\times c^2$	0.51 MeV
z	charge number of incident particle	
Z	atomic number of absorber	
A	atomic mass of absorber	$\mathrm{gmol^{-1}}$
$W_{\max}$	maximum energy transfer to an electron in a single collision	MeV
I	mean excitation energy	eV
$\delta(\beta\gamma)$	density effect correction	

The energy loss per distance described by Equation 3.1 is shown in Figure 3.10, for a muon passing through Copper. Particles with a $\langle \mathrm{d}E/\mathrm{d}x \rangle$ close to the minimum at $\beta\gamma \sim 3$ are called Minimum Ionizing Particles (MIPs) [24].

For electrons the energy loss through collisions is slightly different compared to other charged particles, since they have a small mass and are not distinguishable from the shell electrons they collide with. It can be written as follows [40][3]:

$$\left\langle -\frac{\mathrm{d}E}{\mathrm{d}x} \right\rangle_{\mathrm{col}} = \frac{K}{2} \frac{Z}{A} \frac{1}{\beta^2} \left[\ln \frac{\tau^2(\tau+2)}{2(I/m_{\mathrm{e}}c^2)^2} + F(\tau,\beta) - \delta(\beta\gamma) \right]. \tag{3.2}$$

Here τ is the kinetic energy of the incident electron and $F(\tau,\beta)$ an additional correction function which is different for electrons and positrons. For completeness it can be found in Equation A.7.

[3] Note: Shell correction omitted here because it is relevant only at low incident particle energies.

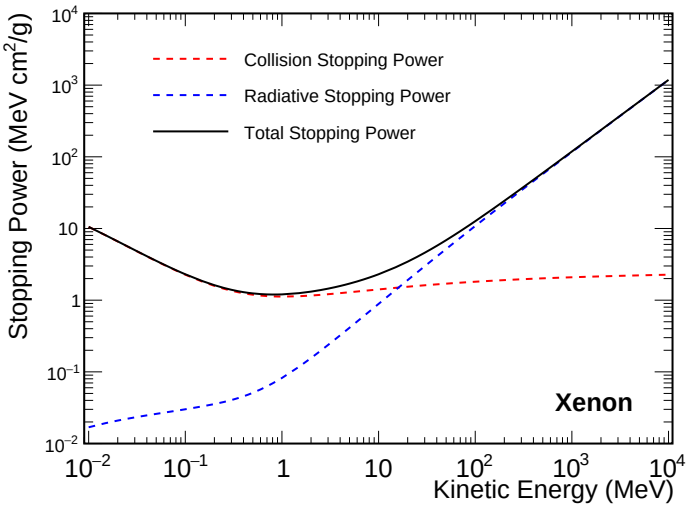

Figure 3.11.: Energy loss of electrons in Xenon as a function of the kinetic energy. The dashed lines show the contributions of collision energy loss and bremsstrahlung. Data from the NIST data base [41].

Secondly, electrons deposit energy not only through collisions but also by radiating bremsstrahlung due to being decelerated by the coulomb field of the atomic nuclei. The energy loss by bremsstrahlung is described by [42]

$$\left\langle -\frac{\mathrm{d}E}{\mathrm{d}x} \right\rangle_{\text{brem}} = 4\alpha N_A \frac{Z^2}{A} \left(\frac{e^2}{4\pi\epsilon_0 mc^2} \right)^2 E \ln \frac{183}{Z^{1/3}}, \tag{3.3}$$

where α represents the fine structure constant. Hence, the total energy loss of electrons is the sum of the losses through collisions and bremsstrahlung:

$$\left\langle -\frac{\mathrm{d}E}{\mathrm{d}x} \right\rangle_{\text{tot}} = \left\langle -\frac{\mathrm{d}E}{\mathrm{d}x} \right\rangle_{\text{col}} + \left\langle -\frac{\mathrm{d}E}{\mathrm{d}x} \right\rangle_{\text{brem}}. \tag{3.4}$$

Note that this is also true for heavier charged particles, but due to the inverse dependence on square of the particles' mass in Equation 3.3, bremsstrahlung only becomes significant at very high momenta (see Figure 3.10). For electrons passing through the Xenon in the detector volume on the other hand, radiative loss by bremsstrahlung surpasses the loss by collisions already at a kinetic energy of $\sim 15\,\mathrm{MeV}$, as shown in Figure 3.11. However, even though electrons with momenta in the GeV/c range *lose* most energy through bremsstrahlung, the *deposited* and thus *measured* energy in the detector gas still mainly comes from ionization loss, as demonstrated in Ref. [43].

3.2.1.2. Signal Generation

As described above, the energy of a particle is deposited through several single collisions with shell electrons of the Xenon atoms, ionizing the detector gas. The freed electrons will then drift along the electric field lines to the anode wires while the positively charged Xenon ions move towards the entrance window which functions as a cathode. Close to the anode wires, the electric field strength increases with a $1/r$ dependence, significantly accelerating the electrons and thus giving them the ability to ionize gas atoms. The newly freed electrons will subsequently ionize more atoms, resulting in an avalanche [40]. The current from the avalanche induces a mirror charge on

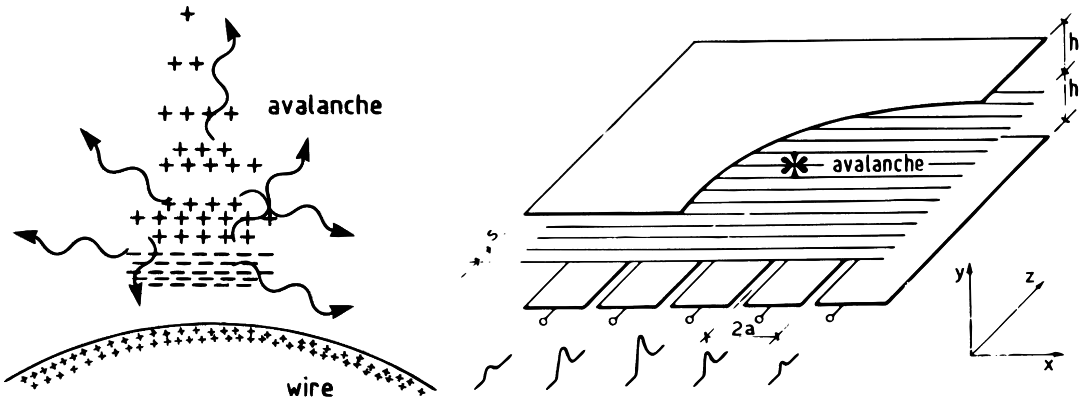

Figure 3.12.: Left: Illustration of a charge avalanche developing in the vicinity of an anode wire. Right: Signal in the cathode pad plane induced by the avalanche current at the anode wire (Both [44]).

the cathode pad plane which is read out. Due to the segmentation of the cathode plane into rectangular pads, the position of the avalanche (and thus of the incident particle) can be determined by comparing the signal amplitude on neighboring pads (see Figure 3.12, right) [44].

3.2.1.3. CBM-TRD Readout Chamber Properties

As stated above, the active detector volume of the readout chamber is separated into an amplification and a drift region, which can be seen in Figure 3.13. While the amplification region is essential for the signal generation, the 5 mm drift region is added to extend the width of the gas volume and thus, increase the probability of TR absorption. Furthermore it reduces the effect of deformations of the entrance window on the gas gain, since it also acts as the drift potential plane. The entrance window is a 25 µm thick Kapton foil with an 0.05 µm aluminum coating on one side. To limit deformations caused by pressure variations it is supported by a carbon fiber grid, as shown in Figure 3.14 [35].

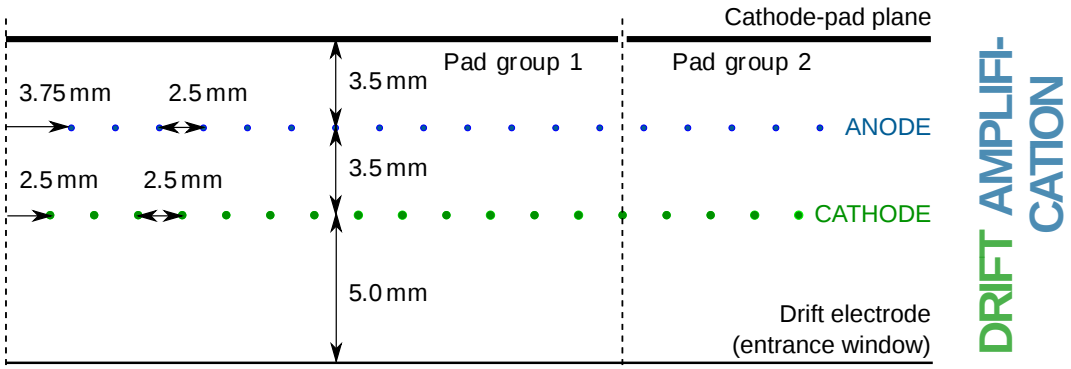

Figure 3.13.: Schematic drawing of a readout chamber of the CBM-TRD showing the width of the amplification and drift region, as well as the wire pitch of anode and cathode wires [35][edited by P. Kähler].

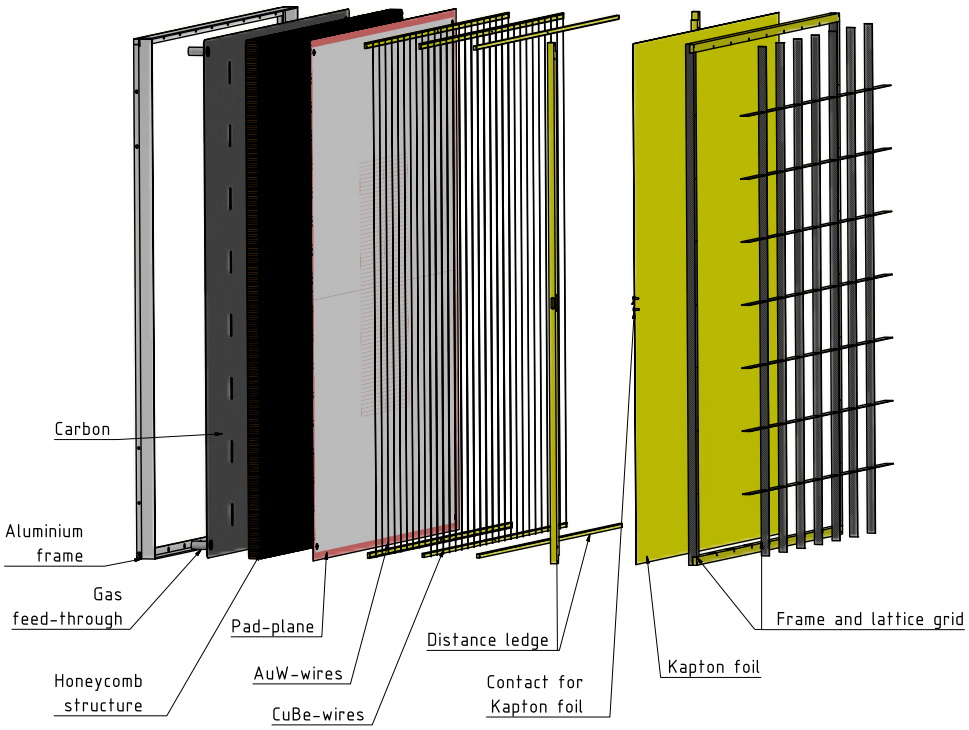

Figure 3.14.: Explosion view of a readout chamber of the CBM-TRD: For mechanical stability, the cathode pad plane is glued onto a honeycomb carbon fiber sandwich, which is supported by a aluminum frame. The Kapton entrance window is stabilized by a carbon fiber grid to minimize deformations due to external and internal pressure variations [35].

3.2.2. Radiator

Even though the specific energy loss of electrons is already slightly different to other (heavier) charged particles, the main separation capability of the CBM-TRD stems from the TR produced in the radiator [35].

3.2.2.1. Transition Radiation

When a relativistic charged particle passes the boundary between two media with different dielectric constants, its Coulomb field readjusts itself resulting in the emission of so-called TR [45] . The double differential energy spectrum

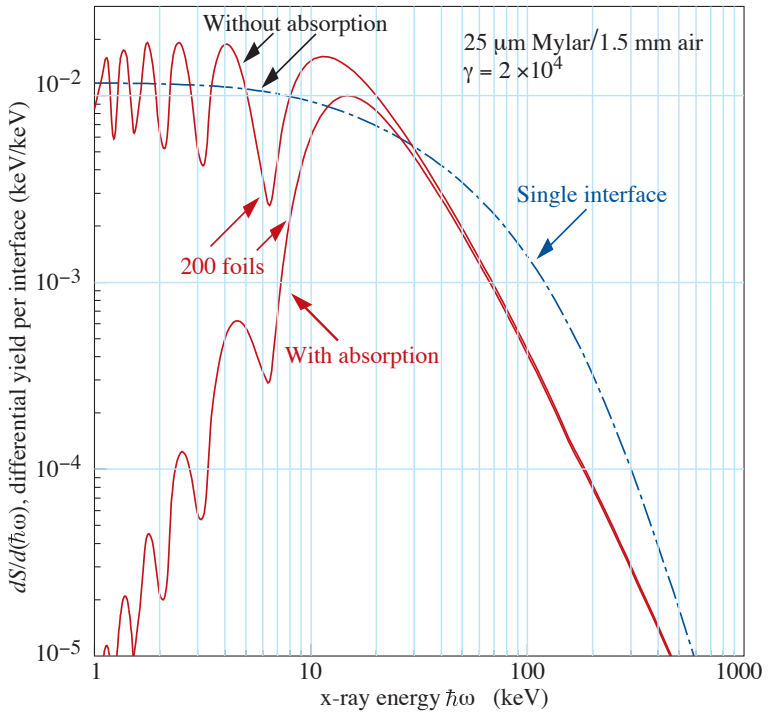

Figure 3.15.: TR photon spectra per interface for a stack of 200 Mylar foils with a thickness of 25 μm each. The dashed line shows the yield for single interfaces, while for the solid lines interference effects are taken into account. The used Lorentz factor of $\gamma = 2 \times 10^4$ corresponds to an electron momentum of ~ 10 GeV/c [24, 46].

of the emitted radiation can be described by [45]:

$$\frac{\mathrm{d}^2 W}{\mathrm{d}\omega \mathrm{d}\Omega} = \frac{\alpha}{\pi^2}\left(\frac{\theta}{\gamma^{-2}+\theta^2+\xi_1^2} - \frac{\theta}{\gamma^{-2}+\theta^2+\xi_2^2}\right), \tag{3.5}$$

with θ being the emission angle and $\xi_i^2 = \omega_{Pi}^2/\omega^2$ where ω_{Pi} is the plasma frequency of the medium i. Equation 3.5 is valid for $\gamma \gg 1$ and $\xi_1^2, \xi_2^2 \ll 1$

and $\theta \ll 1$. The plasma frequency of a medium is given by [47]:

$$\omega_P = \sqrt{\frac{4\pi\alpha n_e}{m_e}} \approx 28.8\sqrt{\rho\frac{Z}{A}}\text{eV}. \tag{3.6}$$

Here n_e denotes the electron density of the medium.
The TR is emitted with a very small opening angle to the trajectory of the particle, with

$$\theta \approx \sqrt{\gamma^{-2} + \xi_2^2} \approx \frac{1}{\gamma}. \tag{3.7}$$

A particle passing through a foil of a certain material will produce TR when entering and also when leaving the foil again, leading to interference of the emitted radiation. This is accounted for by introducing a correction factor to Equation 3.5 [47]:

$$\left(\frac{\mathrm{d}^2W}{\mathrm{d}\omega\mathrm{d}\Omega}\right)_{\text{foil}} = \left(\frac{\mathrm{d}^2W}{\mathrm{d}\omega\mathrm{d}\Omega}\right)_{\text{interface}} \cdot 4\sin^2(\phi_i/2) \tag{3.8}$$

with the phase ϕ_i, which can be approximated by [47]:

$$\phi_i \approx \frac{(\gamma^{-2} + \theta + \xi_i^2)\omega l_i}{2\beta c}. \tag{3.9}$$

The impact of interference on the emitted radiation can be seen in Figure 3.15. Furthermore, absorption of the produced photons in the radiator material itself has to be taken into account. As shown in Figure 3.15, the lowest energy photons are suppressed, leading to a peak in the effective yield at around 15 keV. The exact location and form of the peak will depend on the properties of a given radiator, which will be discussed in the following section.

3.2.2.2. Transition Radiation for Particle Detection

Due to its strong dependence on the γ factor and its small emission angle, TR is commonly used in particle detectors as a tool to separate electrons from other, heavier particles. However, since the TR yield for a single interface is still relatively small even for highly relativistic electrons, multiple foils are stacked together in so-called radiators, which may contain up to a few hundreds of interfaces and thus strongly increase the amount of produced TR per particle.

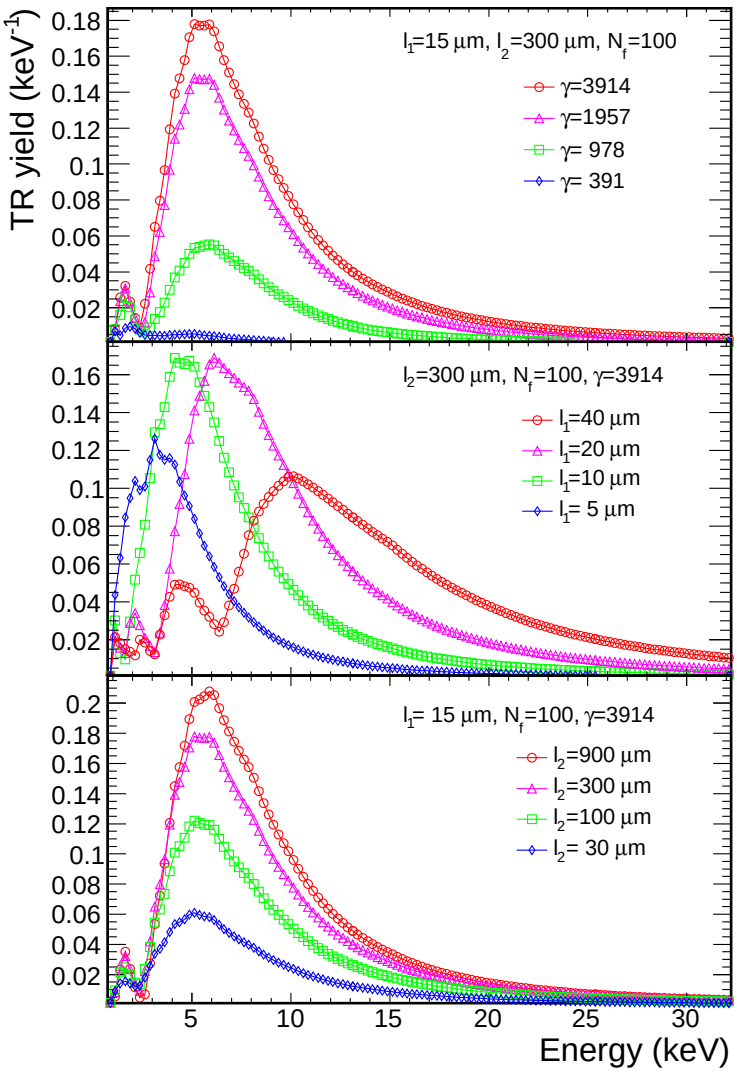

Figure 3.16.: TR yield for a foil radiator with 100 layers in dependence of the particles' Lorentz factor (top panel), foil thickness l_1 (middle panel) and foil spacing l_2 (bottom panel). The Lorentz factors in the top panel correspond to electrons with momenta of 2, 1, 0.5, and 0.2 GeV/c, respectively [47].

In Figure 3.16 produced TR spectra for a radiator consisting of 100 foils are shown as function of various parameters. The upper panel illustrates the dependence of the yield on the Lorentz factor of the incident particle. While almost no TR is produced for low values of γ, the yield increases notably after the production onset at $\gamma \simeq 1000$. The foil thickness l_1 on the other hand does not only influence the amount of TR generated, but also the hardness of the spectrum (see middle panel of Figure 3.16). Hence, this parameter can be optimized to produce as many photons as possible which are able to leave the radiator but are still detected in the readout chamber as the ab-

sorption length generally increases with energy. Finally, the bottom panel of Figure 3.16 shows the dependence of the TR yield on the foil spacing l_2. Similar as for increasing γ, the yield first rises with l_2 and then saturates, while the onset is not as threshold-like as for the dependence on γ [47].

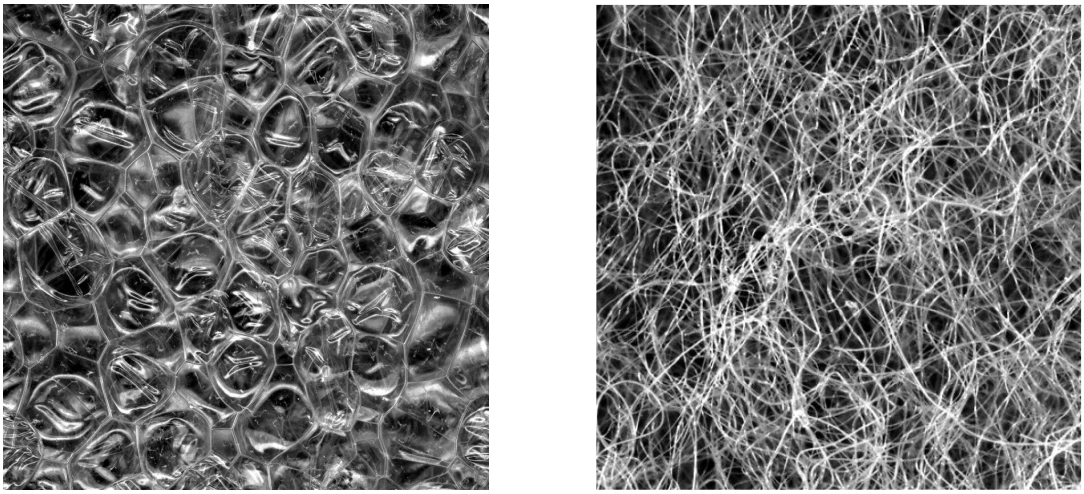

Figure 3.17.: Left: Microscopic images of a $19 \times 19\,\mathrm{mm}^2$ polyethylene foam foil (left) and a $10 \times 10\,\mathrm{mm}^2$ polypropylene fleece sheet (right) (Both [35]).

The calculations for Figure 3.16 were carried out for regular radiators, in which foils with identical thickness l_1 are evenly spaced with the same distance l_2. A different approach are so-called irregular radiators, consisting of materials with foam or fiber structures which naturally contain transitions between different media (see Figure 3.17). Since the foil thickness, spacing, and number of transitions vary inside an irregular radiator, calculations for the TR spectra are carried out using average parameters $\langle l_1 \rangle$, $\langle l_2 \rangle$ and $\langle N_f \rangle$. Furthermore an efficiency factor is applied to model the loss in performance as a result of reduced constructive interference due to the irregular structure [35, 47]. Advantages of irregular radiators are that they are generally easier and cheaper to produce and maintain than regular radiators with comparable numbers of foils.

3.2.2.3. CBM-TRD Radiator Properties

For TR generation, the CBM-TRD uses irregular PE foam foil radiators. Each of these consists of a stack of 146 PE foam foil mats housed inside a Rohacell HF71 box with a width of 30 cm (see right image of Figure 3.18). Furthermore, 7 additional mats fill the 1.5 cm deep gaps in the carbon grid in front of the entrance window of the readout chamber as shown in the left image in Figure 3.18. In both cases, the foam mats are held in place using polymer filaments [35].

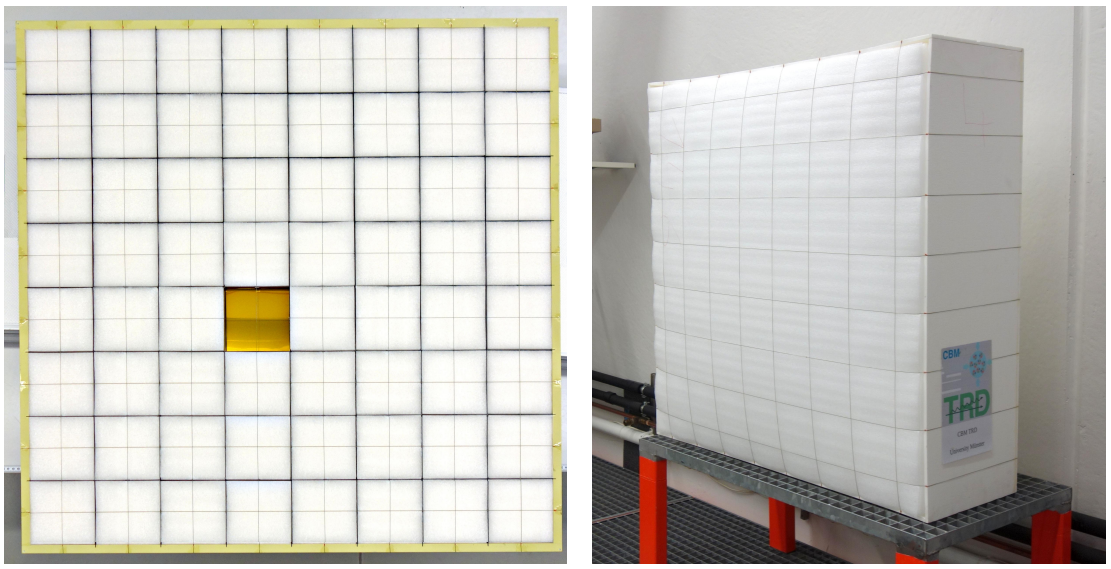

Figure 3.18.: Left: Front view of a CBM-TRD readout chamber. The quadratic gaps in the carbon grid are filled with PE foam foil mats. One gap is left empty here to also show the entrance window. Right: Photograph of a radiator box made of Rohacell and filled with PE foam foil mats (Both [35]).

3.2.3. CBM-TRD Layout

The CBM-TRD consists of four detector layers, each comprised of 56 individual detector modules of varying sizes and cathode pad granularities. To keep the hit rate per pad in the desired range of $\lesssim 100\,\mathrm{kHz}$, the pads in the inner zone have to be smaller in order to account for the higher particle flux in this area. Thus, there are four different types of modules with different pad layouts, as summarized in Table 3.2. The arrangement of these modules is shown in Figure 3.19. With a pad width of 0.68 cm (or 0.67 cm, respectively) the desired position resolution $\sim 300\,\mu\mathrm{m}$ can be reached. However, as the rectangular pads have considerably larger heights, this resolution can only be achieved in one direction. Therefore, the modules in the second and fourth detector layer are rotated by 90° [35].

Table 3.2.: Number of pads and their respective sizes of different CBM-TRD module types [35].

Module type	Pads	Height (cm)	Width (cm)	Area (cm^2)
1	2560	1.75	0.68	1.18
3	640	6.75	0.68	4.56
5	3456	4.00	0.67	2.67
7	1152	12.00	0.67	8.00

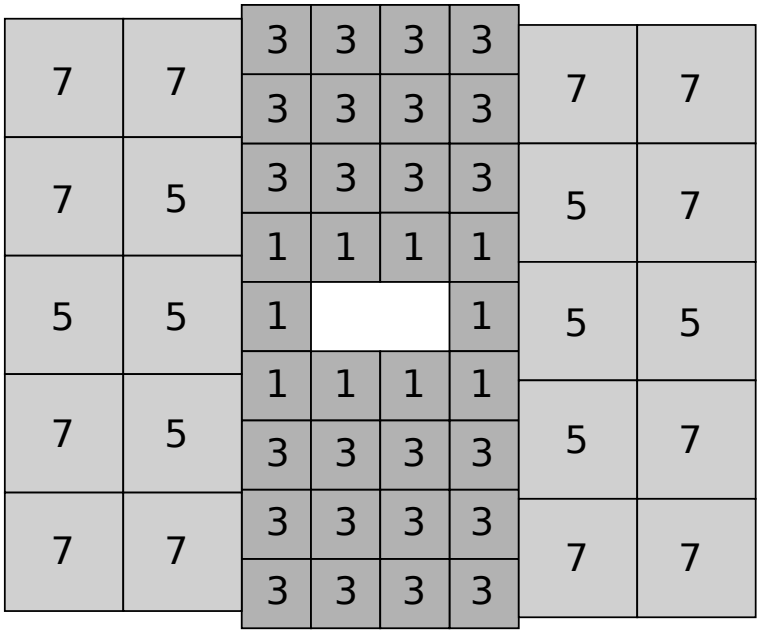

Figure 3.19.: Layout of one layer of the CBM-TRD. The numbers denote the different module types [35].

3.2.3.1. CBM-TRD 2D Inner Zone

To enhance the position resolution in the inner zone of the detector, an addendum to the technical design report of the CBM-TRD was proposed and approved (Ref. [48]), replacing the rectangular pad geometry of module type 1 (see Table 3.2) with triangular shaped pads. By appropriately combining the charge shared on these triangular pads, it is possible to extract highly resolved position information in both x **and** y direction from the same detector layer, providing the means for the CBM-TRD to be used as a stand alone tracking device [48]. Though the addendum has been approved in 2023, all simulations and calculations for this thesis are carried out using the layout from the original technical design report (Ref. [35]), as they were started before the addendum's approval and the full integration of software like e.g. geometry files, reconstruction and analysis into the main `cbmroot` release was not yet completed. It is reasonable to expect that an improvement in position resolution and possible applications of the CBM-TRD stand alone tracking station may only further enhance the results of the analysis carried out in Chapter 5.

4. Radiator Measurements @DESY 2019 Test Beam

In September 2019 the CBM-TRD groups from Frankfurt and Münster conducted a test beam campaign at DESY, using a pure electron beam for testing of various aspects of the detector prototypes and readout electronics. One element of particular interest was the generation of TR in the radiator and its dependence on the radiator thickness. In this chapter, the test beam campaign will be discussed with regard to the radiator characterization, by describing the used measurement setup, the data analysis methods and results.

4.1. Test Beam Setup

The DESY facility in Hamburg provides three dedicated test beam areas for external users, which can be irradiated with electron and positron beams. The user is able to individually activate and deactivate the beam generation for their respective test beam area, as well as to set a beam momentum between 1 and 6 GeV/c, rendering the facility an ideal environment for testing of the CBM-TRD prototypes.

4.1.1. Beam Generation

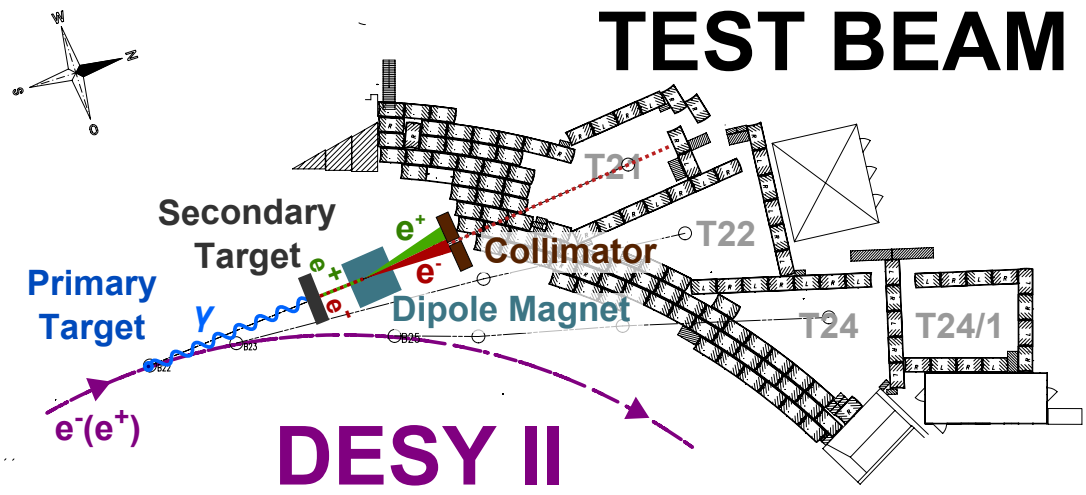

Figure 4.1.: Schematic drawing of the beam generation procedure for the three test beam sites (T21, T22 and T24) at the DESY II accelerator. For simplicity it is only drawn for test beam area T21 [49].

Figure 4.1 schematically shows the procedure in which the electron or positron beam for the test beam sites are generated. Electrons are stored in the 292.8 m long DESY II synchrotron for two of its magnet cycles (160 ms) after which they are either dumped or supplied to the Positron-Elektron-Tandem-Ring-Anlage (PETRA) III storage ring, and new electrons are injected. During each magnet cycle, the particles are accelerated from their minimum energy of 0.45 GeV to the maximum of 6.3 GeV and subsequently decelerated back down to 0.45 GeV. Inside the DESY II line, carbon fiber targets with a width of 7 µm can be moved into the beam orbit to generate bremsstrahlung. As sketched in Figure 4.1, these photons will subsequently hit a secondary target, producing e^+e^- pairs via pair production. For this, different Cu and Al plates and wires with widths ranging from 1 to 4 mm are available as secondary targets, which can be selected by the user to control the particle rate. The generated electrons and positrons then travel through the field of a dipole magnet, fanning out the particles by charge and momentum, after which they pass through a collimator. Thus, by setting the magnetic field strength and polarity accordingly, the user is able to select the momentum of the particles and switch between electrons and positrons. Since neutral particles are not deflected by the magnetic field and therefore pass through the collimator, a kink in the beam line is introduced to reject all particles traveling on a straight path [49].

4.1.2. Detector Setup

One of the main aims of the measurement campaign was to characterize the TR yield of the PE foam radiator foreseen for the CBM-TRD and investigate its dependence on the radiator width. For this, the setup shown in Figure 4.2 was assembled at the test beam site T24.

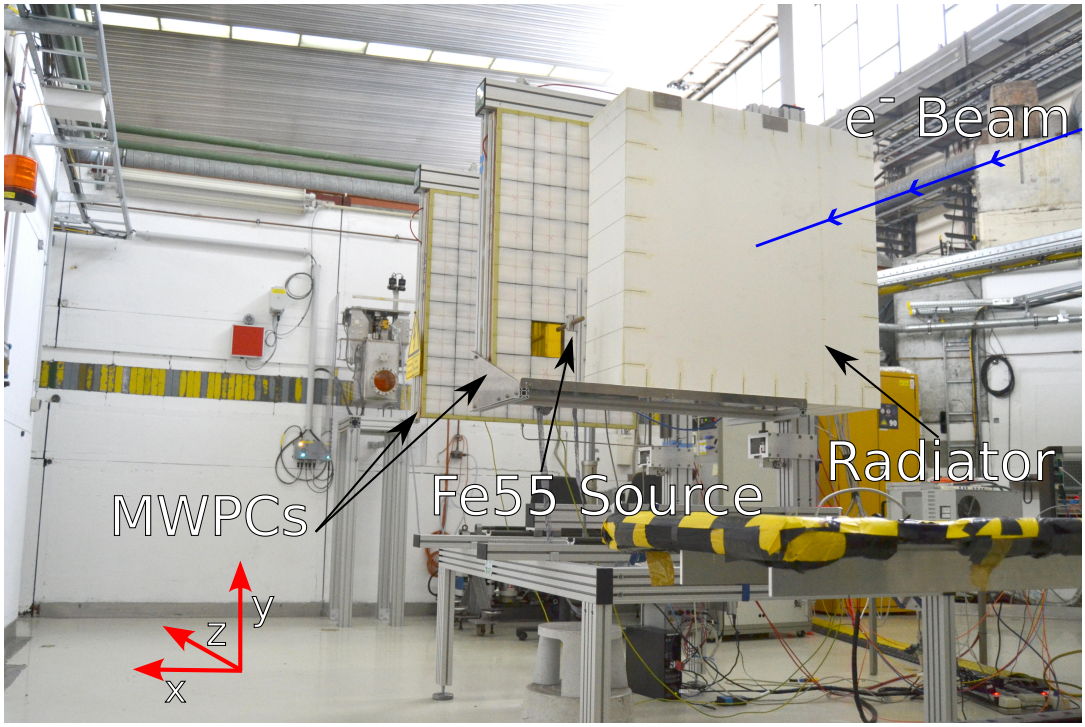

Figure 4.2.: Detector setup used for radiator characterization. The electron beam enters from the right and passes through the radiator as well as the readout chamber. The radiator box is displaced to the right with respect to the readout chamber to create space for the ^{55}Fe source used for energy calibration purposes (Photo: F. Roether).

The setup consists of two „type 8“ CBM-TRD readout chamber prototypes. However, in the measurement runs used for this analysis, only the one in front was equipped with readout electronics. The type 8 MWPCs are a prototype series very close to the type 7 chambers which will be used in CBM, having the same composition and wire geometry as shown in Figure 3.14 and Figure 3.13. The main difference is the slightly larger pad size of $15.25 \times 0.72\,\mathrm{cm}$ at outer dimensions of $96 \times 96\,\mathrm{cm}$, thus resulting in fewer pads in total (768 compared to 1152 on a type 7 chamber, see Table 3.2). The gas volume is filled with a mixture of Xe and CO_2 with a ratio close to the foreseen 85 : 15 by setting the respective flows to $f_{\mathrm{Xe}} = 3\,\mathrm{l/h}$ and $f_{\mathrm{CO_2}} = 0.5\,\mathrm{l/h}$, resulting in a

mixing ratio of 85.7 : 14.3. The chambers are operated at an anode voltage of $U_{\text{anode}} = -1800\,\text{V}$ and a drift voltage of $U_{\text{drift}} = 500\,\text{V}$.
Radiator boxes of various widths are placed in front of the readout chamber, each filled with different amounts of PE foam mats, in addition to the 1.5 cm inside of the gaps in the carbon grid at the entrance window. The number of PE foam mats for each box is chosen such that the volume is completely filled, but the foils are not squeezed together. The parameters of the radiator configurations are summarized in Table 4.1. As shown in Figure 4.2, the radiator box is displaced in x so that an ^{55}Fe source can be placed directly in front of the readout chamber, to be used for energy calibration. Here, the PE foam mats inside the carbon grid are removed to increase the number of photons from the source reaching the detector volume.

Table 4.1.: Radiator width w_r, number of stacked foam mats N_m and resulting average number transitions $\langle N_f \rangle$ inside the radiator for all different configurations used in the measurements at DESY. The average number of transitions are calculated by multiplying the number of stacked foam mats by the average number of transitions per mat $N_m \times \langle N_f \rangle / N_m = \langle N_f \rangle$, with the value of $\langle N_f \rangle / N_m = 2.2$ for the used PE foam mats taken from [50].

Configuration	w_r (cm)	N_m	$\langle N_f \rangle$
No Radiator	0	0	0
1.5 cm inside Carbon Grid	1.5	7	15
10 cm Box + 1.5 cm inside Carbon Grid	11.5	53	117
15 cm Box + 1.5 cm inside Carbon Grid	16.5	78	172
20 cm Box + 1.5 cm inside Carbon Grid	21.5	103	227
25 cm Box + 1.5 cm inside Carbon Grid	26.5	128	281
30 cm Box + 1.5 cm inside Carbon Grid	31.5	153	337

4.1.2.1. ^{55}Fe as a Radioactive Source

^{55}Fe is a radioactive isotope of Iron with a half life of 2.7 y, decaying into the stable ^{55}Mn via electron capture [51]. When an electron from an outer shell subsequently fills the resulting vacancy either an Auger electron or an X-ray is emitted. However, at energies at around 5 keV the mean free path of the Auger electrons is too short to reach the detector in the measurement setup. The most relevant X-rays are the $K_{\alpha 1}$ (5.90 keV), $K_{\alpha 2}$ (5.89 keV) and K_β (6.49 keV) with relative probabilities of 100 : 51 : 20.5 [52]. As they can not be separated with the energy resolution of the CBM-TRD, they are treated in the following as mono-energetic radiation with an energy of 5.97 keV, calculated by a weighted average.

4.1.3. Data Acquisition

The Data AcQuisition (DAQ) chain used for the measurement consists of several components, converting the analog pulses from the individual pads into digital signals with time and position information and storing them into archive files on a PC for later analysis. The main piece of this chain is the Self-triggered Pulse Amplification and Digitization ASIC (SPADIC) 2.2, a readout chip specifically designed for the CBM-TRD, which is directly connected to the pads.

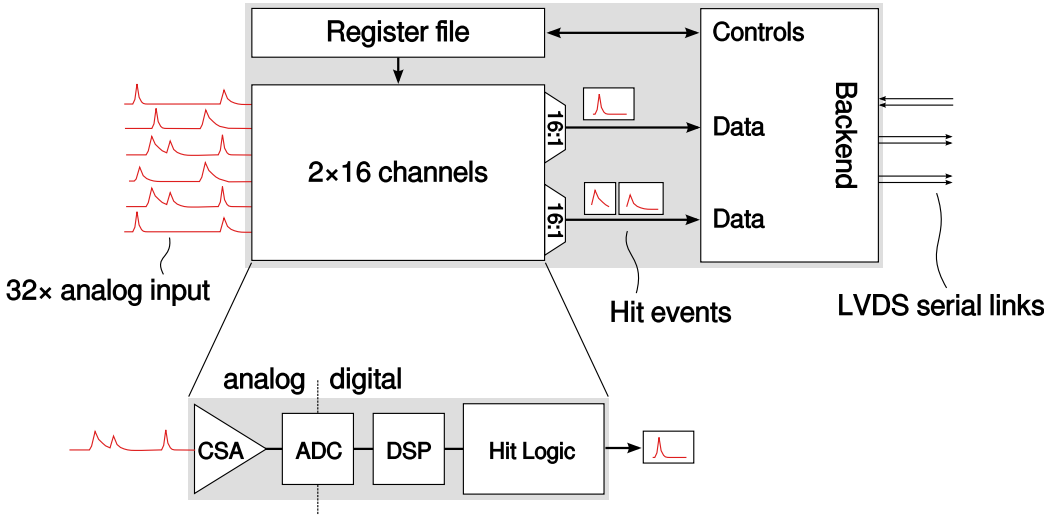

Figure 4.3.: Block diagram showing the layout of the SPADIC. The chip contains 32 independent channels, each connected to an individual pad. The channels themselves consist of a Charge Sensitive Amplifier (CSA), an Analog to Digital Converter (ADC), a Digital Signal Processor (DSP) and a Hit Logic, and are grouped into two half-chips of 16 channels each [35].

Figure 4.3 shows the layout of the SPADIC. It consists of two half-chips, each containing 16 individual channels which are connected to the pads of the MWPC. The channels themselves consist of several components: First, the incoming pulse is amplified and shaped by a CSA, generating a signal of the following shape [35]:

$$f(t) = A \cdot \frac{t}{\tau} \cdot \exp -\frac{t}{\tau} \text{ (for } t \geq 0) \tag{4.1}$$

In the SPADIC 2.2, the peaking time of the signal as a response to a delta-like input charge is $\tau = 110\,\text{ns}$ [53]. However, due to the finite signal collection time of the chamber ($t_{\text{col}} < 300\,\text{ns}$ [35]), the pulse produced in a real measurement will be longer. This pulse is then digitized by a 9 bit ADC with a

sampling rate of 16 MHz, resulting in one sample every 62.5 ns. Due to non-linearities the effective resolution of the ADC is roughly 8 bit [35]. Behind the ADC, the digitized signal can be scaled, inverted or shifted by a DSP before passing into the Hit Logic unit. At the DESY test beam campaign, none of the DSP functionalities were used. The SPADIC features a free-streaming, Self-TRiggered (STR) readout. Therefore, the Hit Logic continuously checks if the incoming signal fulfills a user-defined trigger condition, on the basis of which the samples are either discarded or further transferred to be recorded on disk. The trigger condition features two programmable threshold values T_1 and T_2 and can be expressed as [53, 54]:

$$t = [(a \leq T_1) \vee (b \leq T_2)] \wedge (b > T_1) \wedge (c > T_2) \tag{4.2}$$

The user can choose between two different trigger modes: In the „absolute“ mode a, b and c in Equation 4.2 refer to three subsequent ADC samples, in the „differential“ mode on the other hand, they refer to three subsequent **differences** between ADC samples, i.e. for a given set of four successive samples s_1 to s_4, they are calculated as $a = s_2 - s_1$, $b = s_3 - s_2$ and $c = s_4 - s_3$ [53]. With the differential trigger mode it is possible to trigger the readout solely on the basis of the rising flank of the signal regardless of its absolute ADC values, which depend on the baseline level on the individual channel. The differential trigger mode was chosen for the measurements at DESY, with the thresholds set to $T_1 = 10$ ADU and $T_2 = 16$ ADU for the electron beam and $T_1 = 12$ ADU and $T_2 = 20$ ADU for the ^{55}Fe source.
If a signal fulfills the condition in Equation 4.2, the readout is triggered and a hit message is generated, containing 32 ADC samples, as well as various meta data, such as time and channel information. Furthermore, the SPADIC features a so-called Forced Neighbor Readout (FNR) trigger logic: Once the readout on a pad is triggered, the adjacent pads are read out as well, even if the signals on these pads do not exceed the trigger thresholds. With this feature also smaller amounts of charge shared with the neighboring pads can be used for position determination, increasing spacial resolution [35]. The information if the hit message was generated by fulfilling the trigger condition is encoded in its meta data with the so-called „trigger type“ being either STR or FNR (or both).
Since both the electron beam and the ^{55}Fe source are well collimated, illuminating only small parts of the MWPC, the chamber is equipped with only two SPADICs.

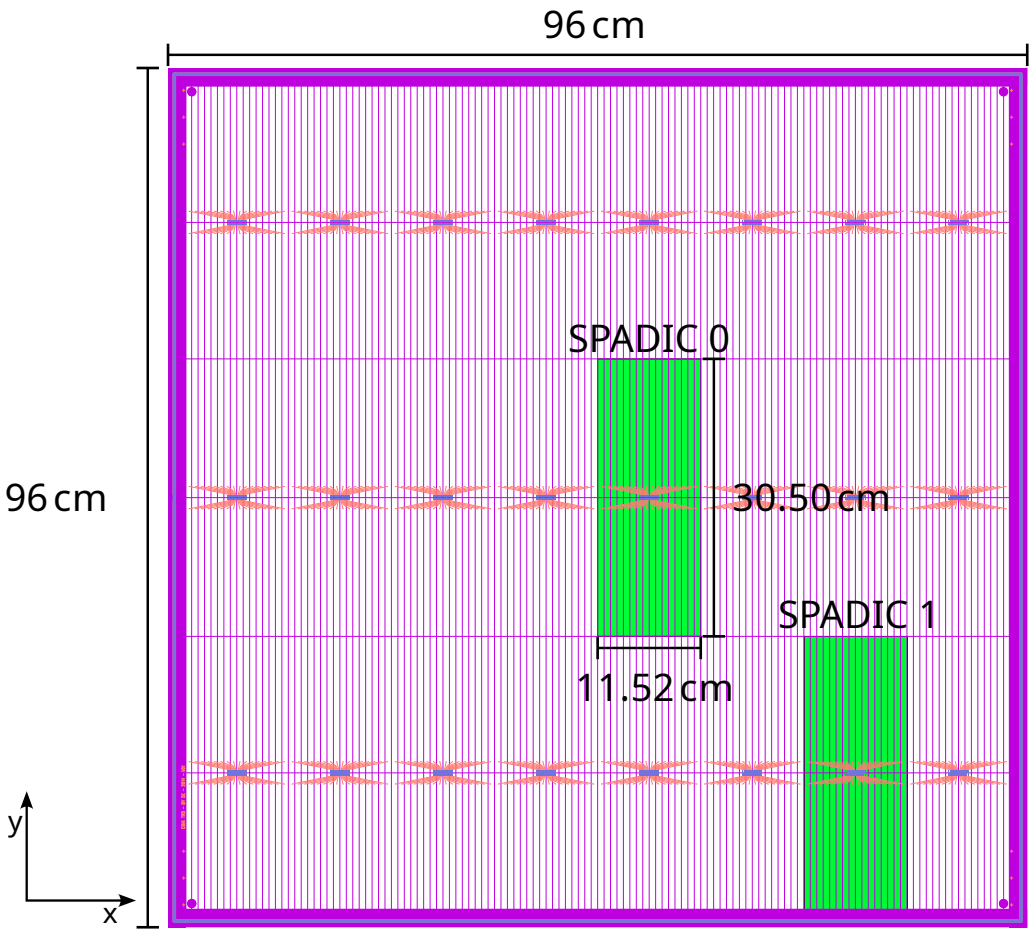

Figure 4.4.: Technical drawing of the pad plane of a type 8 MWPC with the areas read out at the measurements at DESY sketched in green, as seen looking towards the beam. Technical drawing supplied by D. Emschermann.

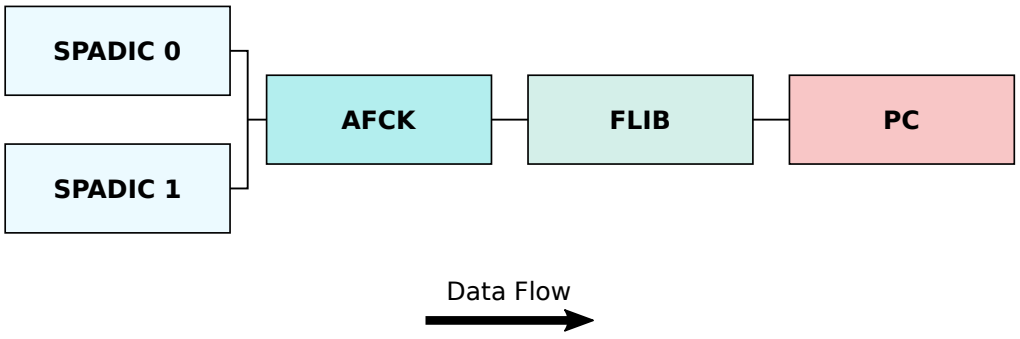

Figure 4.5.: Flowchart depicting the different components of the DAQ chain used for the measurements at DESY. SPADIC 0 is connected to the pads close to the electron beam, while the SPADIC 1 reads out the area hit by the photons from the ^{55}Fe.

Figure 4.4 shows the parts of the pad plane equipped with readout electronics marked in green. As can be seen, the chamber is oriented with the high pad granularity in x-direction. The beam passes through the detector at the upper row of pads connected to SPADIC 0, while the ^{55}Fe source was placed in front of the upper row of SPADIC 1. Both SPADICs are connected to a so-called AMC FMC Carrier Kintex (AFCK), a processing board combining the data stream of up to three readout chips. The AFCK is also used as an interface to load configurations onto the SPADICs and synchronize their clock cycles. From the AFCK, the data is sent to the FLES Interface Board (FLIB), which is the interface between the components processing the „running“ data stream (*online*) and the PC, where it is stored for later analysis (*offline*). The FLIB writes the data into Time Slice Archive (TSA) files, consisting of multiple time slices, data containers with a length of 0.0128 s each. The entire DAQ chain used is sketched in Figure 4.5.

4.2. Data Analysis

4.2.1. Reconstruction Process

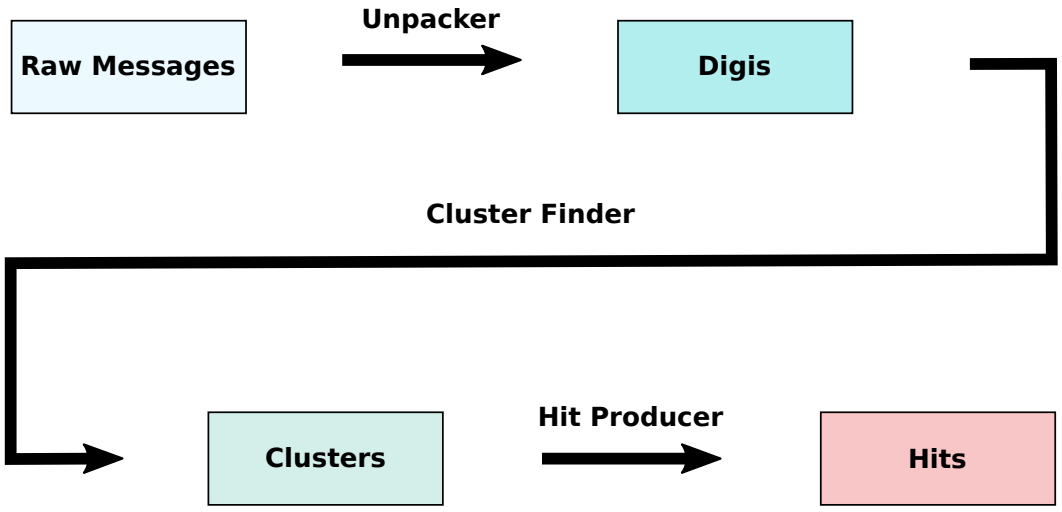

Figure 4.6.: Flowchart of the reconstruction steps in `cbmroot` converting the signal shapes measured on individual pads into hits which contain energy, time and position information.

To reconstruct the position resolved energy loss spectra, the charge signals registered on the individual pads of the segmented pad plane have to be processed and combined, which is done in various steps by different classes inside `cbmroot`, as shown in Figure 4.6. The data types used in the process are

listed and described below, including the name of the corresponding class name inside `cbmroot` in parentheses:

- **Raw Message** (`CbmTrdRawMessageSpadic`): Output of each individual readout channel of the SPADIC, containing the signal shape produced by the SPADIC as a response to the induced charge on the connected pad. It consists of (up to) 32 samples of the pulse height as digitized by the ADC as well as information about the time, channel and trigger type of the signal.
- **Digi** (`CbmTrdDigi`): Smallest unit of information inside the reconstruction chain. It contains the charge (in ADC Unit (ADU), time and trigger type and global address of the pad.
- **Cluster** (`CbmTrdCluster`): Combination of digis from adjacent pads in order to summarize all charge produced by a single particle. It stores the amount of digis it is comprised of, as well as their global addresses and the combined charge and time information.
- **Hit** (`CbmTrdHit`): Information unit corresponding to an energy deposit of a single particle in the detector. It contains the position in x-y-z-coordinates, time and charge/energy (in ADU or keV depending on calibration).

To produce digis from the raw messages, the unpacker reads the information of the channel and SPADIC on which the signal was received and combines them into a global address uniquely identifying the individual pad. Furthermore a method to calculate the charge from a signal shape has to be chosen. In this analysis, the charge is defined as the maximum value of the signal shape minus the first sample, which corresponds to the baseline. Then, the cluster finder searches for digis from adjacent pads with the same time stamp and combines them into a single cluster, summing up the individual charge values of the digis. While a cluster can in principle span over multiple rows of pads, both the electron beam and ^{55}Fe source are strongly collimated and set to hit the center of a pad row and thus all clusters extend over a single row. Therefore, the *width* of a cluster refers to the number of pads in x-direction, while the size in y is assumed to be one pad. Finally each cluster is converted into a hit by calculating its position using the center-of-gravity method and setting its total charge as the energy value. To avoid confusion, the uncalibrated energy value of the hit will be referred to as *charge* (with ADU as unit), while calling only the calibrated value *energy*.

4.2.2. Noise Reduction

Before reconstructing any energy loss spectra, several methods are implemented at different positions in the reconstruction chain shown in Figure 4.6

to reduce the amount of unwanted noise. In the following, exemplary plots are shown with data from run 55, the measurement run without a radiator.

4.2.2.1. Signal Shape Filter

First, the self-triggered signal shapes measured on channel 16 of SPADIC 0 were inspected, which is one of the main channels registering the electron beam. An overlay of signals is shown in Figure 4.7.

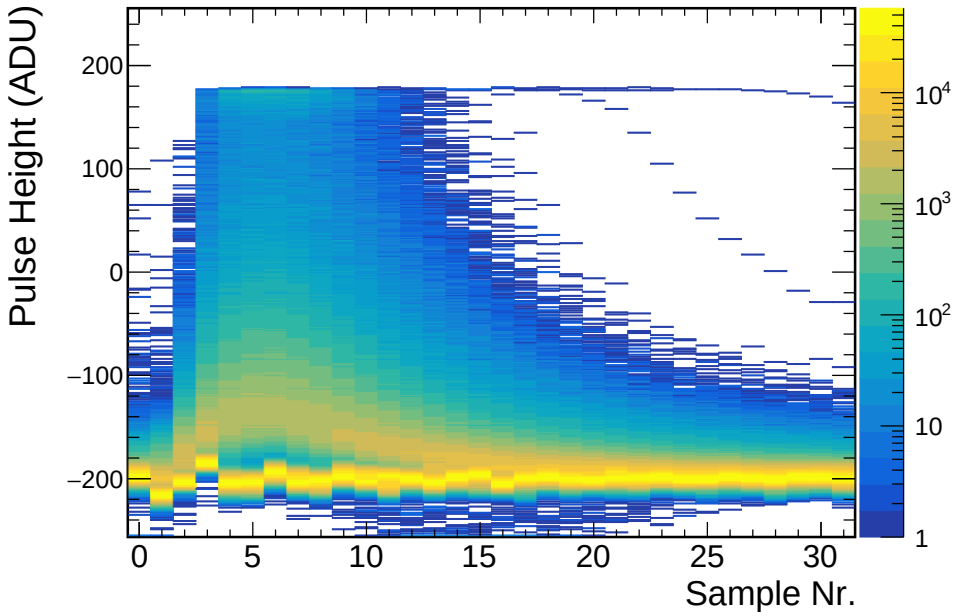

Figure 4.7.: Overlay of self-triggered signal shapes registered on channel 16 of SPADIC 0.

As can be seen, in addition to the regular „expected“ signal shapes, there are many very flat signals which only show some deviation from the baseline at the point where they triggered the readout (samples 1 to 3). To reject as many of these signals as possible, the following filter condition is implemented:

$$\text{Accept if: } \left(\frac{s_0 + s_1 + s_2}{3} + c_1 < s_4\right) \wedge (s_1 + c_2 < s_5) \tag{4.3}$$

with s_i denoting the measured sample i and the constants $c_1 = 15$ and $c_2 = 20$. The condition itself and the constants therein where optimized by trial and error, but kept rather loose to avoid biasing the signal.

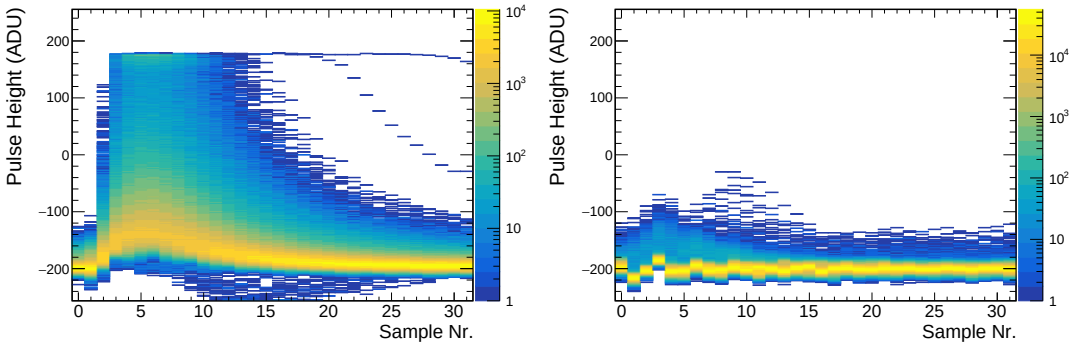

(a) Accepted (b) Rejected

Figure 4.8.: Overlay of self-triggered signal shapes registered on channel 16 of SPADIC 0, which are accepted by the filter condition in Equation 4.3 (left) and rejected by it (right).

4.2.2.2. Cluster Filter

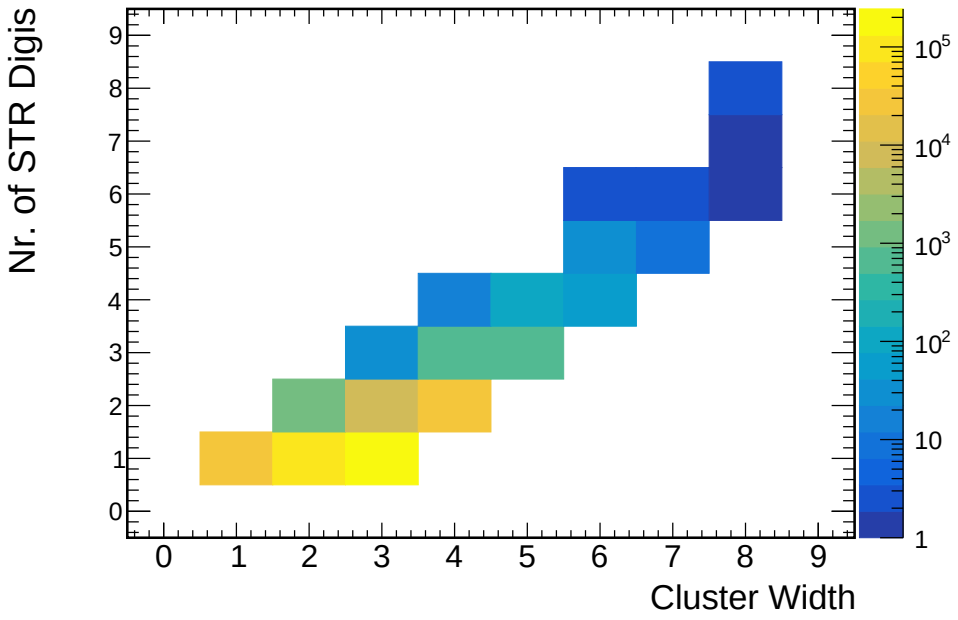

Figure 4.9.: Number of STR digis plotted against the width of the cluster on SPADIC 0.

Due to the FNR feature of the SPADICs hit logic, each cluster should contain exactly two FNR digis, one on each edge. However, if the pad triggering the readout lies at the edge of the active area or next to a deactivated or misconfigured channel, it may occur that the neighboring digi is missing. Since it

is not clear in these cases how much charge information is lost, these *irregular* clusters are excluded in this analysis. As can be seen in Figure 4.9, most clusters lie on the diagonal of N_{STR} = width − 2, and thus have exactly two FNR digis. In this case 19.4% of clusters on SPADIC 0 are irregular. However, these mostly stem from channels whose neighbors were deactivated to reduce noise, and one channel (channel 20) whose FNR configuration was wrongly set. In the region defined as the *beamspot* (see Section 4.2.2.3) only 3.17% of clusters are irregular.

4.2.2.3. Hit Filter

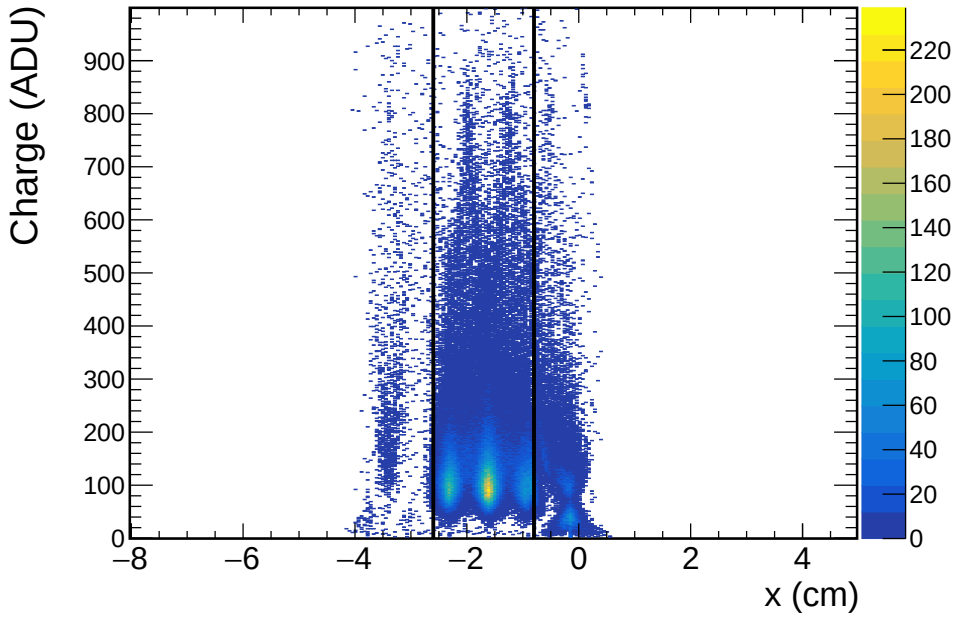

Figure 4.10.: Charge vs x position of all remaining hits on the upper row of SPADIC 0. The vertical black lines indicate the area referred to as beam spot in this analysis, with all hits laying outside being rejected.

Figure 4.10 shows the charge of all remaining hits on the upper row of SPADIC 0 plotted against their position in x. As can be seen, the area with the most entries is located at around $x \simeq -1.6\,\mathrm{cm}$ and is thus identified as the center of the beamspot. Its left edge is caused by a misconfiguration of the FNR feature of a channel (pad 315, channel 23), causing it to not be read out when a signal on its right neighbor (pad 314, channel 20) surpasses the trigger threshold and vice versa. Therefore no valid clusters can be reconstructed in the area $x < -2.6\,\mathrm{cm}$. On the right side artifacts caused by defective ADC on channel 12 connected to pad 310 can be seen. Starting at

$x \sim -0.8\,\mathrm{cm}$, when a significant amount of charge is registered on pad 310, the reconstructed value becomes distorted. For clusters centered on this pad ($-0.5\,\mathrm{cm} \lesssim x \lesssim 0.1\,\mathrm{cm}$), a large amount of entries at small charge values can be seen. Therefore, a cut on the x-position is implemented, only accepting hits with $-2.6\,\mathrm{cm} \lesssim x \lesssim -0.8\,\mathrm{cm}$. This region is in the following referred to as the *beam spot*.

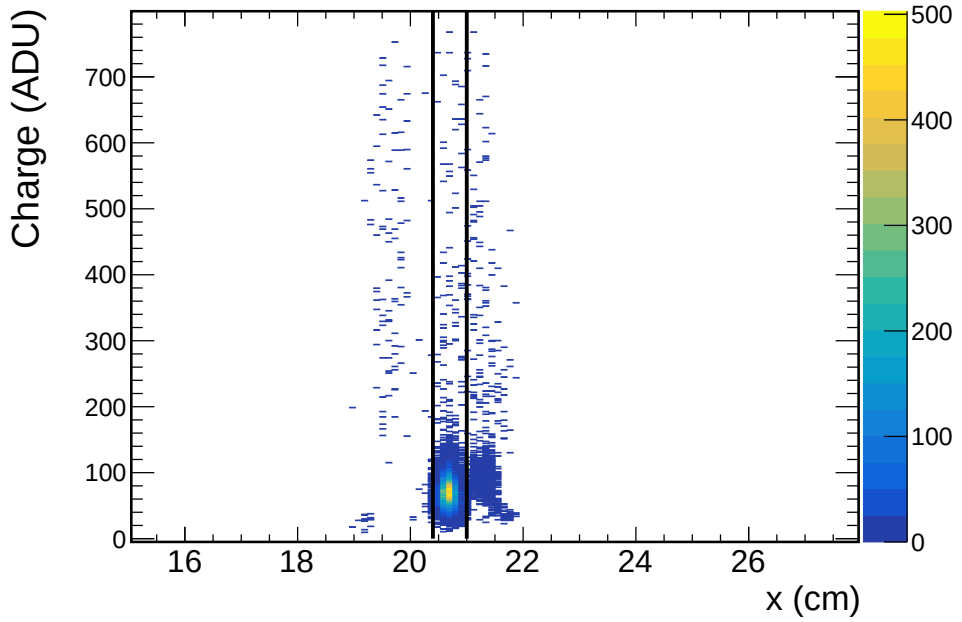

Figure 4.11.: Charge vs x position of all remaining hits on the upper row of SPADIC 1. The area between the vertical lines is defined as the *source spot* and all hits outside of it are rejected.

The x-positions of the hits on SPADIC 1 are shown in Figure 4.11. Evidently the source is strongly collimated and for the most part only hits one pad (pad 537, channel 18). Due to a defective ADC on the channel connected to its next-next-neighbor pad (pad 535, channel 14), many of the hits centered on pad 356 (channel 16) are distorted. To exclude these hits and the very few random triggers, hits with $x < 20.4\,\mathrm{cm}$ or $x > 21\,\mathrm{cm}$ are rejected. The remaining area is referred to in the following as the *source spot*.

4.2.3. Charge Spectra

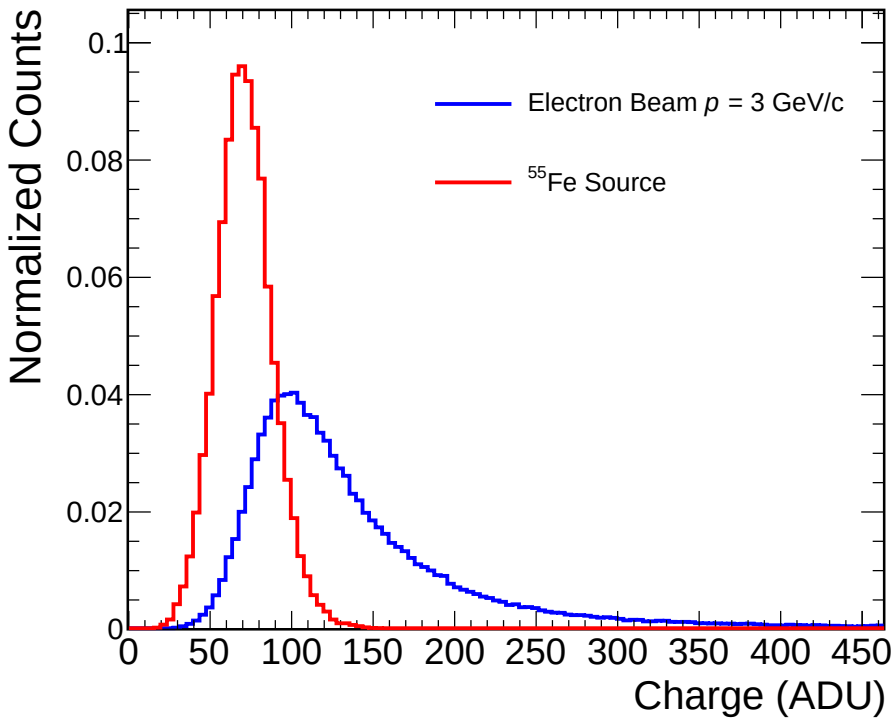

Figure 4.12.: Reconstructed uncalibrated energy loss spectra for the electron beam at $p = 3\,\mathrm{GeV/c}$ without a radiator and the photons from the ^{55}Fe source.

The resulting charge spectra for the electron beam at 3 GeV/c without a radiator in front of the MWPC and for the ^{55}Fe source can be seen in Figure 4.12. As expected, the mono-energetic photons from ^{55}Fe produce a Gaussian peak, while the electron spectrum exhibits its characteristic Landau-Gaussian shape [43]. However, their positions relative to each other do not match the theoretical expectations.

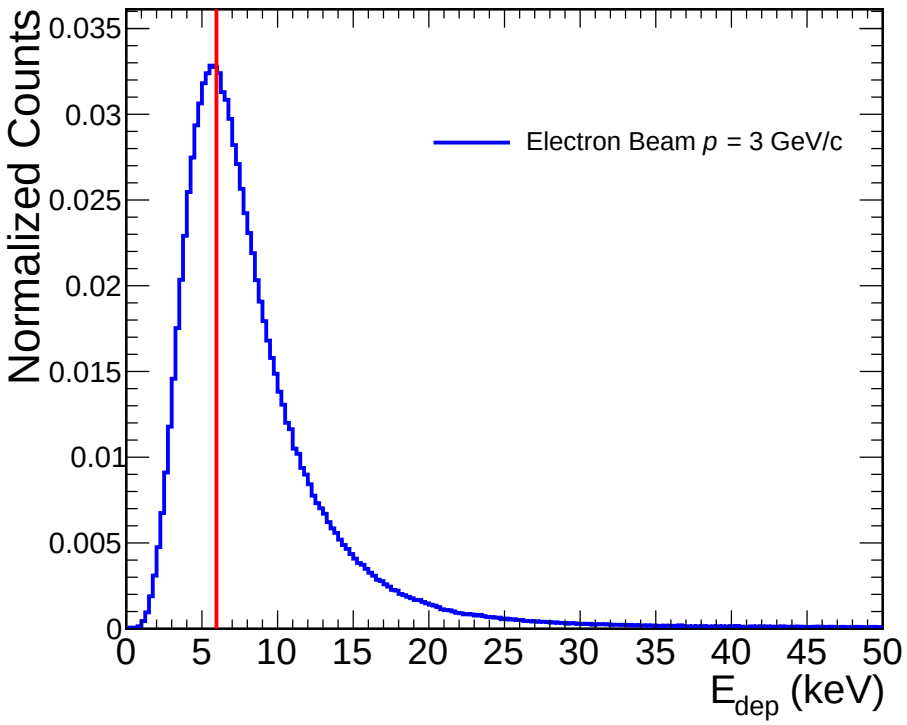

Figure 4.13.: Simulated energy deposit of electrons passing the CBM-TRD with $p = 3\,\mathrm{GeV/c}$. The red line indicates the energy $E_\gamma = 5.96\,\mathrm{keV}$ carried by the ^{55}Fe photons.

As can be seen in Figure 4.13, the Most Probable Value (MPV) of the electron spectrum should lie very close to the photon energy of $E_\gamma = 5.96\,\mathrm{keV}$, and therefore at the center of the Gaussian peak in the reconstructed spectrum, which is not the case in the data (Figure 4.12). This bias is a result of the differential thresholds used for the measurement, as will be demonstrated below.

4.2.4. Bias Investigation

4.2.4.1. ^{55}Fe Spectrum

In addition to the ones at nominal operating voltage of $U_{\mathrm{anode}} = 1800\,\mathrm{V}$[4] and $U_{\mathrm{drift}} = 500\,\mathrm{V}$, a set of measurements at various other values for U_{anode} ranging from 1680 V to 1950 V were conducted, which are useful to investigate the effect of the trigger thresholds on the recorded spectrum as the gain rises exponentially with the anode voltage [35]. First, the measured hit frequency

[4]For simplicity, the negative sign in front of the anode voltage is omitted in this section.

at the source spot is evaluated by simply counting the number of hits registered at the source spot in each measurement run and dividing this value by the measurement time.

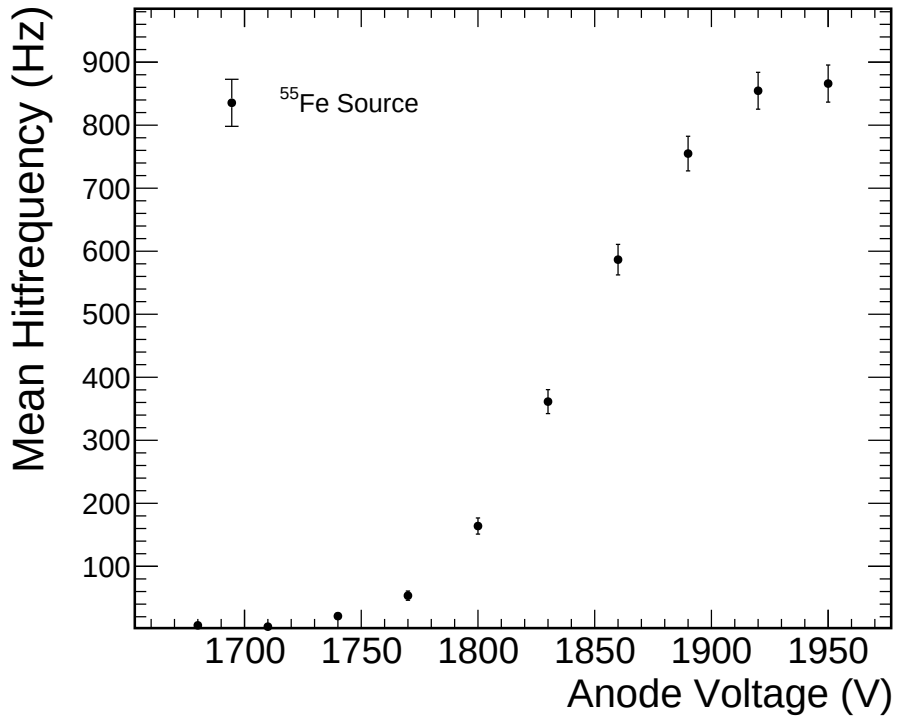

Figure 4.14.: Measured mean hit frequency at the source spot in dependence of the set anode voltage. The list of the used runs can be found in Table A.3

The resulting measured mean hit frequencies can be seen in Figure 4.14. As expected, the rate increases with anode voltage, as the gain rises and more and more signals are able to pass the trigger thresholds[5] until finally reaching a plateau, as the radioactive source emits a finite amount of photons and at a certain gain, all resulting signals will trigger a readout. Evidently this plateau is only reached at the highest anode voltage settings, while at the nominal value of $U_{\text{anode}} = 1800\,\text{V}$ only 18.6 % of the maximum rate is registered, and thus more than 80 % of the signals are not recorded. However, since differential trigger thresholds were set, there is no clear „cut-off“ point in the pulse amplitude, but rather just a strong suppression of low amplitude signals. This results in the reconstructed spectrum still resembling the

[5] While the energy deposit is always 5.96 keV, this still results in varying signal heights, depending on the position of the charge avalanche relative to the pad plane, timing of the pulse relative to the ADC sampling, noise, etc..

expected Gaussian shape, even though in reality it is strongly biased.

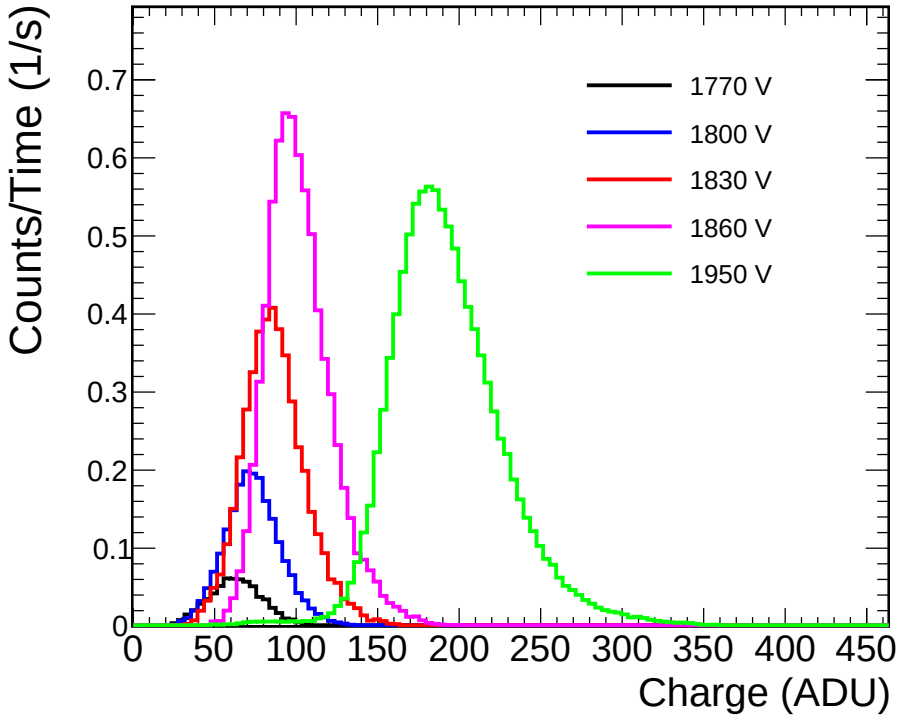

Figure 4.15.: Reconstructed charge spectra at the source spot for different anode voltages, normalized by measurement time. To improve readability, only selected anode voltages are shown. The full set of recorded spectra can be seen in Figure A.13.

Figure 4.15 shows the reconstructed ^{55}Fe spectra at different anode voltages, normalized by measurement time. As can be seen, with increasing voltage, the peak generally shifts to higher charge values. For the measurements up to $U_{\text{anode}} = 1860\,\text{V}$ also the peak height rises, further reflecting the increasing hit rate. In case all measurements had the same detection efficiency, the peak height would *decrease* with anode voltage, while the width would increase. For $U_{\text{anode}} \leq 1830\,\text{V}$ the left flank of the peak remains at the same position regardless of the set gain, further indicating that the spectrum is biased due to the trigger thresholds. Since it is known that the gas gain of the MWPC rises exponentially with the applied anode voltage [35], this should be reflected by the position of the peak, which can be approximated by a Gaussian fit.

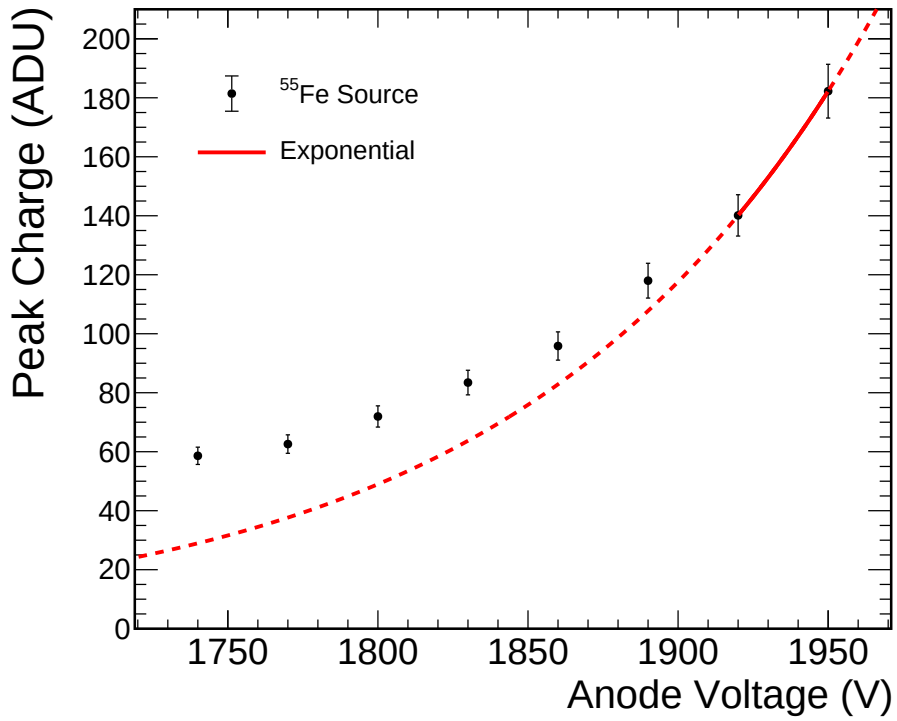

Figure 4.16.: Peak positions of the reconstructed charge spectra at the source spot as a function of the anode voltage. An exponential line is calculated using the last two data points.

Figure 4.16 shows the fitted peak positions as a function of the applied anode voltage. Based on the hit frequency, only the spectra at the two highest gain settings (U_{anode} = 1920 V and 1950 V) can be assumed to not be biased, and thus not enough data points are available for a meaningful exponential fit. The exponential curve, which can be calculated using the last two data points is drawn as a dashed red line to guide the eye. Since the curve is essentially overfitting the data, it is not necessarily reliable outside of the two used points. However, the position of the peak at the nominal anode voltage U_{anode} = 1800 V deviates also from an exponential fit which includes the last *three* data points (Figure A.14). This shift towards higher charge values is caused by the thresholds suppressing signals with lower amplitudes. Thus the ^{55}Fe spectrum measured at the nominal 1800 V is not suitable for an energy calibration. While in principle one could calculate a calibration factor from the exponential gain curve, this method is not feasible in this case, because not enough reliable data points are available for a fit. Furthermore, the electron spectrum is affected by the thresholds as well, which will be discussed in the following section.

4.2.4.2. Electron Spectrum

In the gain scan measurements used in the previous section electron spectra with a beam at $p = 2\,\mathrm{GeV/c}$ were also recorded at each anode voltage setting. However, due to time constraints in the measurement schedule, these were conducted with a 25 cm thick radiator present in the setup. Therefore, this data are not well suited for a bias analysis, as the shape of the spectrum and its dependence on the radiator width is one of the key parameters to be determined by this test beam campaign. On the other hand, a very detailed detector simulation of the CBM-TRD is fully integrated in `cbmroot`. It takes into account individual ionization points, their drift inside the gas volume, distribution of charge among the pads and individual signal generation [55, 56], which can be utilized to simulate the measurement conditions as realistically as possible.
Using the data from run 55 ($p = 3\,\mathrm{GeV/c}$, no radiator), where the expected electron spectrum is well known, efforts are made to reproduce the effect of trigger thresholds on the reconstructed spectrum. For this, the simulation needs to be tuned to resemble the data as close as possible, which is described in Section A.1.

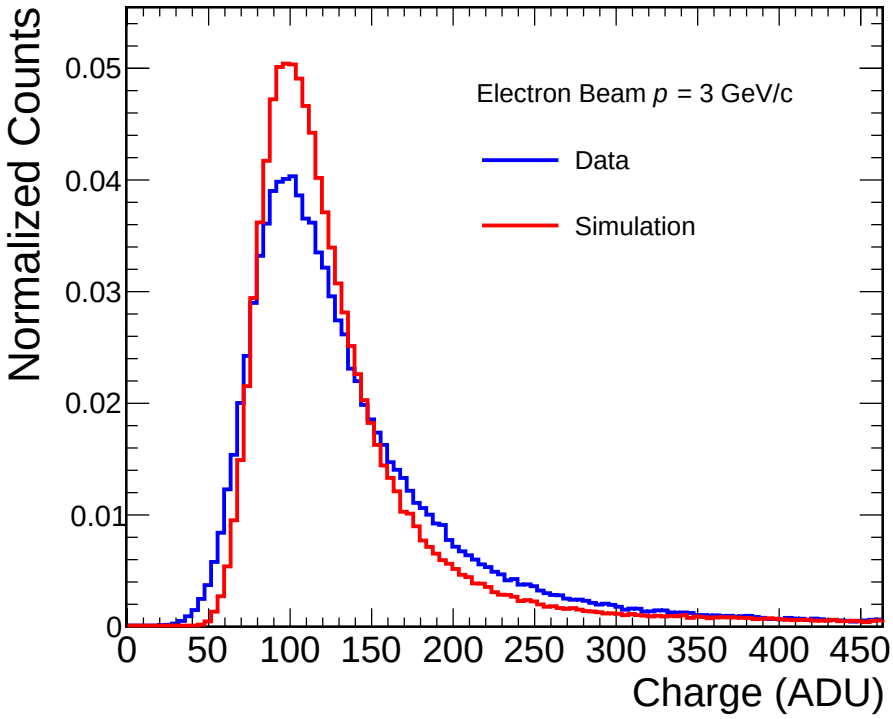

Figure 4.17.: Electron spectra reconstructed from measured and simulated data at $p = 3\,\mathrm{GeV/c}$ beam momentum without a radiator.

A comparison between the recorded and simulated spectra is shown in Figure 4.17. The same differential trigger thresholds of $T_1 = 10\,\mathrm{ADU}$, $T_2 = 16\,\mathrm{ADU}$ are applied. While the spectra match rather well, limitations of the simulation framework are evident, as many effects of the analog part of the SPADIC, e.g. correlated noise, oscillations on signal or baseline, differences between individual channels, are not included. Thus, the simulated spectrum appears less wide than the one reconstructed from the measured data. Therefore, the simulation is not suited for a quantitative study, but still useful to reproduce and understand the effect of the differential trigger thresholds on the electron spectrum.

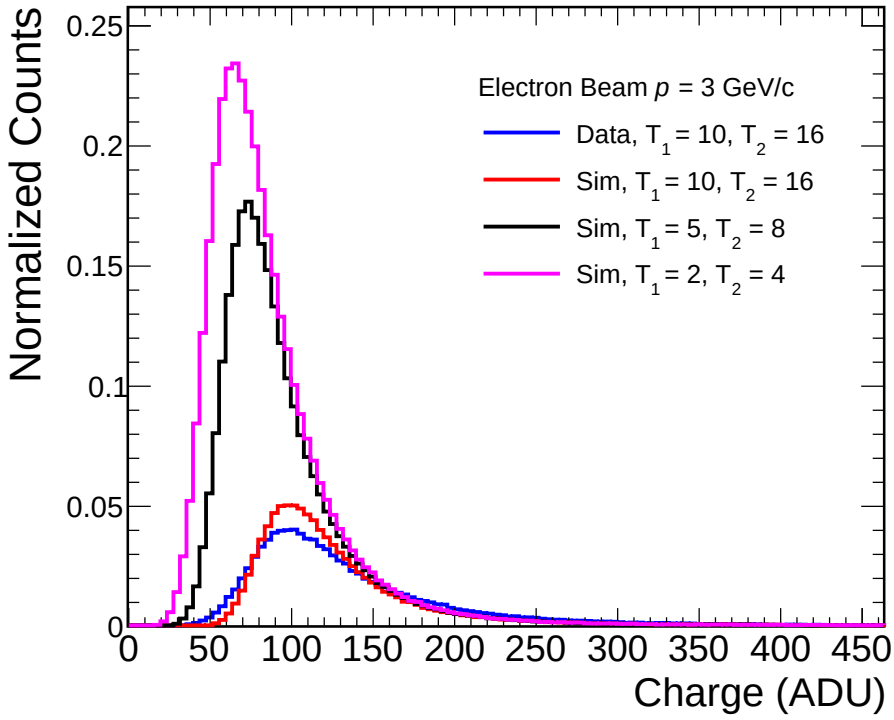

Figure 4.18.: Electron spectra reconstructed from measured and simulated data at $p = 3\,\mathrm{GeV/c}$ beam momentum without radiator for different settings of trigger thresholds.

Figure 4.18 shows the electron spectrum reconstructed from simulated data for different trigger thresholds. Evidently, for the thresholds used for the main measurement campaign ($T_1 = 10\,\mathrm{ADU}$, $T_2 = 16\,\mathrm{ADU}$), most signals are rejected, with the suppression being the strongest for low charge hits. In total 25.8 % of energy deposits in the readout area are reconstructed, which can be increased for example to 69.3 % ($T_1 = 5\,\mathrm{ADU}$, $T_2 = 8\,\mathrm{ADU}$) or 98.4 % ($T_1 = 2\,\mathrm{ADU}$, $T_2 = 4\,\mathrm{ADU}$). However, due to the prevalence of oscillations

on the analog signal and other sources of noise, these low threshold values would not be feasible in a real measurement. Furthermore, the numbers above should only serve as a rough estimate, since the behavior of the analog signal cannot be fully simulated and will also depend on external factors of the measurement setup (additional noise sources, grounding, etc.). These simulations demonstrate, in combination with the data analysis from the gain scan (Section 4.2.4.1), that the measured electron and ^{55}Fe spectra are strongly biased, even though at first glance they do not appear to be, when judged by their shape.

4.2.5. Radiator Comparison

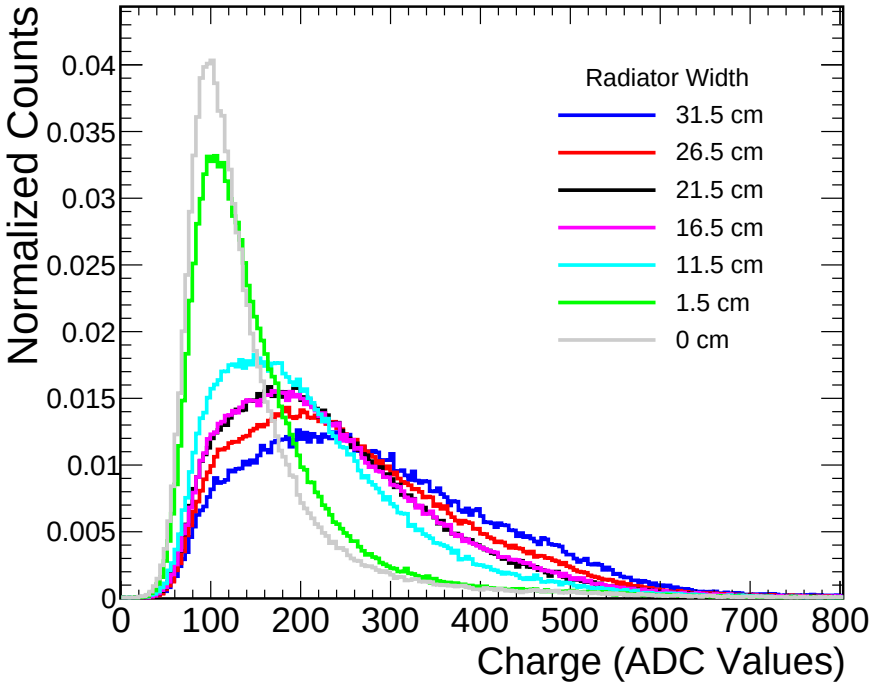

Figure 4.19.: Reconstructed electron spectra at a beam momentum of $p_{\text{beam}} = 3\,\text{GeV/c}$ for different radiators widths. A list of the used measurement runs can be found in Table A.4.

Due to the strong bias of both the electron and ^{55}Fe spectra by the differential trigger thresholds, a quantitative comparison between the electron spectra recorded with different radiators and the impact on electron pion separation performance of the CBM-TRD is not possible. Still, as the spectra are measured with the same conditions and settings, the biasing is assumed to impact all spectra to the same extent. Since the radiator width is the only parameter varied between the measurements, any difference seen in the spectra should

be a direct result of this change. Therefore it is still useful to compare the recorded spectra.
Figure 4.19 shows the spectra reconstructed from the measurement runs with different radiators. Peculiar is the fact that the data from run 49 (w_{rad} = 21.5 cm, black line) and run 59 (w_{rad} = 16.5 cm, magenta line) overlap perfectly. Most likely the same radiator was placed in front of the MWPC by accident for these runs. However, it is not possible to verify this, nor to confirm if both data were recorded with w_{rad} = 21.5 cm or w_{rad} = 16.5 cm. Still, the general trend of thicker radiators resulting in more entries at larger charge values and thus, higher energy deposits, clearly demonstrates their TR production capabilities. In particular, a clear difference is visible even between the radiators with the largest widths (w_{rad} = 26.5 cm and w_{rad} = 31.5 cm). Therefore, a conclusion from this measurements is, that the TR production does not fully saturate at widths $w_{\mathrm{rad}} \leq$ 31.5 cm, and thus a radiator of at least this width is preferred when optimizing exclusively for electron identification performance.
For a quantitative study these measurements should be repeated, utilizing the insights of this analysis to create better conditions. Since no sophisticated online data analysis tool was available at the 2019 test beam campaign, the trigger thresholds were set mainly by inspecting the total data rate and the pulse height spectra visible at the most active channels. In a future campaign, the gain scan should be performed and analyzed before recording the main data sets to check for any biasing of the spectra by the trigger thresholds, since this is not visible at a first glance (see Section 4.2.4). Measurements at lower thresholds might still be possible, as much of the noise can be filtered in the reconstruction by deactivating „bad“ channels, rejecting certain signal shapes and introducing cuts on the position of the hits, as shown Section 4.2.2.

5. Dielectrons

The main aim of measuring dielectrons in CBM is to observe the thermal radiation emitted by the QGP in the early stages, and by the hot and dense hadronic matter in the later stages of the fireball evolution, since this can provide valuable insights regarding the properties of the matter formed in the collision, as described in Section 2.3.2. However, thermal radiation is not the only source of dielectrons: Various mesons formed at the chemical freeze-out such as π^0, η or ω have decay modes resulting in electron positron pairs, either via two-body $X \rightarrow e^+e^-$ or three-body decays $X \rightarrow e^+e^- + Y$, involving a third decay product Y. In order to access the thermal radiation, this freeze-out cocktail has to be carefully reconstructed as well, so that it can be subtracted from the measured spectrum. Thus, the thermal radiation and the freeze-out cocktail are both considered to be „signal“ (as opposed to „background“) in the following sections, even though ultimately only the former is utilized to probe the desired fireball parameters (e.g. temperature, life time, etc.).
Since all signal originates from the primary collision vertex, the decays into e^+e^- pairs are not reconstructed individually, in contrast to, for example, multi-step decays with secondary or tertiary decay vertices. Instead, each electron track is simply paired with each positron track of a given event and their invariant mass compiled into a spectrum. Hence, any reconstructed dielectron spectrum will not only contain the „true“ pairs of electrons and positrons stemming from the same mother particle, but also all other possible combinations of e^+e^- from that event, forming the *combinatorial background*. This background is further increased by every track which originates from other sources than the cocktail or thermal radiation, each leading to multiple additional combinations. Therefore, an effective background rejection to ensure a pure sample of signal e^+ and e^- tracks is of utmost importance for a dielectron pair analysis.
This chapter is split into several sections: In Section 5.1 and Section 5.2 the software framework and signal input used for the analysis are described, respectively. Then, in Section 5.3, all methods utilized for the rejection of background from various sources are elaborated on, before finally discussing the resulting invariant mass spectra and signal-to-background ratios in Section 5.4. Since in most cases in this analysis particles and antiparticles are handled and processed in the same way, the latter are generally omitted in the following, referring to e^+ and e^- as „electrons“ , π^+ and π^- as „pions“ and

so on, except if explicitly stated.

5.1. Pair Analysis with the PAPA Framework

In essence, in a dielectron pair analysis all that needs to be done is to combine each electron track with each positron track of a given event and compile a spectrum of the invariant masses of all pairs. Of course, in reality the process is a lot more complex, involving various steps which need to be evaluated, selection cuts to be modified and their performance monitored, and for simulated data also the Monte Carlo (MC) information has to be processed. For this thesis, all of this is done using the Pair Analysis Package (PAPA). It was originally based on the dielectron framework used in ALICE [6] and then modified and implemented as PAPA into `cbmroot` by Julian Book. Further development was carried out first by Etienne Bechtel in Ref. [55] and then in this work. As input PAPA takes the particle tracks created with the standard reconstruction chain in `cbmroot` as well as the MC tracks which are output by the transport. Then, before filling any histograms, several steps are performed in which the user can apply selection cuts as shown in Figure 5.1.

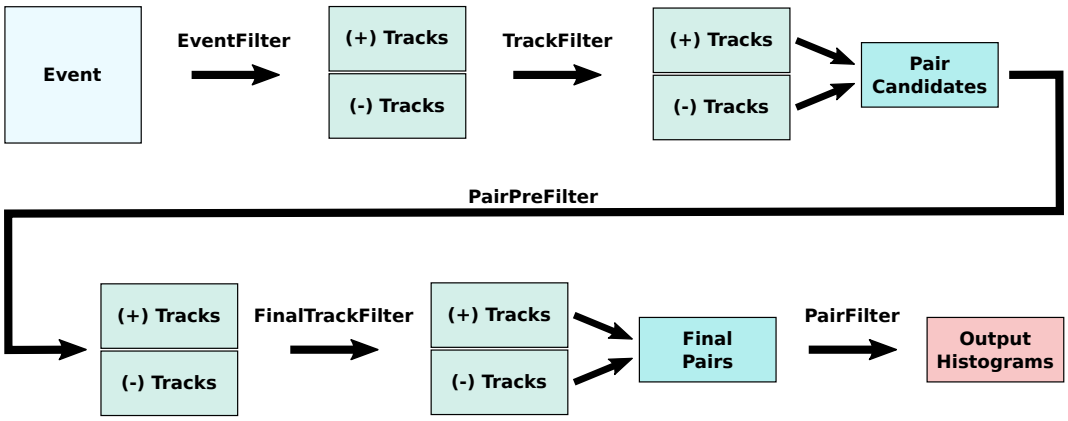

Figure 5.1.: Flowchart of the filtering steps performed in PAPA for each event. Adapted from Ref. [57] and [55].

At first, events can be selected or discarded based on their specific properties such as track multiplicity, centrality etc. with the so-called `EventFilter`. If an event is not discarded, all contained charged tracks are then filled into arrays and cuts depending on the individual track attributes (e.g. momentum, number of hits in a specific detector) can be applied, which is called `TrackFilter`. The remaining tracks are subsequently passed into the `PairPreFilter`, where positively and negatively charged tracks are paired and both

[6] https://github.com/alisw/AliPhysics/tree/master/PWGDQ/dielectron/core

legs can be rejected on basis of the attributes of this so-called *Pair Candidate*. After the `PairPreFilter`, the user can again apply cuts on individual tracks in the `FinalTrackFilter` before the final pairs are then built by combining each remaining positive track with each remaining negative track. Finally, these pairs can be filtered one more time with the `PairFilter`. The reason for having two track filtering stages which essentially work in exactly the same way (`TrackFilter` and `FinalTrackFilter`) is that the performance of the `PairPreFilter` strongly depends on its position in the cut sequence, as will be described in Section 5.3.2.1 and, in more detail, in Section A.3.

5.2. Signal Input

The heavy-ion collisions used for this analysis are generated using the Ultra-relativistic Quantum Molecular Dynamics (UrQMD) package, a microscopic transport model with hadrons as degrees of freedom, explicitly simulating their propagation through time and space and their individual hard and soft interactions [58–60]. The collisions are simulated at a beam momentum of 12 AGeV, corresponding to a center-of-mass energy of $\sqrt{s_{NN}} = 4.90\,\text{GeV}$, which is the top energy at which CBM will operate, and at an impact parameter of $b = 0\,\text{fm}$. Since these are the most central collisions physically possible, this results in the highest number of participants and therefore the highest amount of signal and background tracks. As will be demonstrated below (Section 5.3), the combinatorial background increases quadratically with the number of tracks, while the signal yield only increases linearily. Thus, these collisions can be seen as the most demanding in terms of background reduction.
However, UrQMD does not produce the rare probes relevant for this thesis (i.e. most of the dielectron *freeze-out cocktail* and thermal radiation), these decays are simulated with the *Pluto* event generator and subsequently embedded into the UrQMD collisions. Pluto is a lightweight and highly flexible simulation package for hadronic interactions, originally developed for the HADES experiment [61, 62]. The relevant dielectron decays of resonances which are simulated with Pluto are summarized in Table 5.1. One decay of each of these channels is embedded into every UrQMD collision. In the analysis, tracks from these decays are then scaled according to the expected yield per event of the particle and the branching ratio of the corresponding decay channel, as listed in Table 5.1. Additionally, the two types of thermal radiation described in Section 2.3.2, namely the one produced directly in the QGP and the in-medium modified spectral function of ρ and ω are simulated with Pluto. The used weighting factors (branching ratio × yield per event) are 4.2×10^{-2} and 6.2×10^{-4}, respectively. To further enhance the statistics for larger invariant masses, these decays are embedded assuming

Table 5.1.: Relevant dielectron decays simulated with Pluto and embedded into the UrQMD collisions. The yields per event were calculated using the SHM [3, 25, 63]. Branching ratio values taken from Ref. [24].

Decay channel	Yield per event	Branching ratio
$\eta' \rightarrow \gamma e^+e^-$	0.803	4.91×10^{-4}
$\Delta \rightarrow pe^+e^-$	229.5	4.2×10^{-5}
$\omega \rightarrow \pi^0 e^+e^-$	5.821	7.7×10^{-4}
$\omega \rightarrow e^+e^-$	5.821	7.38×10^{-5}
$\phi \rightarrow e^+e^-$	1.018	2.98×10^{-4}

a uniform mass distribution and then later rescaled according to the actual expected distribution in the analysis, as described in Ref. [55].

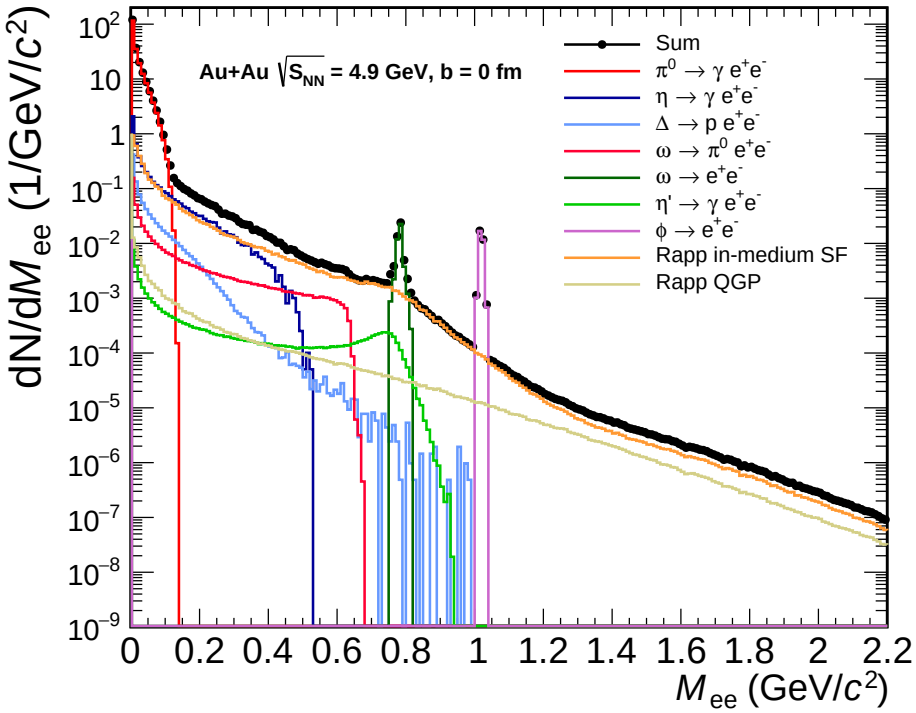

Figure 5.2.: Simulated invariant mass spectrum of all relevant dielectron decays scaled to the expected yield per event. The decays of π^0 and η are generated by UrQMD, all other decays using Pluto. The spectrum is generated using all MC tracks in the full phase space.

An invariant mass spectrum of the relevant dielectron decays is shown in Figure 5.2. It is compiled by using all MC tracks from these signals in the

full phase space. Its agreement with the expected spectrum shown in Figure 2.6 confirms that the embedding and weighting of the decays simulated with Pluto is working as intended. The propagation of these MC tracks and their interactions with the CBM detector are simulated using GEometry ANd Tracking (GEANT) 3 [64].

5.2.1. Acceptance Effects

Since the CBM detector does not cover the full phase space, acceptance effects have to be considered. In the context of this analysis, two classes of acceptance are used: *Tracking acceptance* refers to tracks which reach enough stations of the tracking detectors for successful tracking, while for *PID acceptance* the track also has to pass through the Particle Identification (PID) detectors.

Table 5.2.: Requirements for tracks to fall under the used acceptance definitions.

Acceptance Definition	Selection Cut
Tracking Acc.	MvdPoints + StsPoints ≥ 4
Tracking & PID Acc.	MvdPoints + StsPoints ≥ 4 TrdPoints ≥ 0

In detail, the former is implemented by requiring the combined number of MC points in MVD and STS to be four or larger, and for the latter, one MC point in the TRD is required, as summarized in Table 5.2.

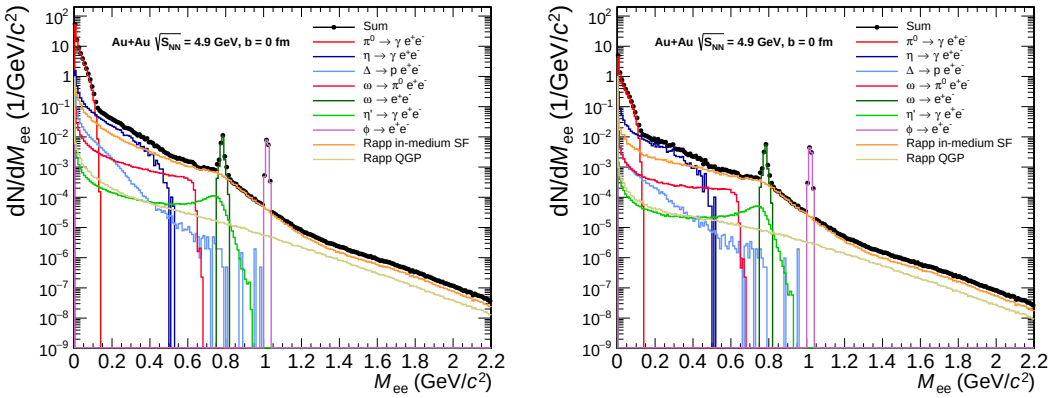

(a) Tracking acceptance

(b) Tracking and PID acceptance

Figure 5.3.: Invariant mass spectra in acceptance of the tracking detectors (left) and in acceptance of tracking and PID detectors (right).

Figure 5.3 shows the resulting invariant mass spectra using all MC tracks which fulfill the conditions noted in Table 5.2. As can be seen, while the general shape stays roughly the same, the total yields per event decrease. When including PID acceptance, this decrease is strongest at very low invariant masses.

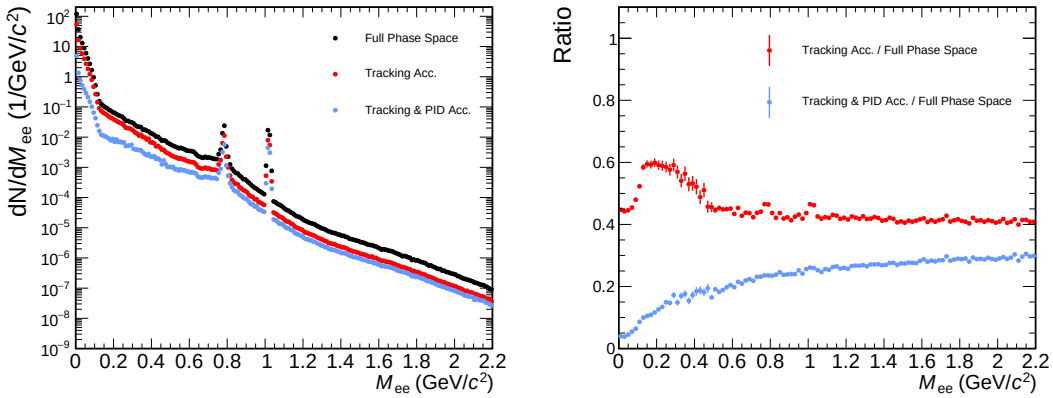

(a) Sum of all signals for different acceptances

(b) Sum of all signals for different acceptances divided by full phase space

Figure 5.4.: Sum of all relevant dielectron signals for different acceptances (left) and ratios of acceptance and full phase space (right).

The mass dependence becomes more evident when directly comparing the sum over all signals shown in the spectra. As can be seen in Figure 5.4b, the tracking acceptance is approximately 40% over the entire mass range, with an increase for pairs with $0.1\,\mathrm{GeV/c^2} \leq M_{ee} \leq 0.4\,\mathrm{GeV/c^2}$. In this mass region, the decay $\eta \rightarrow \gamma e^+e^-$, which is already included in the UrQMD collision, is one of the dominant contributions. While the tracks from decays simulated in Pluto are centered around mid rapidity ($y = 1.66$), the tracks from η in UrQMD appear to be shifted towards higher rapidities, thus increasing their probability to reach the tracking detectors. A comparison between tracks from $\eta \rightarrow \gamma e^+e^-$ (UrQMD) and $\eta' \rightarrow \gamma e^+e^-$ (Pluto) can be found in Figure A.16. This observation is still under investigation. Due to the low acceptance of the PID detectors in this mass range, its effect is expected to be minimal.

5.3. Background Rejection

Since the decays of interest for dielectron spectroscopy are very rare in comparison to other tracks in the detector, it is of utmost importance to select only relevant signals while rejecting as much background as possible. The

two main classes of this background are hadrons, which are falsely identified as electrons on the one hand, and electrons coming from other sources on the other hand. The former are mainly comprised of pions, protons and kaons, while the latter are predominantly electrons formed in photon conversion processes in the target or detector material $\gamma \xrightarrow[\text{material}]{} e^+e^-$.

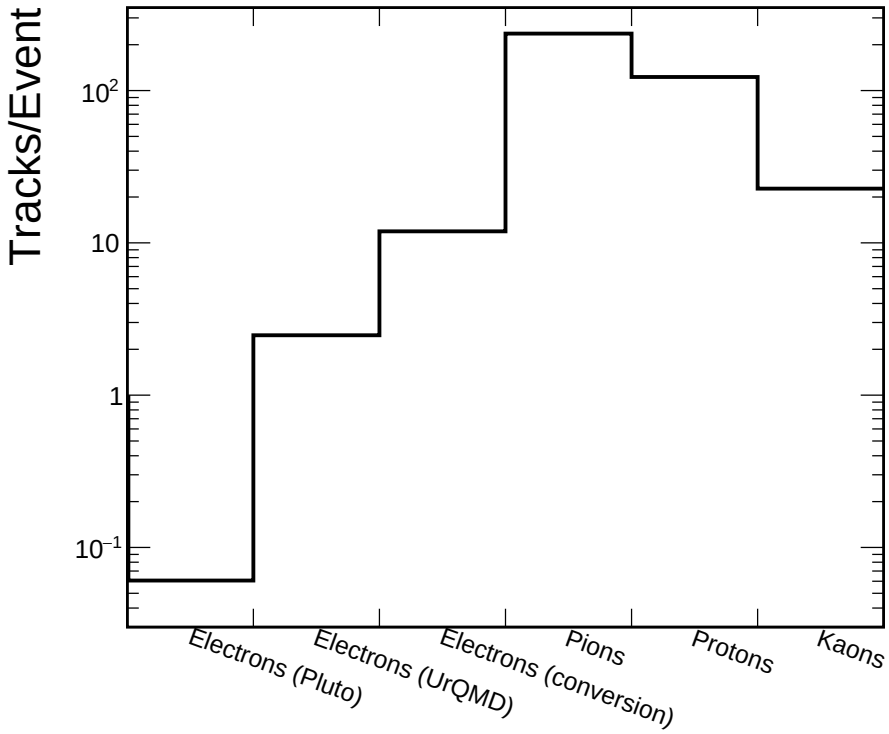

Figure 5.5.: Amount of tracks per event of different particle species and sources for all reconstructed tracks, each bin including the particle and its antiparticle. The decays embedded with Pluto are summarized in Table 5.1. Electrons from UrQMD refers to the relevant dielectron channels, i.e. π^0 and η Dalitz decays.

As can be seen in Figure 5.5, without any selection cuts the amount of tracks of interest for the spectroscopy is several orders of magnitude lower than the amount of other tracks. In addition to the sheer abundance of this background, combinatorics render a dielectron pair analysis very sensitive to any non-signal tracks in the final sample, as shown in Ref. [55]: With the number of positively charged signal tracks N_{S+} and negatively charged signal tracks N_{S-} the total amount of unlike-sign pairs from the same event is given by:

$$SE^{+-}(N_{S+}, N_{S-}) = N_{S+} \cdot N_{S-} \tag{5.1}$$

Adding N_{B+} positively charged and N_{B-} negatively charged background tracks to the sample will increase the number of combinations to:

$$SE^{+-}(N_{S+} + N_{B+}, N_{S-} + N_{B-}) = (N_{S+} + N_{B+}) \cdot (N_{S-} + N_{B-}) \tag{5.2}$$
$$= N_{S+}N_{S-} + N_{B+}N_{S-} + N_{B-}N_{S+} + N_{B+}N_{B-} \tag{5.3}$$

Finally, assuming an even split of the total amount of tracks for both charges ($N_{S+} \approx N_{S-} \approx 0.5N_{S,tot}$ and $N_{B+} \approx N_{B-} \approx 0.5N_{B,tot}$) Equation 5.2 can be simplified to:

$$SE^{+-}(N_{S,tot}, N_{B,tot}) \approx 0.25N_{S,tot}^2 + 0.5N_{B,tot}N_{S,tot} + 0.25N_{B,tot}^2 \tag{5.4}$$

As Equation 5.4 shows, the amount of pairs increases quadratically with the number of additional background tracks, demonstrating the need for effective rejection methods.
Naturally, the different background components require different rejection strategies, which are explained in the following sections, namely the rejection of the hadronic background in Section 5.3.1 and subsequently the rejection of the electron background in Section 5.3.2. This order was chosen, because it makes more sense *narratively*, i.e. first rejecting all tracks which are not electrons, and then rejecting all electron tracks which are not signal electrons. However, it should be noted that in practice this is not the order in which the cuts are applied, since the effectiveness of certain cuts may depend on their respective position in the cut sequence. The final order of cuts can be found in Table A.5.

5.3.1. Hadronic Background

All subsystems of the CBM electron setup (see Section 3.1) provide information which may be utilized for the reduction of the hadronic background. This leads to a large set of input parameters (e.g. momentum, shape of the Cherenkov ring in RICH, energy deposit in TRD, time-of-flight, etc.) for the user to tune selection criteria in order to achieve the most effective background rejection.

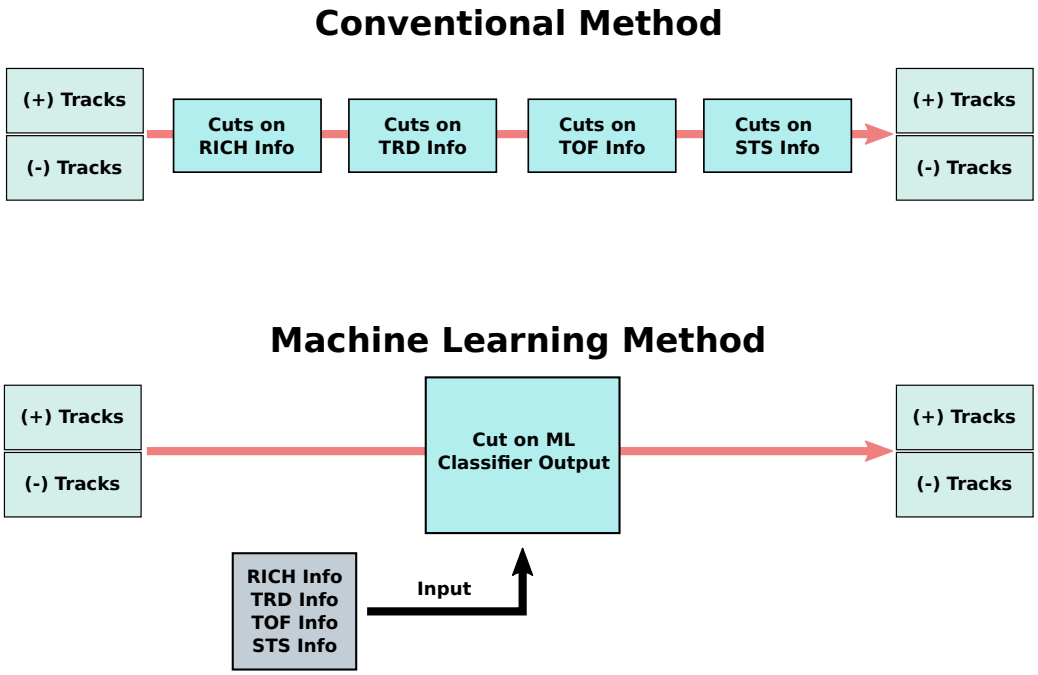

Figure 5.6.: Sketch of different approaches for cut based hadron rejection. The information provided by the different detectors is either used in subsequent one- or two-dimensional cuts, or it is used as an input for a Machine Learning (ML) classifier and a single (momentum dependent) cut on the output of this classifier is implemented.

One method of making use of all of the information is to define a set of subsequent cuts, each using a certain subset of the provided input parameters, and to then apply and evaluate them individually, as shown in the upper part of Figure 5.6. An advantage of this approach is high transparency and flexibility. If the information is used separately, the user can spot which parameters are the most useful, or which parts of the cut configuration might still be optimized or altered for a specific analysis. On the other hand, this approach does not effectively make use of all possible correlations between the parameters, since any selection cut depending on more than three variables becomes difficult to visualize and tune. This issue may be avoided by using a Machine Learning (ML) approach: Instead of implementing several cuts on small parameter subsets, a classifier is trained with ML methods, which uses all information simultaneously to create a single output proportional to the probability of the track being an electron. On the one hand, a cut on this parameter can then be easily optimized and tested. On the other hand, such a classifier is less transparent and flexible than the conventional approach as it operates largely as a black box and its performance relies on the training data and optimization parameters.

In the following sections, first the reduction of hadronic background using conventional cuts will be described, followed by a depiction of the ML approach and a comparison of the two.

5.3.1.1. Conventional Cuts

While all subsystems of the CBM setup may contribute to the electron identification, the main detectors dedicated to this task are the RICH and the TRD. Therefore, the usage of these two detectors will be covered first. The cuts applied before any of the information of the PID detectors is used are denoted as `PreCuts` and listed in Table A.5. On the one hand they ensure a basic track quality, while on the other hand, some are implemented for the rejection of electron background and will be described in Section 5.3.2.

PID with the RICH Detector

As stated in Section 3.1, the RICH detector identifies electrons based on their produced Cherenkov radiation. The Cherenkov threshold for pions in CO_2 is $p = 4.65\,\mathrm{GeV/c}$ [38]. Thus, in an ideal case, rejecting all tracks which did not produce a Cherenkov ring should remove all pions (and heavier particles) with a momentum below this threshold. In reality, due to mismatches in the reconstruction it may occur that a hadron track with a momentum below its respective threshold has a Cherenkov ring assigned. In these cases however, the shape of the ring and its distance to the track should differ from the shape and distance of true electron tracks. For pions with momenta above the Cherenkov threshold, the produced rings will also have different parameters than the ones from electrons at the same momentum. Hence, the electron identification using the RICH detector is done in two steps: Firstly, all tracks without rings are discarded by requiring the amount of `RichHits` to be greater than five. Subsequently, parameters describing the shape and size of the ring are used as input for an Artifical Neural Network (ANN), which outputs a value out_{ANN} between -1 and 1 corresponding to the likelihood of the track being an electron ($out_{\mathrm{ANN}} = 1.0$) or not ($out_{\mathrm{ANN}} = -1.0$). A sketch of the Cherenkov ring parameters is shown in Figure 5.7 and a full list of the inputs for the ANN can be found in Table 5.3.

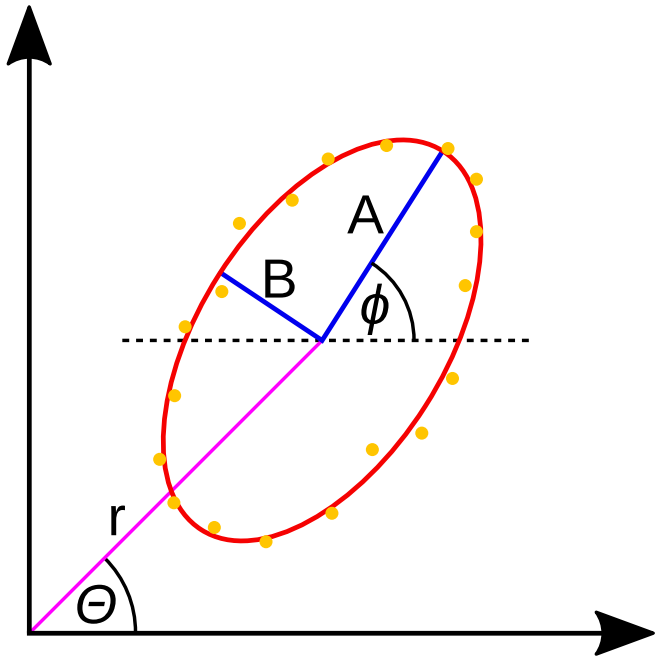

Figure 5.7.: Sketch of a Cherenkov ellipse produced by an electron in the RICH detector and the parameters characterizing its shape and position on the detector plane. The orange dots represent the reconstructed `RichHits` which are then fitted with the red ellipse. Adapted from Ref. [65].

Table 5.3.: Input parameters of the ANN used for further electron identification based on the RICH detector information.

Parameter	Description
NofHits	Nr. of `RichHits` attached to ring
χ^2/NDF	Squared distance of hits to ellipse
A Axis	Length of major semi-axis
B Axis	Length of minor semi-axis
ϕ	Tilt angle
Θ	Radial angle
r	Radial position
d	Distance of ring to track
p	Particle momentum

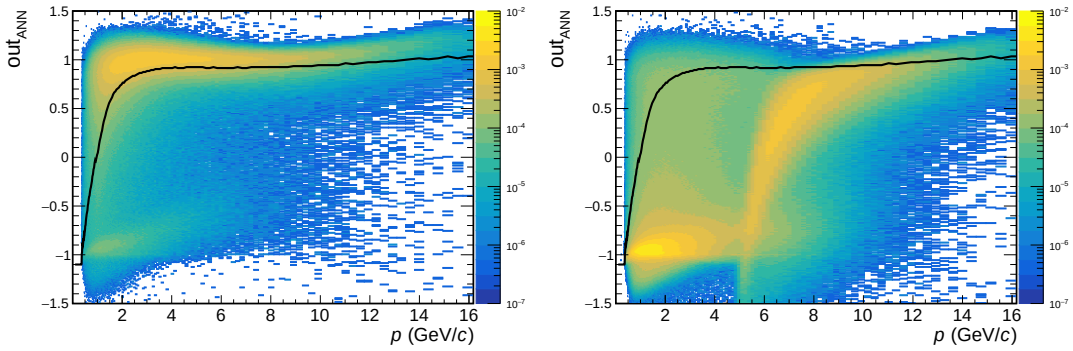

(a) Electrons (b) Pions

Figure 5.8.: Output of the ANN of the for electron identification based on the RICH ring parameters for electrons (left) and pions (right) as a function of the particle momentum. The black line indicates a cut with 80% electron efficiency in each momentum bin.

Figure 5.8 shows the output of the ANN for electrons and pions as a function of the momentum. While for low momenta ($\lesssim 1.5\,\mathrm{GeV/c}$) the particles are not well separated and many electrons receive relatively low output values, the ANN consistently assigns high values to electron tracks above about 1.5 GeV/c. Therefore, it makes sense to apply a momentum dependent cut, setting different thresholds for out_{ANN} in different momentum bins. The black curve in Figure 5.8 shows a cut with an electron efficiency of 80% in each momentum bin, where all tracks laying below the curve are being rejected. For pions, the output of the ANN exhibits more structures than for electrons (see Figure 5.8b), since two types of pion tracks are classified at once: On the one hand, there are pion tracks with a wrongly matched Cherenkov ring attached to them and on the other hand pion tracks which actually produced a ring themselves. The momentum distribution of the former resembles the momentum distribution of pions in general, with most tracks lying in the range between about 0.5 and 1.5 GeV/c and then strongly decreasing towards higher momenta. These pions can be seen on the left side of Figure 5.8b, and while many have low values for out_{ANN} they also smear out towards higher output values and make up the majority of pions which survive the ANN cut. The main parameter to recognize these fake ring matches is the distance between the track and the ring center. Unfortunately, this distance also increases for electrons at lower momenta due to multiple scattering, which is the reason for the worse separation at $p \lesssim 1.5\,\mathrm{GeV/c}$. The pions which produce rings themselves can be seen as a right-sided arch spanning from $p \sim 5\,\mathrm{GeV/c}$ and $out_{\mathrm{ANN}} < -1$ towards $out_{\mathrm{ANN}} \sim 1$ for $p \gtrsim 10\,\mathrm{GeV/c}$, showing that the higher the momentum, the more difficult it is for the ANN to distinguish between electron and pion rings as their parameters become

increasingly similar.

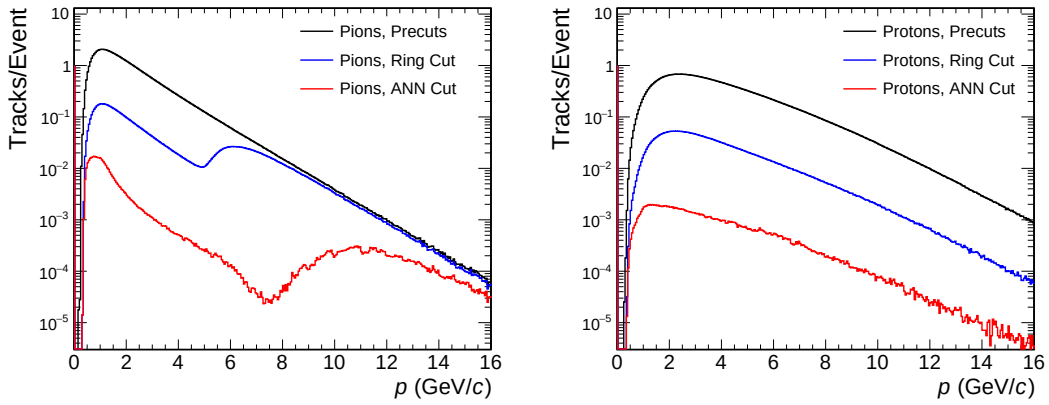

(a) Pions (b) Protons

Figure 5.9.: Momentum distribution of pion (left) and proton (right) tracks before and after the RICH cuts. The ring cut requires `RichHits` > 5, the ANN cut is set to 80% electron efficiency in each momentum bin.

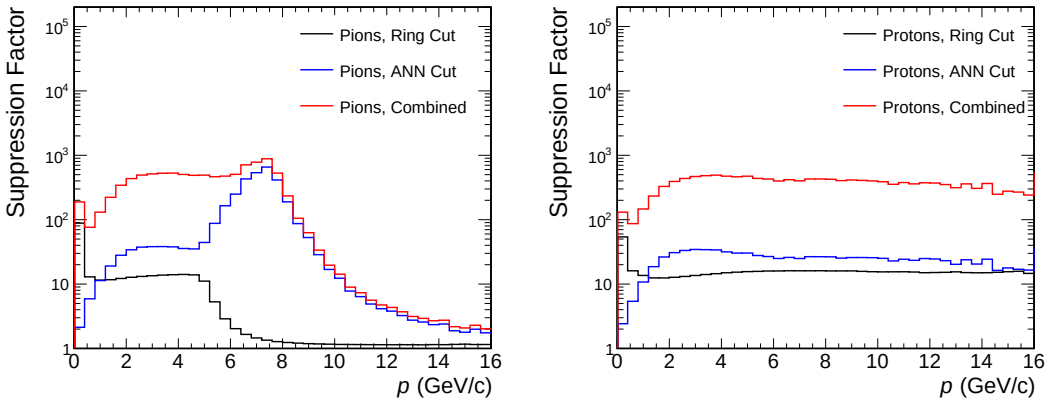

(a) Pions (b) Protons

Figure 5.10.: Suppression factors of the RICH cuts for pions (left) and protons (right) as a function of the momentum. The ring cut requires `RichHits` > 5 while the ANN cut is set to 80% electron efficiency in each momentum bin.

The impact of both RICH cuts on the amount of pion and proton tracks can be seen in Figure 5.9. While the rejection of protons by the ring cut is uniform over the full momentum range, in the case of pions its effectiveness decreases once the pion Cherenkov threshold of $p = 4.65\,\mathrm{GeV/c}$ is reached, leading to

a „bump“ in the momentum distribution at $p > 6\,\mathrm{GeV/c}$ (see blue curve in Figure 5.9a). Since these pions can be separated very well by the ANN up to $p \sim 8\,\mathrm{GeV/c}$, this bump shifts further towards higher momenta after the ANN cut.

The suppression factors are shown in Figure 5.10, calculated by dividing the momentum distributions before and after the cuts. These clearly demonstrate how the ring cut loses its pion rejection capabilities above their Cherenkov threshold and how the ANN manages to enhance and extend the suppression towards higher momenta until its effectiveness ultimately decreases as well. At low momenta, the ANN does not separate protons and pions very well from electrons, due to the increased multiple scattering and the resulting larger distance between the electron and its produced Cherenkov ring, as mentioned above.

PID with the TRD

The working principle of the TRD described described in detail in Section 3.2. Since they produce TR, electrons can be separated from heavier particles by their comparatively higher energy deposit in the detector. Using the energy deposits from multiple layers, the electron likelihood L_e is constructed according to Refs. [47, 66] but taking into account pions, protons and kaons as relevant hadronic background contributions:

$$L_e = \frac{P_e}{P_e + P_\pi + P_p + P_K} \tag{5.5}$$

With:

$$\begin{aligned} P_e &= \prod_{i=1}^{N} P(E_i|e) \quad P_\pi = \prod_{i=1}^{N} P(E_i|\pi) \\ P_p &= \prod_{i=1}^{N} P(E_i|p) \quad P_K = \prod_{i=1}^{N} P(E_i|K) \end{aligned} \tag{5.6}$$

Here, $P(E_i|X)$ denotes the probabilities of a particle X (e, π, p or K) to deposit the energy E_i in detector layer i of the N layers it passes through. These can be seen in Figure 5.11, which shows the energy deposit of electrons, pions and protons for different momenta. Kaons are omitted for readability, since they are the least abundant hadronic contribution and behave very similar to pions.

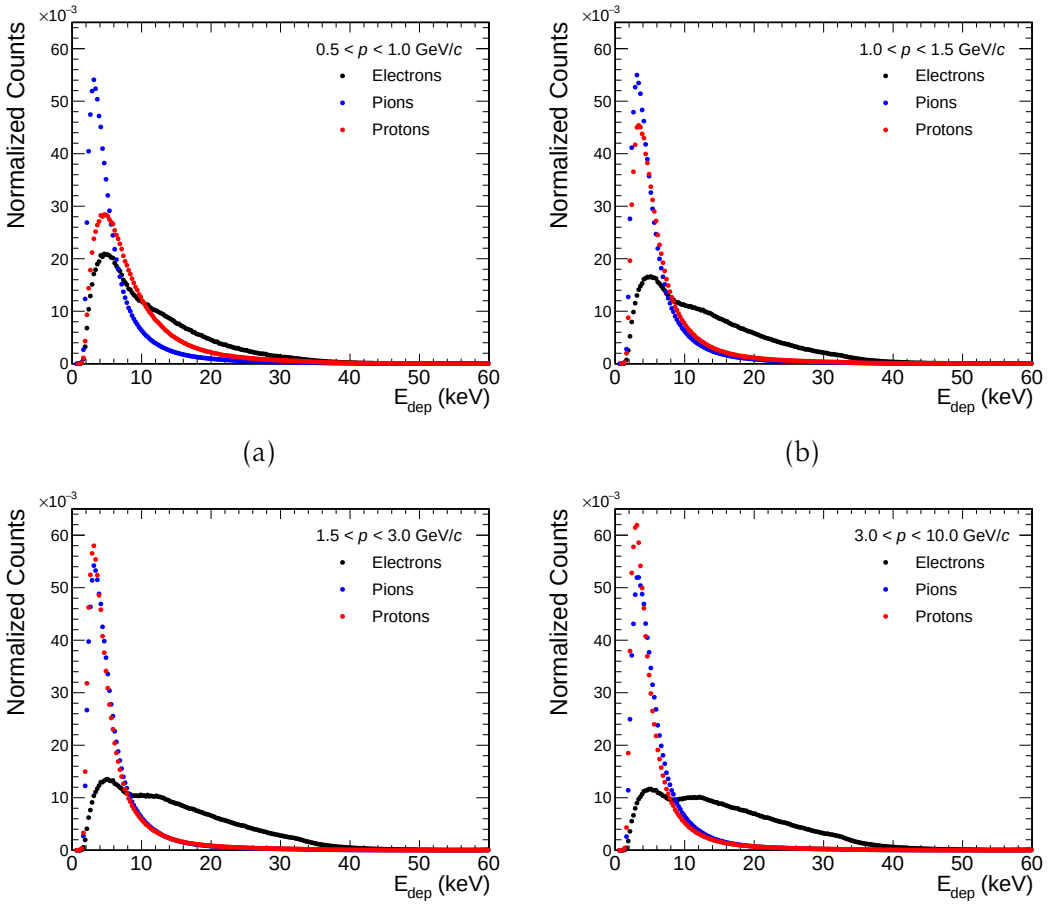

Figure 5.11.: Energy deposit of electrons, pions and protons in one TRD layer for different momentum classes.

Even at low momenta (Figure 5.11a), electrons already produce some TR, giving the spectrum a smeared out flank towards higher energy deposits compared to pions and protons, which then increases with momentum. While the deposited energy of pions stays unchanged over the whole range, for protons it slightly decreases with momentum (compare Figure 5.11a and Figure 5.11b) because the minimum of their specific energy loss in Xenon lies at $p \sim 3\,\mathrm{GeV/c}$ [41].

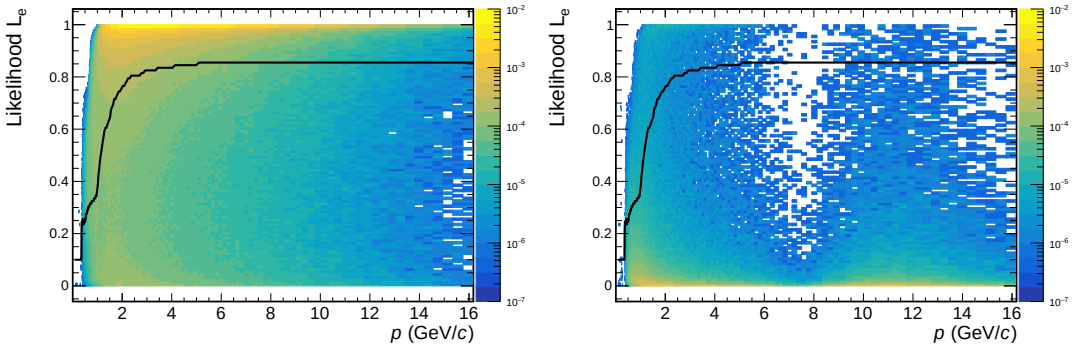

(a) Electrons (b) Pions

Figure 5.12.: Electron likelihood based on the energy deposited in the TRD layers for electrons (left) and pions (right) as a function of the particle momentum. The black line indicates a cut with 70 % electron efficiency in each momentum bin.

The electron likelihood for electrons and pions in the TRD as a function of the particle momentum are shown in Figure 5.12. Evidently, the particles are not well separated for low momenta, as could already be inferred from the large overlap of the energy deposit spectra at $p < 1\,\text{GeV/c}$ (see Figure 5.11a). This separation then increases until reaching a plateau at around $\sim 6\,\text{GeV/c}$. Applying a likelihood cut with an electron efficiency of 70 % in each momentum bin (black line in Figure 5.12) results in the momentum distributions for pions and protons shown in Figure 5.13. Due to the multiplicative nature of the probability calculation (Equation 5.6) each additional `TrdHit` in a given track increases the separation power. Therefore, also a cut requiring the number of `TrdHits` to be greater than two (`TrdHits`> 2) is implemented before the likelihood cut.

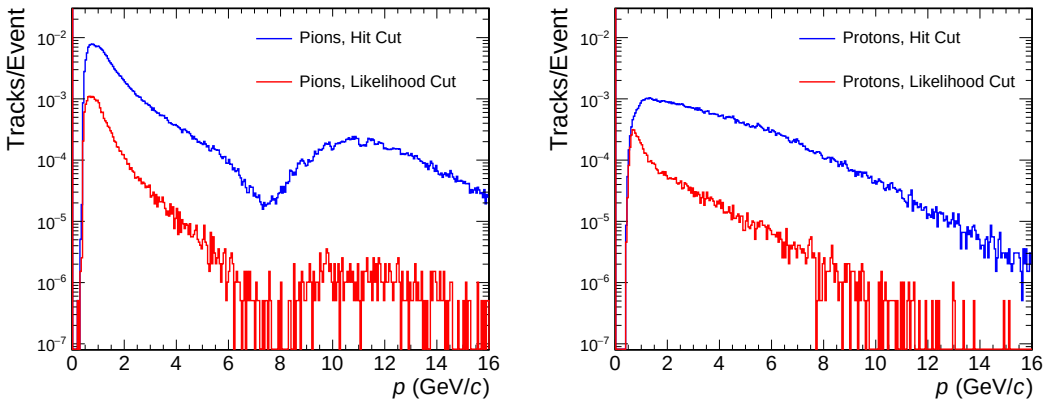

(a) Pions (b) Protons

Figure 5.13.: Momentum distribution of pion (left) and proton (right) tracks after the TRD cuts. The hit cut requires `TrdHits` > 2, while the likelihood cut is set to 70 % electron efficiency in each momentum bin.

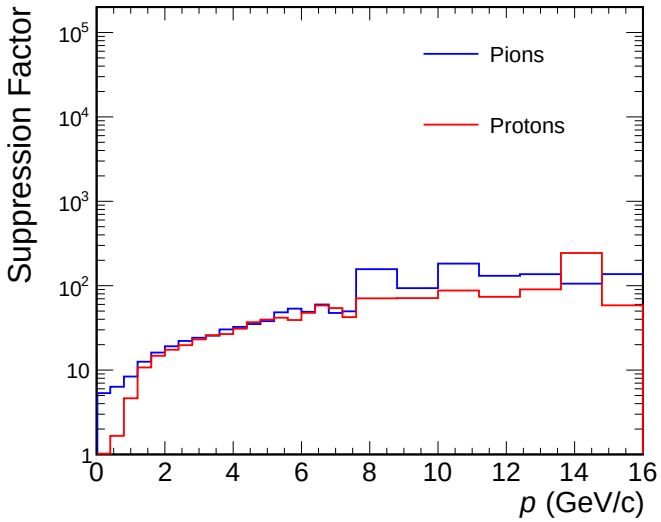

Figure 5.14.: Suppression factors of the TRD likelihood cut for pions and protons as a function of the momentum. The cut is set to an electron efficiency of 70 % in each momentum bin.

The suppression factors of the likelihood cut for pions and protons are shown in Figure 5.14. For both particles, the suppression increases with momentum up to a factor of ∼ 100. At low momenta the TRD still contributes to the pion suppression with a factor of 6 – 10, but loses virtually all of its separation ca-

pabilities for protons with $p < 1\,\mathrm{GeV/c}$ due to the large overlap of the energy deposit spectra (compare Figure 5.11a).

PID with the TOF

By using the time-of-flight t_{tof} of the particles measured with the TOF, the purity of the electron sample can be enhanced even further. With t_{tof} and the distance of the respective TOF layer to the collision point d_{tof}, the velocity v and its ratio to the speed of light $\beta = v/c$ for any given track can be calculated. The parameter used for the PID cut is the difference of this ratio β_{track} to the one expected for an electron at the momentum of the track:

$$\Delta\beta_{\mathrm{electron}} = \beta_{\mathrm{track}} - \beta_{\mathrm{electron}} = \frac{d_{\mathrm{tof}}}{t_{\mathrm{tof}} - t_0} \cdot \frac{1}{c} - \frac{p_{\mathrm{track}}}{\sqrt{m_e^2 + p_{\mathrm{track}}^2}} \tag{5.7}$$

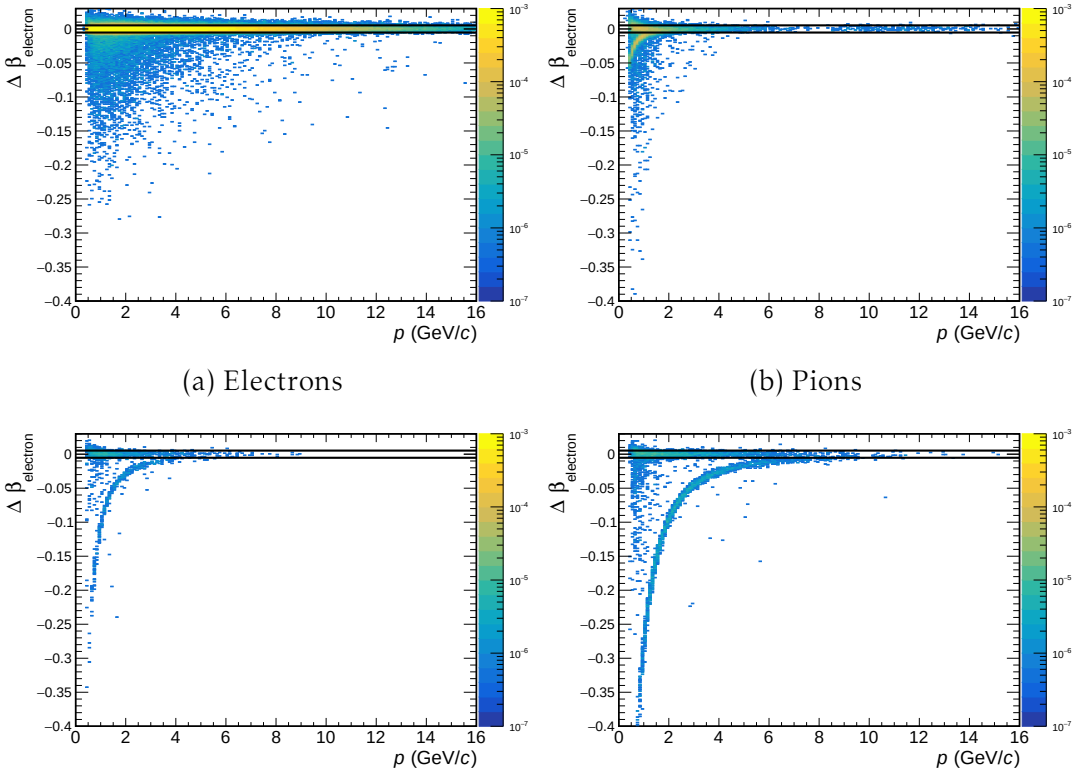

(a) Electrons (b) Pions

(c) Kaons (d) Protons

Figure 5.15.: $\Delta\beta_{\mathrm{electron}}$ calculated from the measured time-of-flight plotted against the particle momentum for electrons, pions, protons and kaons. The black lines indicate the lower and upper cut limit, with every track between the lines being accepted.

The values for $\Delta\beta_{\text{electron}}$ for electrons, pions, kaons and protons are shown as a function of the momentum in Figure 5.15. As expected, the $\Delta\beta_{\text{electron}}$ for electrons is centered around 0 and does not change with the momentum. For all other particles, a second, curved line can be seen in addition to the horizontal line at $\Delta\beta_{\text{electron}} = 0$. This is caused by the fact that at lower momenta, the rest mass of the respective particle is no longer negligible; The larger the mass, the lower its velocity at a given momentum, causing a measurable difference between the β for protons, kaons and pions and the β for electrons. Due to this mass dependence, the separation works over a large momentum range for protons, but only for $p \lesssim 1\,\text{GeV/c}$ for pions. The horizontal line at $\Delta\beta_{\text{electron}} = 0$, which is visible for all hadrons in Figure 5.15, is a result of mismatched hits, caused by faster particles (e.g. electrons from photon conversion in the detector material) producing additional hits in the TOF, which are then falsely attached to the hadron track.

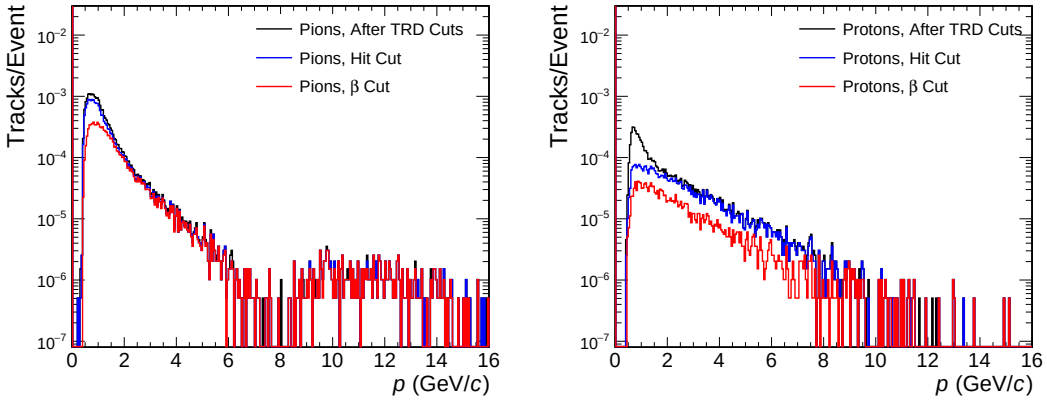

(a) Pions (b) Protons

Figure 5.16.: Momentum distribution of pion (left) and proton (right) tracks after the TOF cuts. The hit cut requires `TofHits`> 0, while the $\Delta\beta$ cut is set to $-5.28 \cdot 10^{-3} \leq \Delta\beta_{\text{electron}} \leq 5.28 \cdot 10^{-3}$.

For the cut, the range of $-5.28 \cdot 10^{-3} \leq \Delta\beta_{\text{electron}} \leq 5.28 \cdot 10^{-3}$ is chosen, leading to an electron efficiency of 93 % over the whole momentum range. The resulting momentum distributions of pions and protons, and the suppression factors of the TOF cuts are shown in Figure 5.16 and Figure 5.17, respectively. As mentioned above, the cut only contributes at very low momenta for pions due to their comparatively low mass. But as evident from Figure 5.16a, most remaining pions are situated in the low momentum range, rendering this cut still useful for pion suppression. For protons, the requirement of one `TofHit` already removes many of the low momentum tracks which passed the TRD likelihood cut. This is the case because of a lower matching efficiency of `TofHits` to `StsTracks` in this momentum range for protons, as the matching

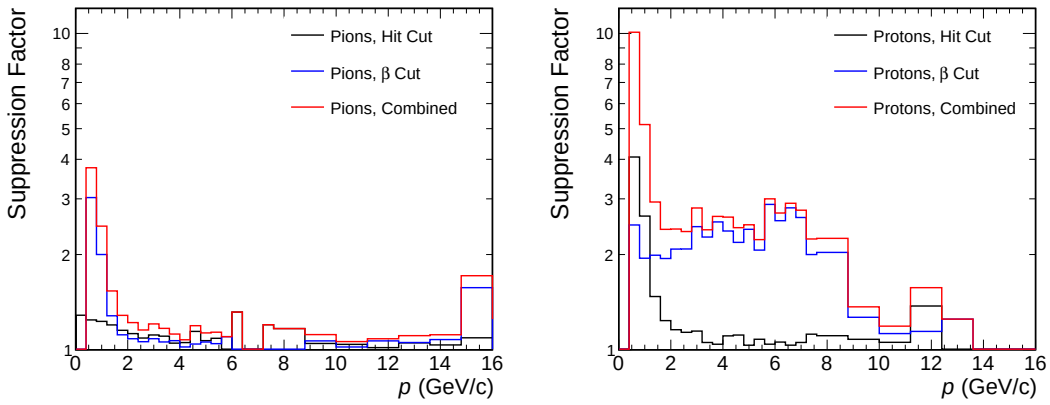

(a) Pions (b) Protons

Figure 5.17.: Suppression factors of the TOF cuts for pions and protons as a function of the momentum.

is carried out assuming a pion and the mass difference between pions and protons becomes more relevant at lower track momentum. The β cut then adds a factor of ~ 2 of proton suppression for tracks with $p \lesssim 8\,\mathrm{GeV/c}$, where the difference between the β for protons and electrons becomes negligible, as can be seen by the merging of the horizontal and the curved line in Figure 5.16b. Therefore, even with its limitations due to mismatches, the TOF β cut is a suitable addition to the cuts using the main subsystems for electron identification, i.e. RICH and TRD.

PID with the STS

Even though the STS is primarily used as a tracking device, it may also contribute to the rejection of non-electron tracks by making use of the multiple energy deposits measured in its layers.

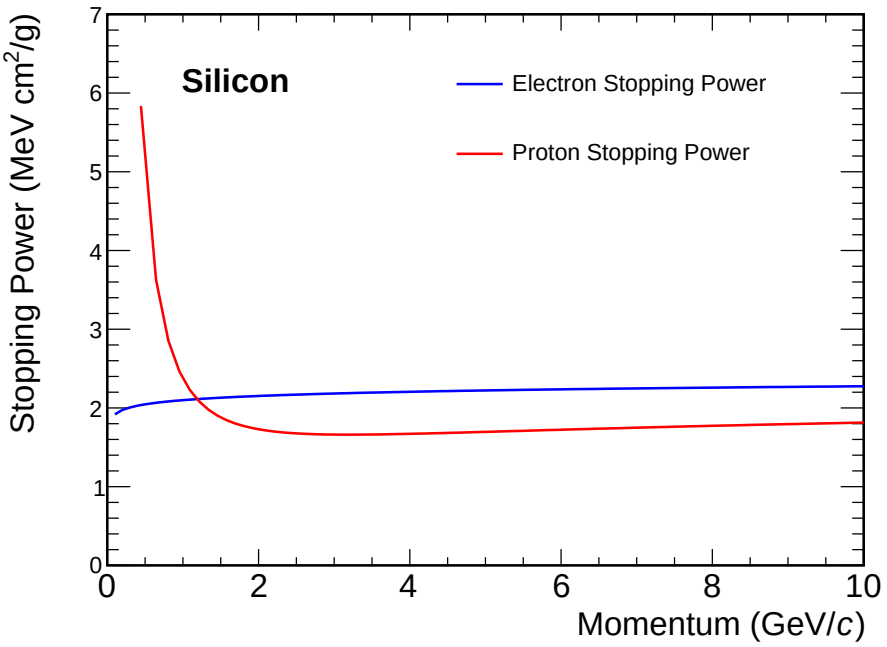

Figure 5.18.: Stopping power of Silicon for electrons and protons plotted against the particle momentum. Data taken from the NIST data base [41].

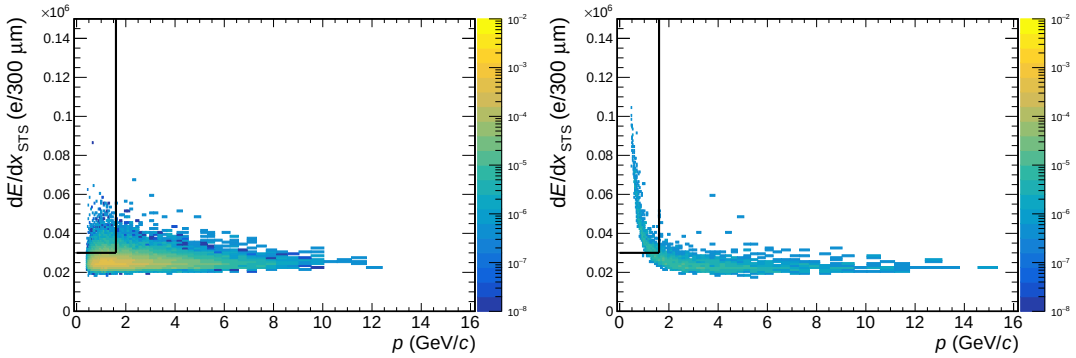

(a) Electrons (b) Protons

Figure 5.19.: Median energy deposit of electrons (left) and protons (right) in the STS plotted against the particle momentum. The black line indicates the implemented cut rejecting all tracks in the top left corner.

One can exploit the fact that protons at low momenta ($p \lesssim 1.5\,\mathrm{GeV/c}$) do no longer behave as MIPs in Silicon and therefore deposit a larger amount of energy than electrons, as shown in Figure 5.18. Since the distribution

of energy deposition has a Landau-shape and therefore a large tail towards higher values, it is useful to use the median of the measured energy in each station instead of a mean value. This median is plotted against the momentum for electrons and protons in Figure 5.19, which evidently follows the expected distributions from Figure 5.18. While a clear separation can only be achieved at low momenta, the low momentum range is the one with the most remaining protons. A further advantage of this PID method is that it is not affected as strongly by electron hits falsely attached to the track, as e.g. the TOF β cut. The black line in Figure 5.19 shows the chosen cut requiring $\mathrm{d}E/\mathrm{d}x_{\mathrm{STS}} < 3 \times 10^4\,\mathrm{e}/300\mu\mathrm{m}$ in the range of $0 \leq p \leq 1.6\,\mathrm{GeV/c}$, which results in an electron efficiency of 93 % in that range.

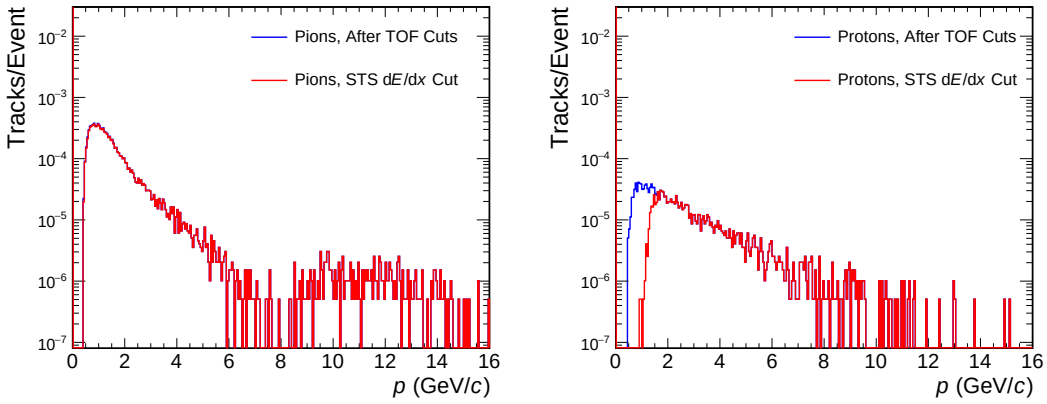

(a) Pions (b) Protons

Figure 5.20.: Momentum distribution of pion (left) and proton (right) tracks before and after the STS cut.

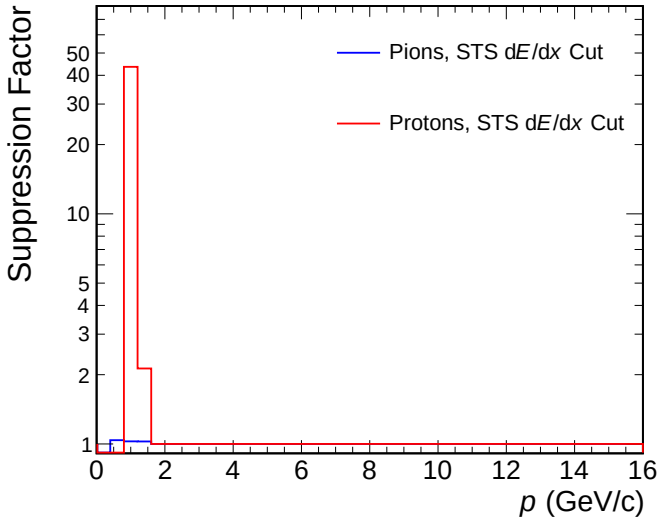

Figure 5.21.: Suppression factors of the STS dE/dx cut for pions and protons as a function of the momentum. Note that no suppression factor could be calculated for the lowest two bins for protons, as **all** remaining proton tracks in this range are removed by the cut.

The momentum distribution of the remaining protons and the achieved suppression can be seen in Figure 5.20 and Figure 5.21. While pions remain practically untouched (i.e. pion suppression ≈ 1), the amount of proton tracks at momenta below $\sim 1.5\,\mathrm{GeV/c}$ are drastically reduced.

Achieved Combined Hadron Suppression

The total achieved hadron suppression and electron efficiency can be calculated by the ratio of the tracks before and after the PID cuts. Naturally, the exact number will depend on the definition of what constitutes a PID cut. For example, by including cuts on a certain amount of hits in a given detecto, the resulting suppression factor will be strongly influenced by the acceptance and reconstruction efficiency of said detector. Therefore, these cuts are often classified as *reconstruction* cuts instead of PID cuts. However, the cut on the number of `RichHits` (i.e. the existence of a Cherenkov ring) should be included into the calculation, since it clearly contributes to the suppression of hadrons. Furthermore, even though requiring 3 or more `TrdHits` and a `TofHit` should *in theory* reduce the number of electron and hadron tracks to a similar degree, differences between particles may arise from varying efficiencies in reconstruction and/or matching. For the TOF reconstruction cut it was shown above (see Figure 5.16b) that it contributes to the reduction of low momentum protons, and also the TRD shows a slightly higher efficiency for electrons than hadrons (see Figure A.17). In these cases this is

not caused by the inherent PID capabilities of the detectors themselves, but rather by the software which might change in the future. However, the low momentum protons which are currently rejected by the cut on a `TofHit` (see Figure 5.16b) will most likely be rejected by the β or STS $\mathrm{d}E/\mathrm{d}x$ cut in case of an improvement of the track matching. For this reason, the values have been calculated one time with the inclusion of TRD and TOF reconstruction cuts and separately also only for *pure* PID cuts for a more conservative estimate.

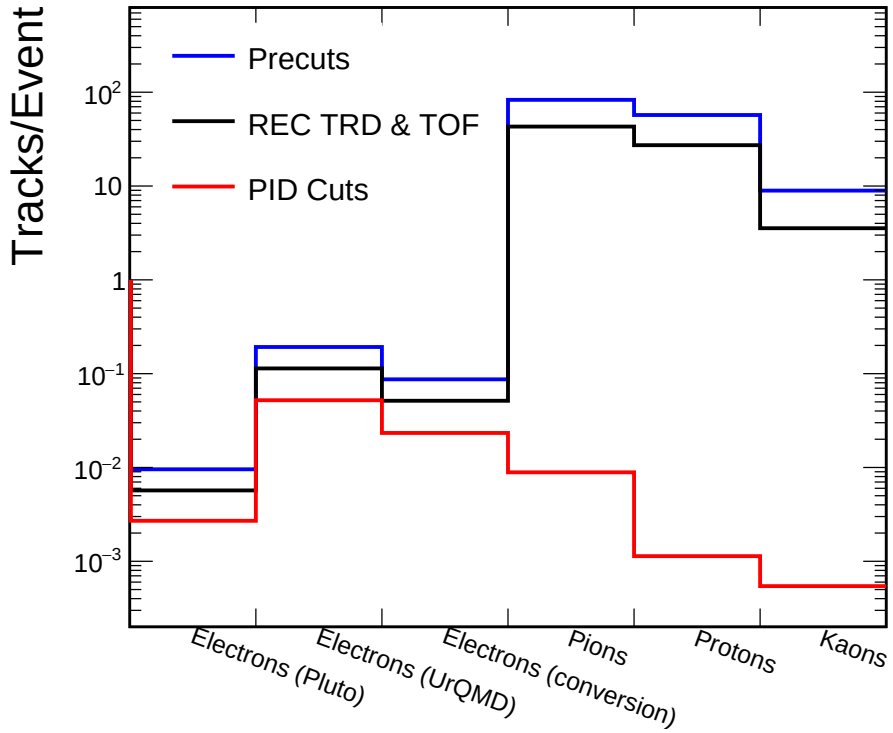

Figure 5.22.: Amount of tracks per event of different particle species and sources after different cut groups. The used cuts are summarized in Table A.5.

Table 5.4.: Momentum integrated total suppression factors achieved with different cut groups. The used cuts are summarized in Table A.5.

Particle	Sup. Factor (REC + PID)	Sup. Factor (Only PID)
Electrons (Pluto)	3.54	2.11
Electrons (UrQMD)	3.69	2.18
Electrons (Conversion)	3.73	2.20
Pions	9338	4845
Protons	50361	24017
Kaons	16438	6531

The amount of remaining tracks per event for different particles before and after the cuts described above is shown in Figure 5.22.Evidently, the cuts manage to reduce the hadronic background by 3 to 4 orders of magnitude, resulting in less proton and kaon tracks than electron tracks from Pluto. The total suppression factors are summarized in Table 5.4, which for electrons translate to efficiencies of 47 % (Pluto), 46 % (UrQMD) and 45 % (conversion) in the case of the pure PID cuts.

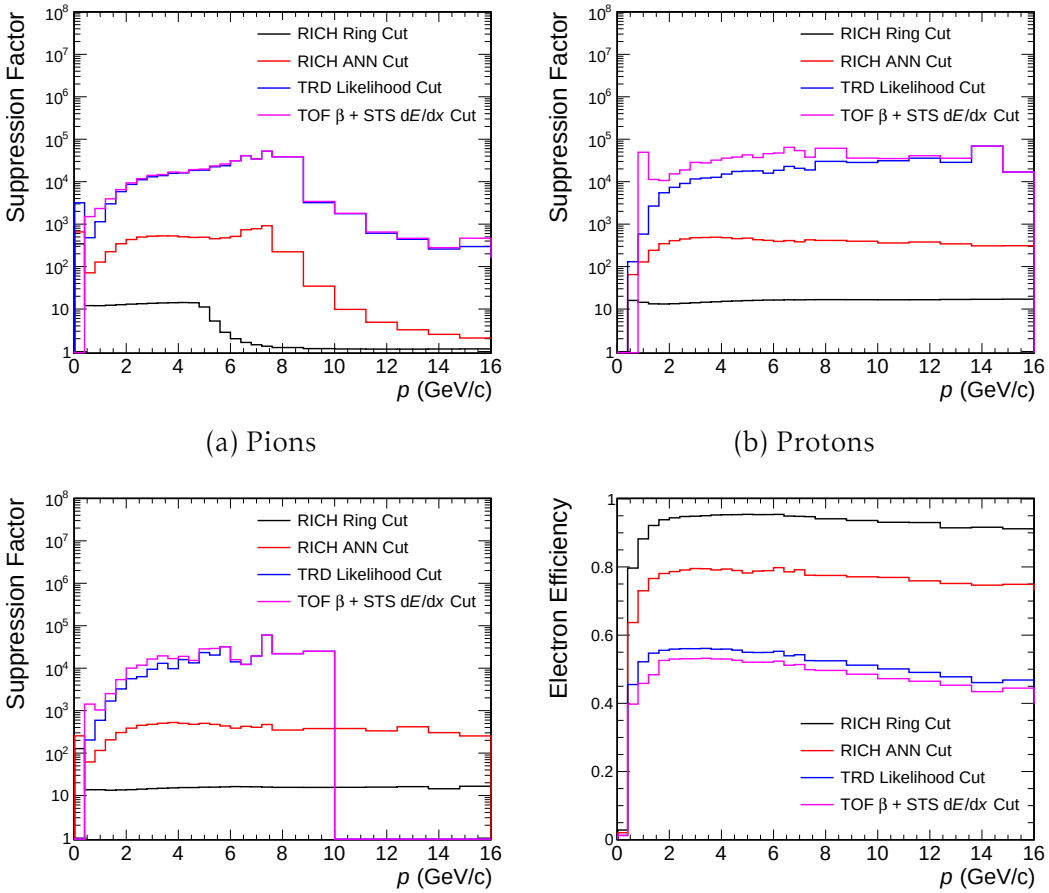

(a) Pions

(b) Protons

(c) Kaons

(d) Electrons

Figure 5.23.: Momentum dependent suppression factors for different hadrons, and electron efficiency achieved with all PID cuts. To increase readability the cuts using TOF and STS are combined into one step. Note that for protons and kaons with $p < 0.8\,\mathrm{GeV/c}$ as well as kaons with $p > 10\,\mathrm{GeV/c}$ no suppression factor could be calculated because no tracks survive the cuts in these momentum ranges.

The momentum dependence of the PID cuts for different particles is shown

in Figure 5.23. As discussed already, the RICH ring cut does not reject high momentum pions, which is mitigated first by the RICH ANN and then by the TRD likelihood cut. For protons and kaons, the RICH and TRD cuts show similar effectiveness, but since the TOF and STS cuts work better for protons, the total suppression for protons is the highest of all hadron species (see Table 5.4). The momentum dependence of the electron efficiency (Figure 5.23d) is primarily shaped by the RICH ring cut, as acceptance and ring-to-track matching efficiency are both reduced at lower momenta.

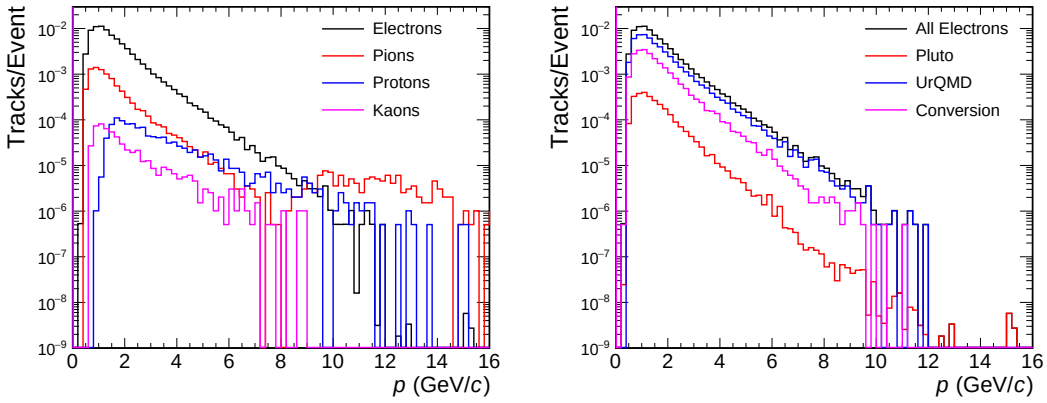

(a) Particle Species

(b) Electron Sources

Figure 5.24.: Momentum distribution of different particle species (left) and different electron sources (right) after all PID cuts.

As shown in Figure 5.24a, the remaining hadronic background consists predominantly of pions with relatively low momenta ($0.5\,\mathrm{GeV/c} \lesssim p \lesssim 1.5\,\mathrm{GeV/c}$). On the one hand, this is caused by the momentum distribution of pions before the PID cuts peaking at $p \sim 1.2\,\mathrm{GeV/c}$ (see Figure 5.9a), but on the other hand also a result of the comparatively low pion suppression in this momentum range. While the RICH ring cut does not show a reduced effectiveness at small momenta, both the RICH ANN cut and the TRD likelihood cut perform worse for $p \lesssim 2\,\mathrm{GeV/c}$, the former due to increased multiple scattering, the latter due to low TR yield. Although this is also true for other particles at low momenta, for protons it is successfully mitigated by the TOF and STS cuts (see Figure 5.23b) and kaons already form the smallest contribution to begin with. Thus, any further improvement to the PID should focus on further suppression of low momentum pions.

5.3.1.2. Machine Learning Method

As stated in the beginning of Section 5.3.1, the idea of an ML approach to hadron rejection is to make use of the same information as with conventional

cuts, but instead of several subsequent cuts, all parameters are compiled into one single „probability-like“ value by an ML classifier on the basis of which a single momentum dependent PID cut can be implemented. In the context of dielectron analysis for the CBM experiment, this method has been studied by Etienne Bechtel in Ref. [55] using ANNs, and by Henrik Schiller in Ref. [65], where several ML architectures were compared and a decision tree classifier based on the *eXtreme Gradient Boosting* (`XGBoost`)[7] [67] library performed best.

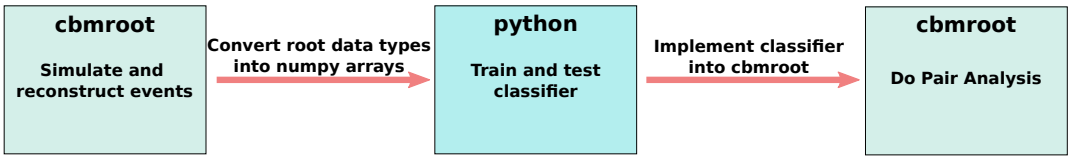

Figure 5.25.: Sketch of the procedure to generate ML classifiers based on data simulated with `cbmroot` and to use them in PAPA.

Since one of the most widespread development language for ML is python, a framework was developed in Ref. [65] to convert the data simulated and reconstructed with `cbmroot` into python data types, which can then be used to train and test a classifier with common python libraries. Afterwards the classifier can be exported into a `.C` file and implemented into `cbmroot`, where a full dielectron pair analysis can be performed with PAPA. However, this functionality was added by Henrik Schiller after the thesis submission, and therefore not tested before this thesis. Instead, the pair analyses carried out in Ref. [65] were performed inside the python framework on a smaller data set with limited statistics and therefore function rather as a proof of principle. Thus, in this work a new classifier was trained with an increased amount of training data and, for the first time, implemented into `cbmroot` and tested in a full pair analysis using PAPA.

Ensemble Classifiers and XGBoost

In principle, `XGBoost` is a software library to create and optimize so-called „ensemble classifiers“, which consist of a multitude of smaller, less complex classifiers. In the case of `XGBoost` these basic building blocks are regression trees, i.e. decision trees which output a continuous score [67]. For the application in this thesis this is preferred, since a continuous output value comparable to the probability of a track being an electron gives the user the opportunity to set a desired cut-off point to control electron efficiency and/or hadron suppression, instead of relying on a binary classification.

[7] https://github.com/dmlc/xgboost

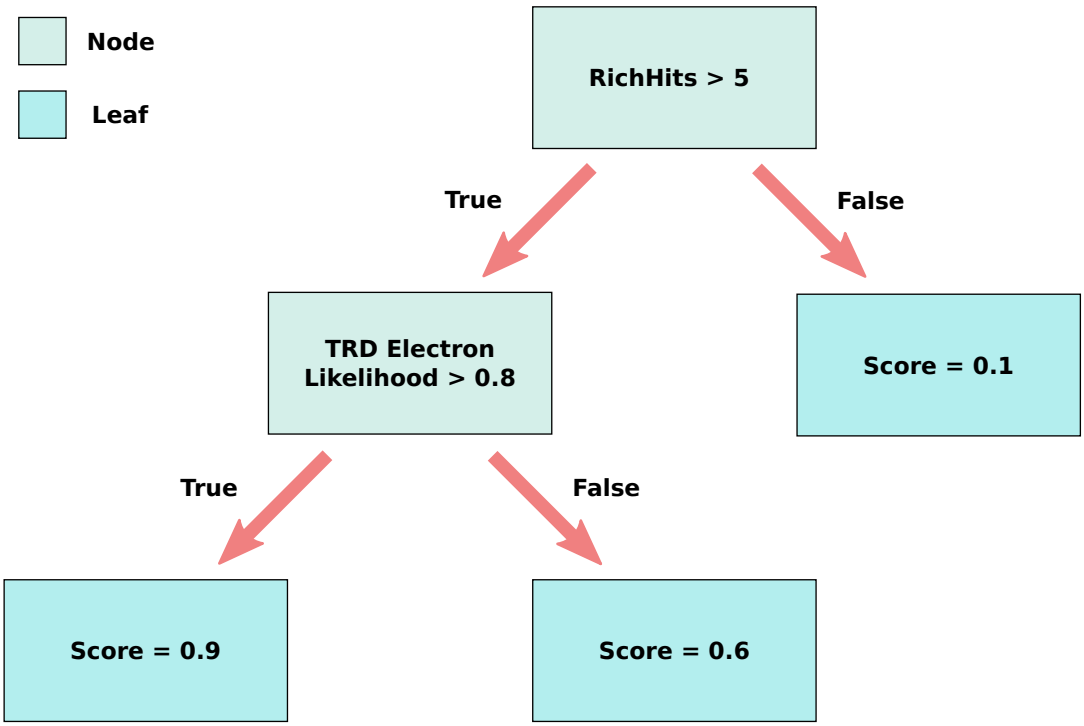

Figure 5.26.: Sketch of an exemplary regression tree with arbitrary values as output scores. The user can apply a cut at any output value and is therefore able to set the electron efficiency to a desired value.

An example of such a regression tree is shown in Figure 5.26. For each track, one simply moves down from the top and checks the binary conditions at the splitting points called *nodes* until a *leaf* is reached, at which no further condition is checked and a score is assigned. While one could already build a classifier with a single regression tree, this tree would become very complex due to the large number of input variables, increasing computing time and being more prone to overfitting. Instead, one builds an ensemble classifier consisting of a multitude of shallow regression trees, whose individual output scores are combined into one final score by a weighted sum. From a computing standpoint, this is clearly advantageous because all trees can be evaluated in parallel, reducing the evaluation time per track. On the other hand, ensemble classifiers are also able to outperform single classifiers in terms of pure classification accuracy [68]. `XGBoost` constructs such an ensemble classifier using the so-called *boosting* method: Starting with a single shallow regression tree, more and more trees are added to the ensemble iteratively, with each new tree correcting the errors of the previous ones, improving the classification accuracy as shown schematically in Figure 5.27 and explained for an example case in Section A.2. An ensemble classifier constructed in such a way is also referred to as Boosted Decision Tree (BDT) classifier.

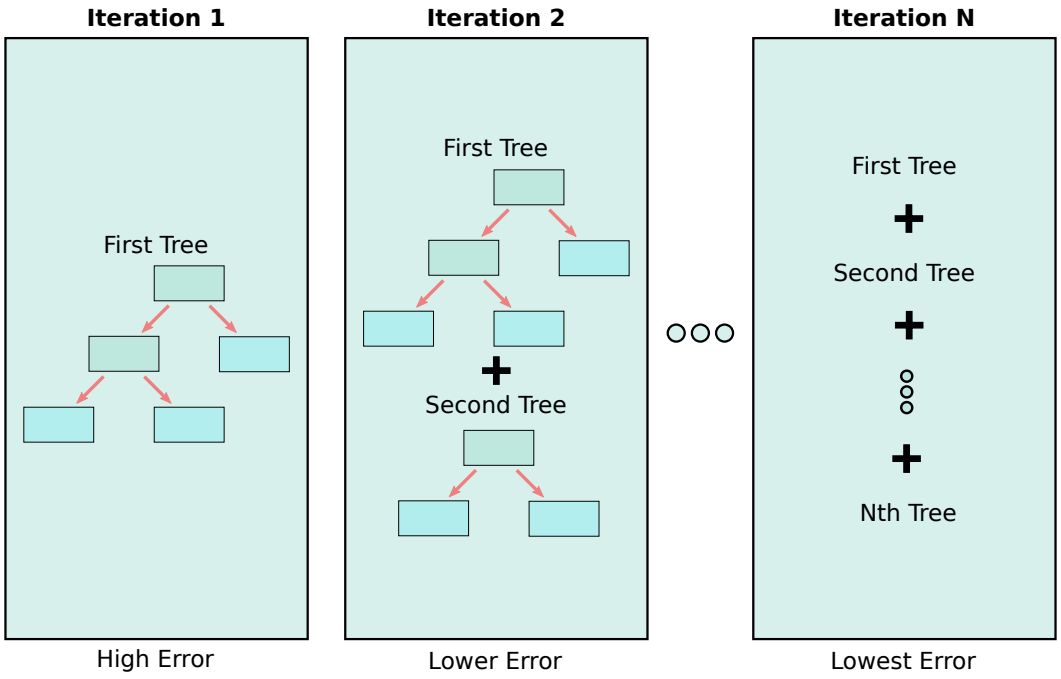

Figure 5.27.: Sketch of the iterative tree boosting procedure used by `XGBoost` to construct an ensemble classifier consisting of several shallow regression trees. Adapted from [69].

A unique characteristic of `XGBoost` is the fact that the *learning objective* $\mathcal{L}$, the function which is minimized in the boosting process, does not only depend on the prediction accuracy but also on the model complexity. It is constructed as follows:

$$\mathcal{L} = \underbrace{\text{loss term}}_{\text{increases with prediction error}} + \underbrace{\text{regularization term}}_{\text{increases with tree complexity}} . \tag{5.8}$$

A new tree is only added to the ensemble if it further reduces $\mathcal{L}$. The regularization term will cause the algorithm to prefer simpler models and avoid overfitting [67]. Another useful feature of `XGBoost` is that its tree building algorithm is *sparsity-aware*, i.e. it learns how to handle missing entries in the input data [67]. This is especially useful for the application in this work, since, for example, not every track has a reconstructed energy loss in the forth TRD station, and a missing entry there should be treated differently than $E_{\text{TRD }3} = 0\,\text{keV}$.

Used Classifier

As input for the classifier 21 track parameters were chosen in total, those being 18 of the 19 parameters used in Ref. [65] (all except the χ^2/NDF to Vertex), with the addition of the number of hits in MVD, the number of hits in STS, and the energy loss in the STS. The full list of parameters can be found in Table 5.5.

Table 5.5.: Track parameters used as inputs for the classifier trained with `XGBoost`.

Category	Parameter
Global Parameters	p, θ, φ, Charge
STS/MVD Parameters	MVDHits, STSHits, STSEloss
RICH Parameters	RICHHits, χ^2/NDF_{RICH}, A Axis, B Axis, ϕ_{RICH}, Θ_{RICH}, r, d
TRD Parameters	TRDHits, $E_{\text{TRD }0}, E_{\text{TRD }1}, E_{\text{TRD }2}, E_{\text{TRD }3}$
TOF Parameters	$\Delta\beta_{\text{Electron}}$

The used parameters are:

- **Global Parameters:**
  - p : momentum of the track at the vertex
  - θ : azimuthal angle of the track at vertex
  - φ : polar angle of the track at vertex
  - Charge: Charge of the track/particle
- **STS/MVD Parameters:**
  - MVDHits : Number of hits in the MVD
  - STSHits : Number of hits in the STS
  - STSEloss : Median of the energy deposited by the track in each STS station
- **RICH Parameters:**
  - Parameters characterizing the Cherenkov ring produced in the RICH as shown in Figure 5.7 and Table 5.3

- **TRD Parameters:**
  - TRDHits : Number of hits in the TRD
  - $E_{\text{TRD i}}$: Energy deposited in TRD layer i
- **TOF Parameters:**
  - $\Delta\beta_{\text{Electron}}$: Difference between β of the track and β expected for an electron at the momentum of the track

After choosing the parameters, the training data had to be prepared. Since the classifier should not be trained on the same data set on which it will be applied on, a new set of 180.000 collisions was simulated, using identical input parameters as for the „main“ data set (see Section 5.2). The reconstructed tracks were then converted into data types readable with python and ported into the framework for the classifier training, as described in the beginning of Section 5.3.1.2.

Table 5.6.: List of cuts applied to the data before training the classifier to reduce the amount of „noise“ tracks which will be discarded by reconstruction cuts in the analysis anyway.

Cut
Nr. of `STSHits+MVDHits` > 3
χ^2/NDF to vertex < 3
Nr. of `RICHHits` > 5
Nr. of `TRDHits` > 2
Nr. of `TOFHits` > 0

However, not all tracks are useful for training: The aim for the classifier in this work is to replace the conventional PID cuts, thus it makes sense to train the model only on tracks containing information from the PID detectors and which fulfill other basic quality conditions. The chosen pre training cuts are summarized in Table 5.6. Furthermore, the weighting of the tracks had to be considered: Since each decay simulated with Pluto (see Table 5.1) is added once per event, the number of electron tracks coming from these sources are greatly enhanced compared to the electrons produced by UrQMD or GEANT. However, this is considered to be beneficial, since electrons from thermal radiation and vector meson decays are the most important for this analysis and the classifier should be as sensitive as possible to them. Therefore, now reweighting of the tracks depending on their source has been performed for the training process.
After filtering, the remaining ~ 300.000 electron and ~ 850.000 hadron tracks were devided into a *training* and *testing* data set with a ratio of 50 : 50. Then

the hyperparameters of the model were optimized using *Bayesian Optimization*[8].

Table 5.7.: Hyperparameters of the classifier training process optimized with *Bayesian Optimization*, except `num_boost_rounds` which was set manually. For a more detailed explanation of the parameters, see `XGBoost` parameter documentation[9]

Hyperparameter	Explanation	Value
`max_depth`	Maximum depth of a tree	7.54
`min_split_loss`	Minimum required loss reduction for a new node on a tree	0.29
`reg_alpha`	„Strength“ of the regularization term	15.00
`learning_rate`	“Strength“ of how much each new tree new tree alters the previous result	0.47
`num_boost_rounds`	Number of boosting iterations (see Figure 5.27)	150

The number of boosting iterations was set to 150 which served as a functional compromise between the size of the model and its accuracy. The classifier was then trained using these parameters and a first evaluation was performed already inside the python framework using the *testing* part of the data set. One method to visualize the classification accuracy is the Receiver Operating Characteristic (ROC) curve, generally showing the relation between false positive and true positive rate, which in the case of this work correspond to the hadron contamination and electron efficiency, respectively.

[8] https://github.com/bayesian-optimization/BayesianOptimization
[9] https://xgboost.readthedocs.io/en/stable/parameter.html

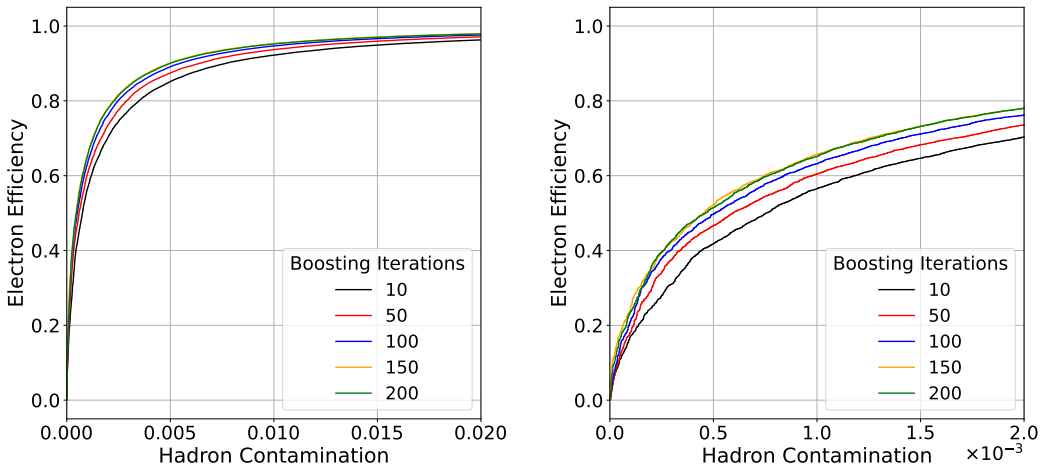

Figure 5.28.: ROC curves of trained classifiers with different number of boosting iterations. The right plot is a zoomed-in version of the left plot.

ROC curves for classifiers with different number of boosting iterations are shown in Figure 5.28. In general, the classifiers show very low false positive rates at high electron efficiency. However, with increasing number of trees, the classifier performance approaches a plateau where adding more trees does no longer result in any improvement. For this reason the parameter for the number of trees was set to `num_boost_rounds` = 150.

Achieved Hadron Suppression

The trained classifier was exported as a `.C` file and then implemented into `cbmroot`, making it accessible by PAPA. Subsequently, a full pair analysis was performed on the same data set which was used in the section describing the hadron rejection based on conventional cuts (Section 5.3.1.1). Since the task of the classifier is only the PID, pre cuts and reconstruction cuts are still necessary and have been implemented as well. The RICH ring cut, being a mixture of reconstruction and PID cut, was included too, also to increase comparability with the results of the previous sections.

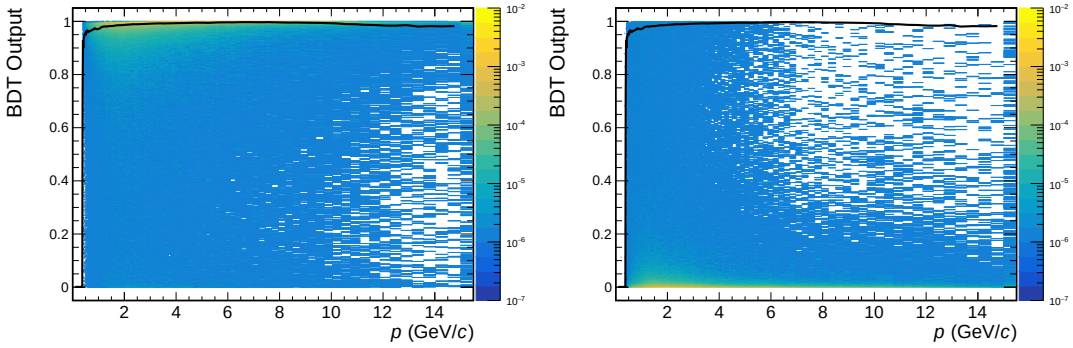

(a) Electrons

(b) Pions

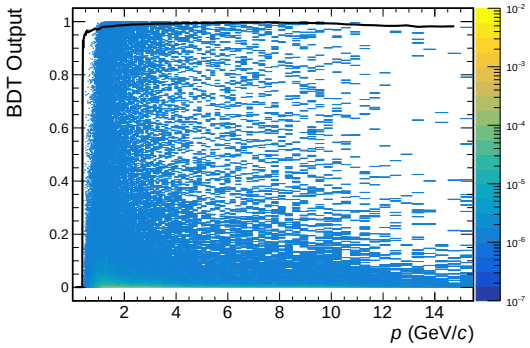

(c) Kaons

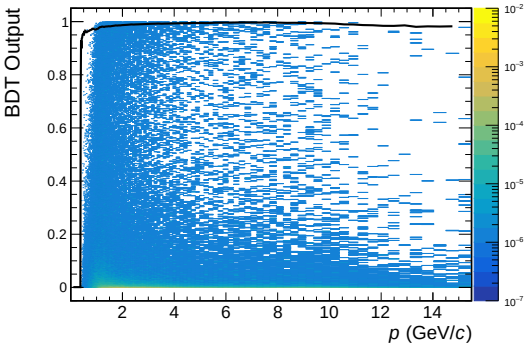

(d) Protons

Figure 5.29.: Output of the trained classifier as a function of the momentum for different particle species. The black line indicates the implemented cut with 50 % electron efficiency in each momentum bin.

The output scores of the ML classifier for different particles are shown in Figure 5.29 with the black lines indicating a cut at 50 % electron efficiency. The efficiency was chosen to be as close as possible to the one of the conventional PID cuts for comparability. Evidently, the classifier works exceptionally well, assigning values close to 1 to most electrons and values close to 0 to most hadrons. The cut at 50 % electron efficiency lies at a value of BDT score > 0.97 for most of the momentum range, only visibly deviating from this at low momenta ($p \lesssim 1.5\,\mathrm{GeV/c}$), as can be seen in the top left corner of Figure 5.29a. Most protons and kaons in this momentum range are assigned very low scores, however, a non-negligible amount of pions does lie above the cut line (top left corner of Figure 5.29b).

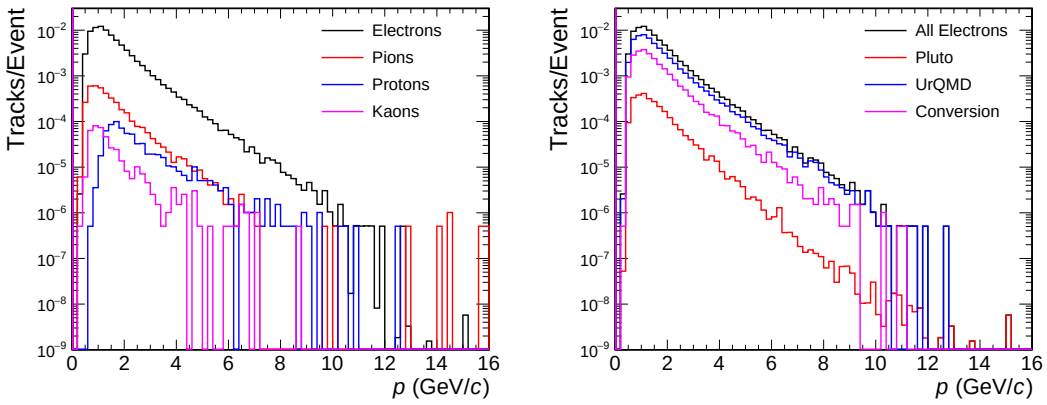

(a) Particle Species (b) Electron Sources

Figure 5.30.: Momentum distribution of different particle species (left) and different electron sources (right) after the PID cut using the ML classifier.

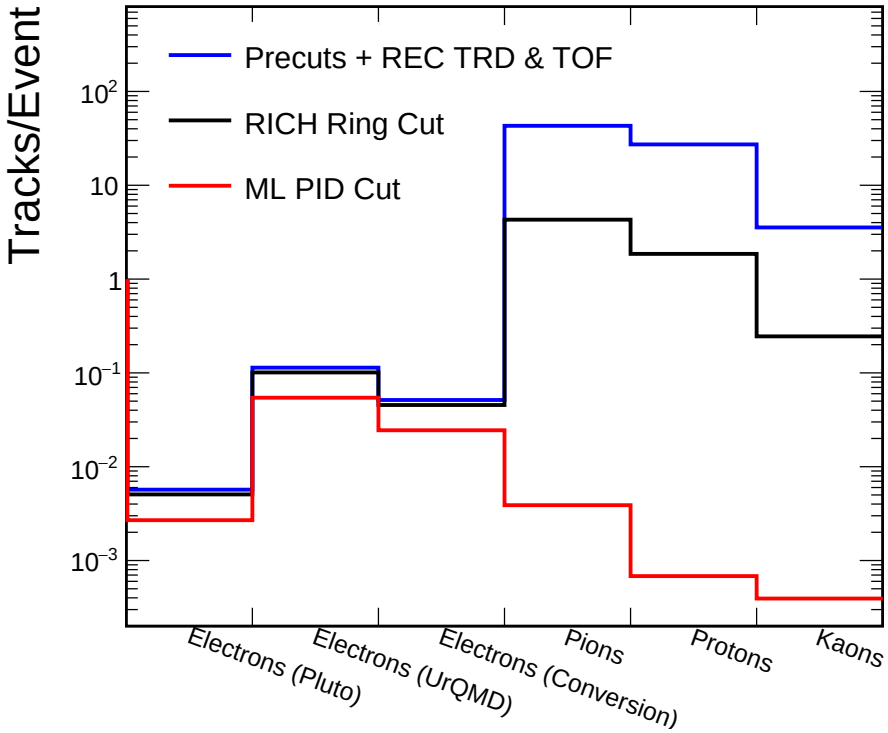

Figure 5.31.: Amount of tracks per event of different particle species and sources after different cut groups using a ML classifier. The used cuts are summarized in Table A.6.

This can be seen more clearly when examining the momentum distribution of the remaining particles after the cut (Figure 5.30a). Pions form the largest remaining hadronic background component, predominantly at low momenta. Still, the pion suppression achieved with the ML classifier is sufficiently high for the remaining number of pion tracks to be in the same order of magnitude as the electron tracks embedded with Pluto, with a ratio of about 3 : 4 for $e_{\text{Pluto}} : \pi$ (Compare Figure 5.30a and Figure 5.30b). This is clearly visible when integrating over the momentum range (Figure 5.31), with pions being in the same order of magnitude as Pluto electrons, and protons and kaons one order of magnitude below after all cuts have been applied.

Table 5.8.: Momentum integrated total suppression factors achieved using a ML classifier for PID. The used cuts are summarized in Table A.6.

Particle	Sup. Factor (RICH Ring + ML PID Cut)
Electrons (Pluto)	2.12
Electrons (UrQMD)	2.09
Electrons (Conversion)	2.10
Pions	11062
Protons	39939
Kaons	9025

The suppression factors for the different particles calculated by taking the ratio of tracks before and after the cuts are summarized in table Table 5.8. Since the RICH ring cut is included these can be directly compared to the factors achieved with the conventional PID cuts shown in the right column of Table 5.4.

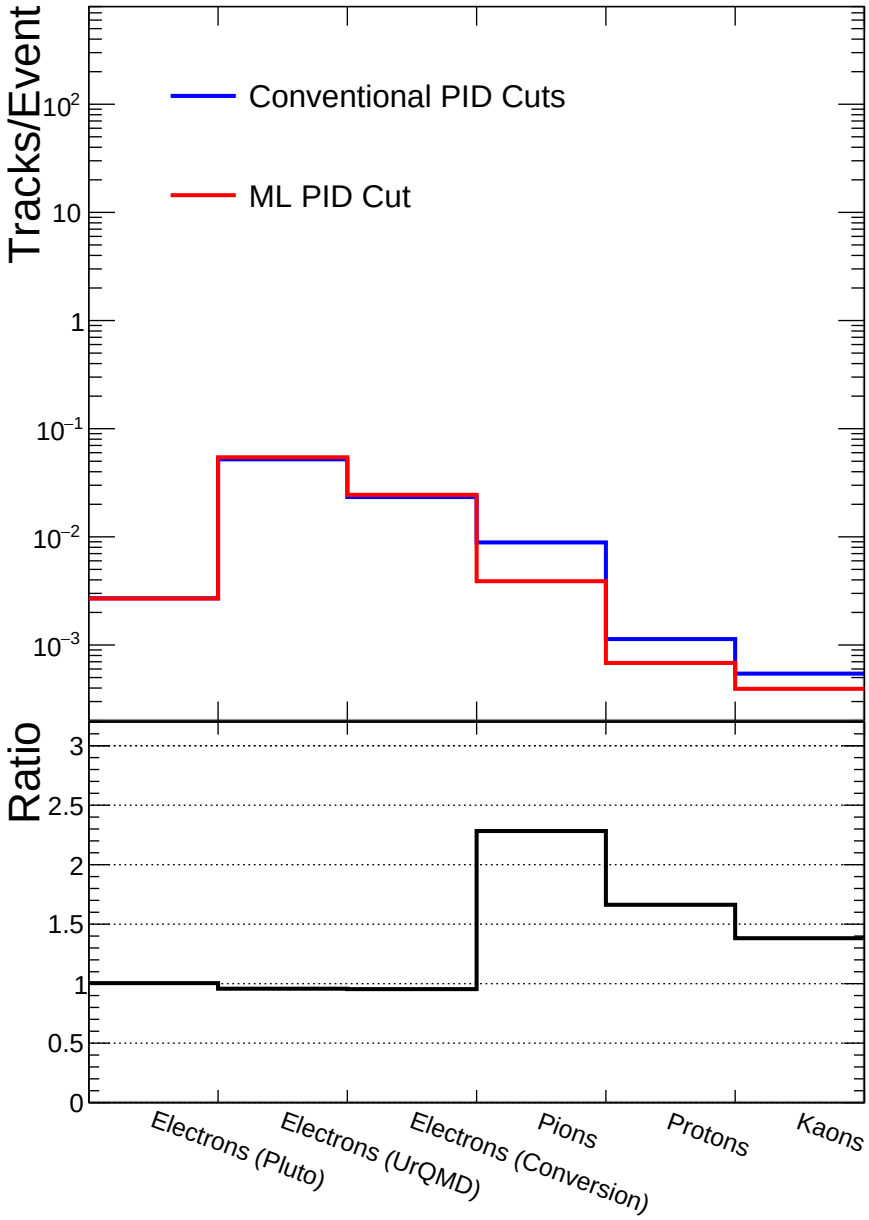

Figure 5.32.: Amount of tracks per event of different particle species and sources after the conventional PID cuts and using the ML classifier with a ratio of the two. The used cuts are summarized in Table A.5 and Table A.6.

A direct comparison of the remaining particle tracks is shown in Figure 5.32. As can be seen, at similar electron efficiency the ML classifier provides comparable, but slightly higher suppression of hadrons as the used conventional

cuts. This improvement is the largest for pions with an increase by a factor of 2.3, while the proton and kaon suppression increases by factors of 1.7 and 1.4, respectively. Thus, the machine learning classifier is able to enhance the purity of the final electron sample and provides a viable alternative to conventional PID cuts. Its impact on the resulting dielectron spectra and signal-to-background ratios will be described in Section 5.4.

5.3.2. Electron Background

Electron background in the context of dielectron analysis refers to electrons which do not contribute to the signal, but only to the combinatorial background in the invariant mass spectrum. By their nature of being electrons they are accepted by the PID cuts described in the above sections and have to be rejected with additional dedicated selections.
There are two main sources for background electrons:

1. **Photon Conversions:** Decays of $\gamma \xrightarrow[\text{material}]{} e^+e^-$, which may occur either in the target or in the detector material
2. **Incomplete Pairs:** Dielectron decays from any source, in which one of the daughters is missing in the final electron sample, either because it is not in detector acceptance or it is rejected by any applied cut

It is important to note that these categories are not mutually exclusive, since an incomplete pair can also result from a photon conversion. However, photon conversions need additional treatment, since also the complete pairs are considered background and should be removed.

5.3.2.1. Photon Conversion Rejection

One distinct feature of photon conversions is the low invariant mass of the resulting e^+e^- pair. To exploit this fact, one makes use of the `PairPreFilter` functionality of PAPA, as explained in Section 5.1: Pair candidates are built from all combinations of the track arrays of positively and negatively charged tracks, and a cut on the invariant mass of these candidates is applied. In this analysis, the cut threshold is set to $m_{\text{inv, candidate}} = 0.025\,\text{GeV/c}^2$, rejecting all tracks from pair candidates with masses below this limit. The effectiveness of this cut highly depends on its position in the cut sequence, since the decision as to whether a track is rejected is not only made on the basis of the parameters of the track itself, but also depends on the other tracks in the sample. In principle, it should be applied *after* all PID cuts, since a valid invariant mass can only be calculated once both tracks of the candidate have been identified as electrons. However, if the cut is applied late in the sequence, it may occur that one of the tracks of the $\gamma \rightarrow e^+e^-$ pair has already been rejected by a

previous cut, leaving the remaining track to form only random combinations which are likely to pass the cut threshold. Thus, the cut is applied before the PID cuts, calculating the invariant mass with the assumption that both tracks are electrons. If on the other hand the cut is applied early, many low momentum tracks are still in the sample, increasing the probability that random combinations with signal electrons lie below the cut threshold. Thus, a fitting position for this cut has to be found by comparing results for different orders. The best performance has been achieved by requiring, among other basic track quality properties, at least one hit in the TRD before applying the `PairPreFilter`. This cut ensures that many low momentum tracks are already removed before the `PairPreFilter`, which would be more likely to form random combinations with signal electrons with invariant masses below the threshold. A significant amount of signal tracks are still rejected by this cut even with the prior requirement of one `TrdHit`, however in the case of this analysis, due to the strong reduction of electrons from photon conversions as well as the „collateral damage“ i.e. the rejection of hadrons by random combinations, this cut has proven to improve the signal-to-background ratio. Nevertheless it should be used and tuned with care. More details on the optimization process can be found in Section A.3.

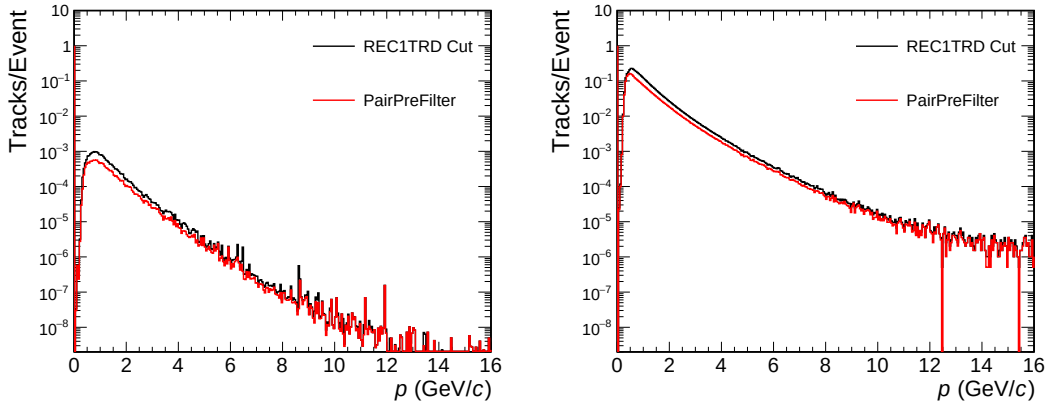

(a) Pluto Electrons (b) Conversion Electrons

Figure 5.33.: Momentum distribution of electrons before and after the `PairPreFilter`

Figure 5.33 shows the momentum distribution of electron tracks from Pluto and photon conversions before and after the pair cut. The momentum integrated efficiency of the cut in this case is 62 % for Pluto and 68 % for conversion electrons. Thus, the cut rejects more signal than background tracks, which at first glance seems counterproductive. However, many of the excluded conversion electrons cannot be rejected otherwise and stay in the final sample if the cut is applied later in the cut sequence. Therefore, this cut ulti-

mately leads to a higher ratio of Pluto to conversion electrons after applying all other cuts (See Section A.3).

Another property of conversion electrons useful for rejection is the fact that many are created in the detector material and not at the primary vertex. This can be exploited by requiring a certain amount of hits in the MVD as well as a low distance of the track projection to the vertex, i.e. its χ^2/NDF value.

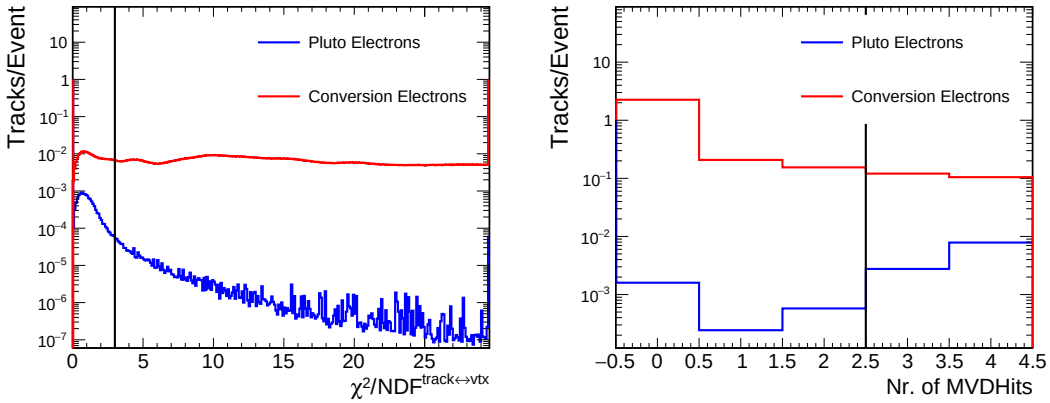

Figure 5.34.: Distributions of χ^2/NDF to primary vertex (left) and number of `MVDHits` (right) for Pluto and conversion electrons after the `PairPreFilter`. The black vertical lines indicate the cut thresholds.

Figure 5.34 shows the distribution of the χ^2/NDF to the primary vertex and the number of `MVDHits` for electrons from Pluto and photon conversions. As cut values, `MVDHits` > 2 and χ^2/NDF $\leq$ 3 have been chosen, indicated by the black vertical lines.

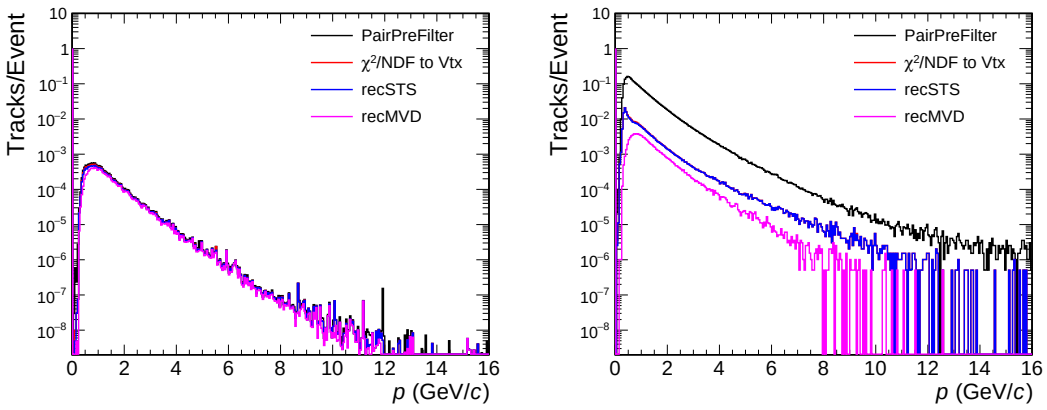

(a) Pluto Electrons (b) Conversion Electrons

Figure 5.35.: Momentum distribution of electrons before and after the cuts on χ^2/NDF, `STSHits` and `MVDHits`. The `recSTS` cut has very little impact and is only shown for the sake of completeness.

The momentum distributions of electrons from Pluto and conversion after these cuts are shown in Figure 5.35. As can be seen from Figure 5.35a, they exhibit an high Pluto electron efficiencies, namely 91.3 % for the χ^2 and 82.3 % for the `recMVD` cut. The electrons from conversions on the other hand are reduced substantially (see Figure 5.35b), by a factor of 11.4 and 2.8 respectively. One should note that these factors depend on the order in which the cuts are applied.

5.3.2.2. Incomplete Pairs and Decay Topology

As stated above, a second major source of background electrons are decays in which only one of the daughter tracks was reconstructed and identified. Since its partner is missing, the electron will only contribute to the combinatorial background in this case. These *incomplete* pairs can originate from any particle, but mainly stem from low invariant mass decays like photon conversions and π^0, as will be shown below. First, it makes sense to classify the tracks into the following categories, which helps to understand the various sources of incomplete decays and how to reject them (see Figure 5.36):

1. **Out-Of-Acceptance (OOA) Track:**
   - No MC Point in MVD+STS
   - Does not reach detector, not tracked by global tracking
2. **Track Fragment:**
   - At least 1, but less than 4 hits in MVD+STS

- Reaches detector, but is not tracked by global tracking

3. **Track Segment:**
   - At least 4 hits in MVD+STS, but no hits in RICH, TRD and TOF
   - Tracked by global tracking, but can not be identified as an electron
4. **Global Track:**
   - At least 4 hits in MVD+STS, hits in RICH, TRD and TOF
   - Tracked by global tracking and identifiable as an electron

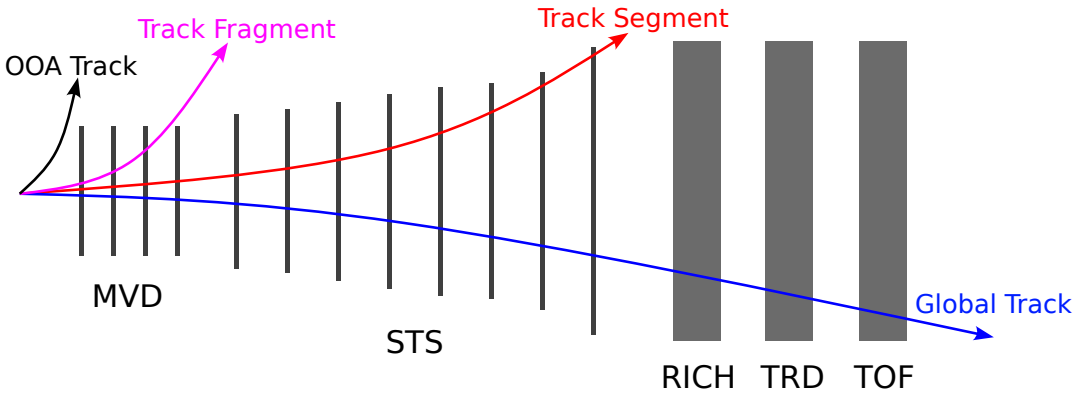

Figure 5.36.: Schematic view of different track classes depending on the amount of detectors traversed by the particles. Adapted from [70].

Since the PID cuts require hits in RICH, TRD and TOF, only global tracks remain in the final dielectron sample for the invariant mass spectrum, and hence, the only **signal** that remains is the one coming from decays in which both daughters are global tracks. All decays in which both tracks are either OOA tracks, fragments or segments are rejected. Thus, for further background reduction one needs to investigate only decays in which one daughter is a global track and the other one not, i.e. incomplete pairs. In these cases, the decay partner of this global track will be rejected by the PID cuts whereas the global track itself remains in the final sample of electron tracks and is by itself indistinguishable from signal electrons. Different strategies have to be applied depending on the track type of the decay partner track, since this changes the amount of information available: If the partner is a track segment, it can be tracked and thus, position and momentum can be accessed. However, if the partner is an OOA track or fragment, it will not appear in the array of reconstructed tracks and is lost for the analysis. It is important to note that the true partner track can only be found using the MC information, thus the partner track type is not known in the analysis.

In order to efficiently reject incomplete pairs, their frequency of occurrence and characteristics are investigated first, for which three decay modes were used, namely photon conversion, the π^0 Dalitz and the $\omega \to e^+e^-$ decay. These modes are all expected to behave differently, since γ and ω are two body decays with vastly different masses while π^0 Dalitz is a three body decay.

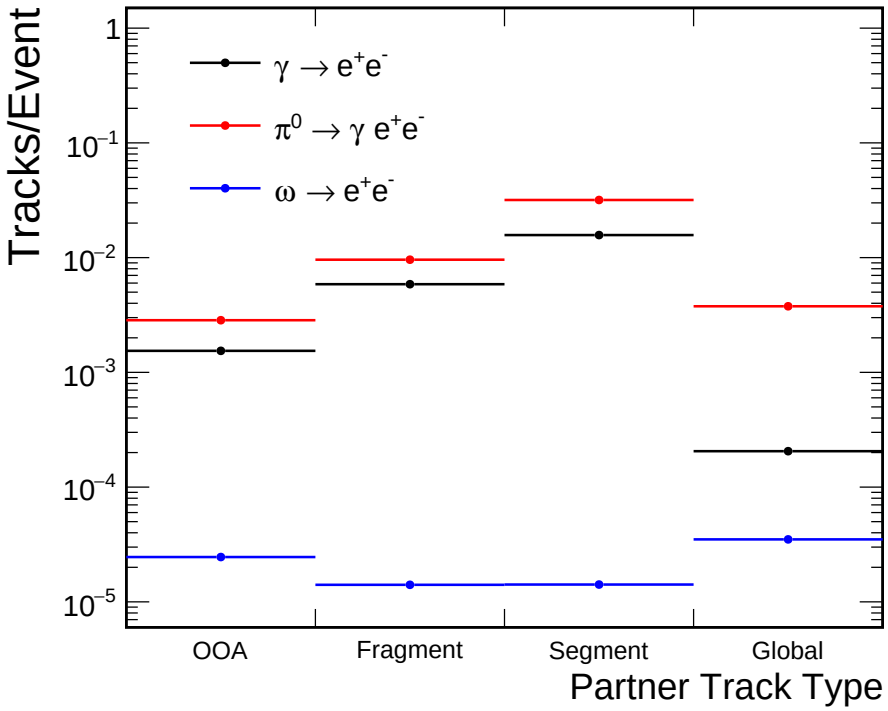

Figure 5.37.: Amount of partner track types of global tracks from different decays. For the definition of track types see the beginning of Section 5.3.2.2 and Figure 5.36. The amount of photon conversions (and π^0 to a lesser extent) with two global tracks has already been significantly decreased by the `PairPreFilter`.

For every global track of these decays which survives the PID cuts, the partner track is searched using the MC information, and subsequently classified into the different track type categories. The resulting distributions are shown in Figure 5.37. As can be seen, decays with one global track and one segment or fragment are the most abundant for photon conversions and π^0, while for the ω the partner track is most likely to be a global track as well or to be outside of the detector acceptance. One reason for this is the momentum of the decay products. The higher the momentum, the higher is the probability for the particle to reach the PID detectors, if is in detector acceptance, while

low momentum tracks are more likely do be deflected or bent out of PID acceptance by the magnetic field. This effect was visible already when investigating the acceptance effects in Section 5.2.1: When including also the PID detectors in Figure 5.4b, the ratio of tracks for low mass decays decreased significantly.
As stated above, all global tracks which do not have a global track as decay partner only contribute to the background and therefore should be removed. The abundance of these incomplete pairs especially for conversion and π^0 underlines the importance of their rejection as these decays constitute the majority of electron tracks after the PID cuts (see Figure 5.32).

5.3.2.3. Rejection of Global Tracks with Segment as Partner

As described above, many of the background tracks with segments as partners stem from low mass decays like photon conversions or π^0. This low invariant mass results in a small opening angle ϕ between the daughter tracks, due the relation [24]:

$$M_{inv} = \sqrt{m_1^2 + m_2^2 + 2E_1E_2(1 - \beta_1\beta_2\cos\phi)} \tag{5.9}$$

Approximating electrons as massless particles ($m_1 = m_2 \approx 0$ and $E_{1,2} \approx p_{1,2}$) this can be simplified to:

$$M_{inv} \approx \sqrt{2p_1p_2(1 - \cos\phi)} \tag{5.10}$$

$$\approx \sqrt{4p_1p_2\sin^2\left(\frac{\phi}{2}\right)} \tag{5.11}$$

$$\approx 2\sin\left(\frac{\phi}{2}\right)\sqrt{p_1p_2} \tag{5.12}$$

Since the tracking information is available for the segments (as well as for the global tracks), this small opening angle can be exploited for rejection: If for each global track with a segment as decay partner one is able to find this true partner segment, the global track may be rejected based on the small opening angle. Since it is not possible to exactly find the true decay partner, the strategy is to simply match each global track to the oppositely charged track segment from the same event, which has the smallest opening angle ϕ to it. To reduce the amount of random matches, this procedure has been optimized with some topological selections, as further explained in Section A.4.

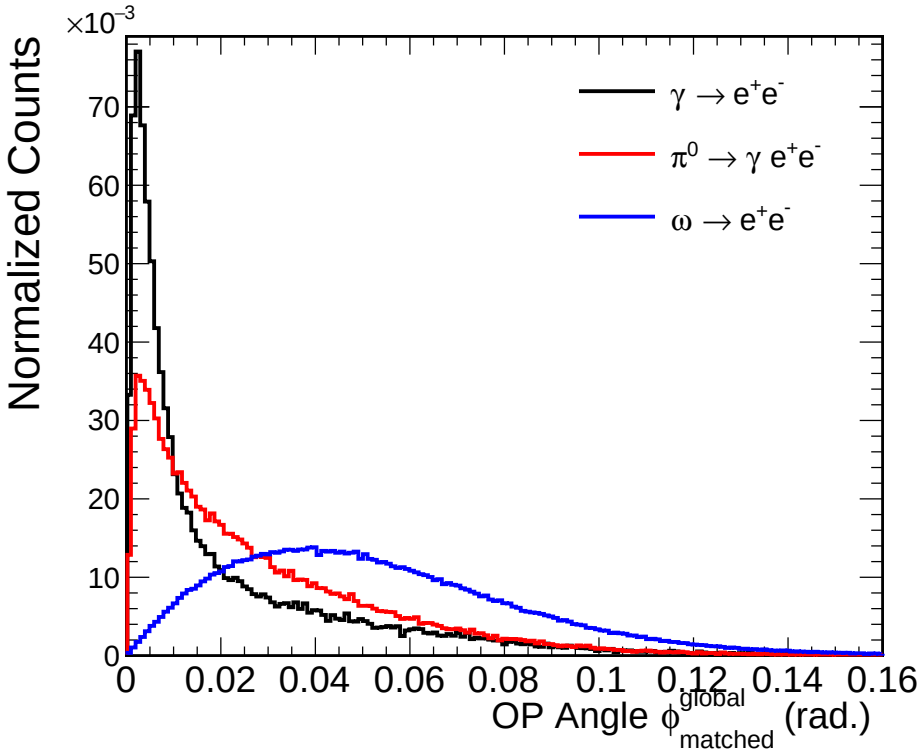

Figure 5.38.: Normalized distributions of opening angles between each global track and its respective matched track segment shown for different particle decays.

The distribution of the angle between each global track and its matched segment is shown for different decays in Figure 5.38. For low mass decays like photon conversion or π^0 the distribution exhibits a peak at very small opening angles ($\phi \lesssim 0.01\,\text{rad}$), while for $\omega \rightarrow e^+e^-$ it shows a broader distribution with the most probable value at $\phi \sim 0.04\,\text{rad}$. This is the result of the correlation between the opening angle and the invariant mass of the mother particle, as demonstrated in Equation 5.12: For low mass decays, the segment with the smallest opening angle towards the global track is often the true decay partner, whereas for high mass decays the true opening angle is of such a large size that the closest segment will be a random match, causing a broader angle distribution. Since Equation 5.12 also contains a dependence on the momenta of the daughter tracks, it makes sense to plot the opening angle against the square root of the product of the momenta of the global track and the matched segment $\sqrt{p_{\text{global}} \cdot p_{\text{matched}}}$, as shown in Figure 5.39.

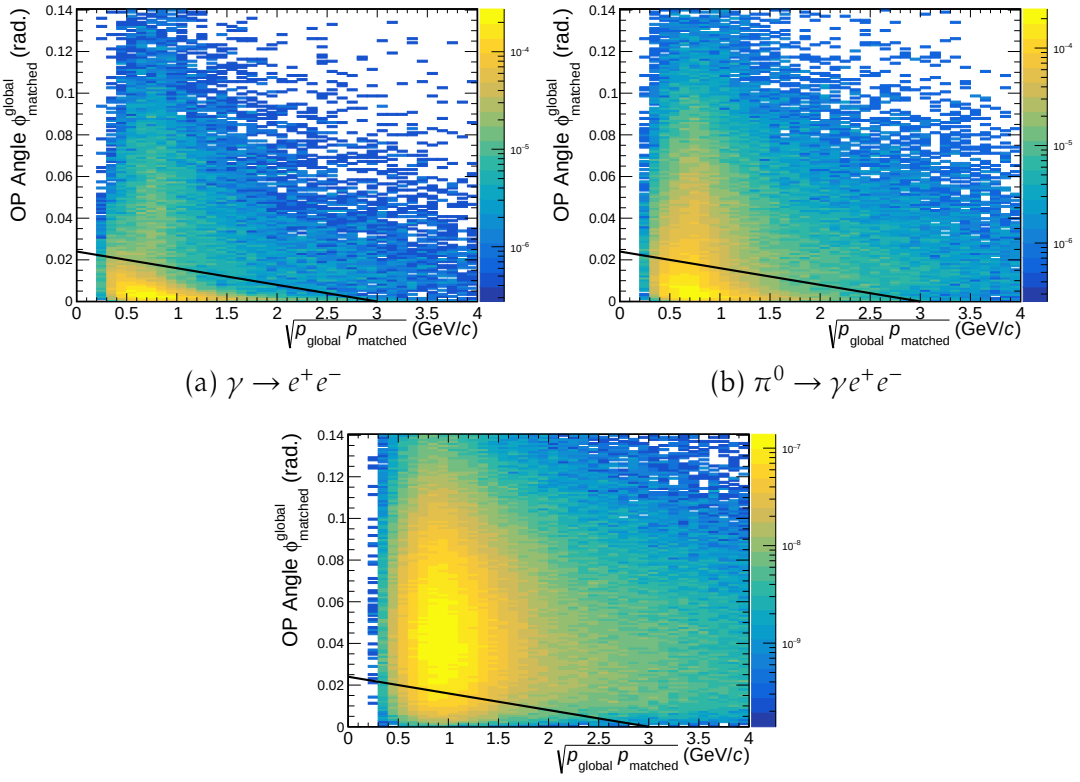

(a) $\gamma \to e^+e^-$ (b) $\pi^0 \to \gamma e^+e^-$

(c) $\omega \to e^+e^-$

Figure 5.39.: Opening angle between global track and matched track segment plotted against $\sqrt{p_{\text{global}} \cdot p_{\text{matched}}}$ for photon conversion, π^0 Dalitz and ω decay. The implemented cut is shown as a black line with entries below being rejected.

This momentum dependence is most evident in the bottom left of Figure 5.39a, since the amount of true matches is the highest for photon conversions. For these true matches, the opening angle decreases with increased combined momentum. For random matches on the other hand, momentum and opening angle are not correlated, as visible as the broad underlying distribution seen for all three decay modes. Thus, to reject as many true matches as possible while keeping a high efficiency for random matches a two-dimensional cut is implemented, as indicated by the diagonal black lines in Figure 5.39.

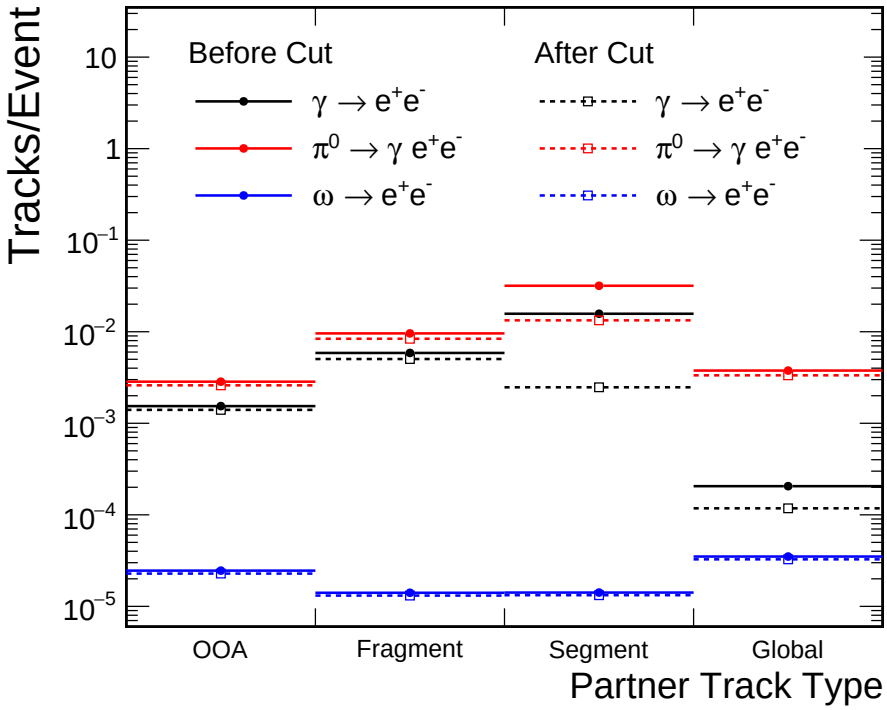

Figure 5.40.: Track types of partners of global tracks from different decays before (closed symbols) and after (open symbols) the opening angle cut. For the definition of track types see the beginning of Section 5.3.2.2 and Figure 5.36.

The distribution of track types before and after the cut is shown in Figure 5.40. As can be seen, the amount of global tracks with segments as partners originating from γ or π^0 are reduced substantially, by factors of 6.36 and 2.39, respectively, while most other tracks pass the filter with high efficiency. For tracks from $\omega \rightarrow e^+e^-$ with global tracks as partners the efficiency is 93.184 %, and 90.5 % when summing over all decays embedded with Pluto . However, for photon conversions, the cut also rejects more global tracks with global tracks as partners than for other decays. These are most likely cases, in which the partner track is classified as a global track because the MC track reaches the PID detectors, but due to non-perfect reconstruction, no PID information is attached to the track, causing it to be handled as a segment in the matching process. This may be investigated further, but since tracks from photon conversion of all track type categories contribute to the background, the additional reduction is advantageous. For completeness, the distribution of track types for all Pluto decays combined can be found in Figure A.18.

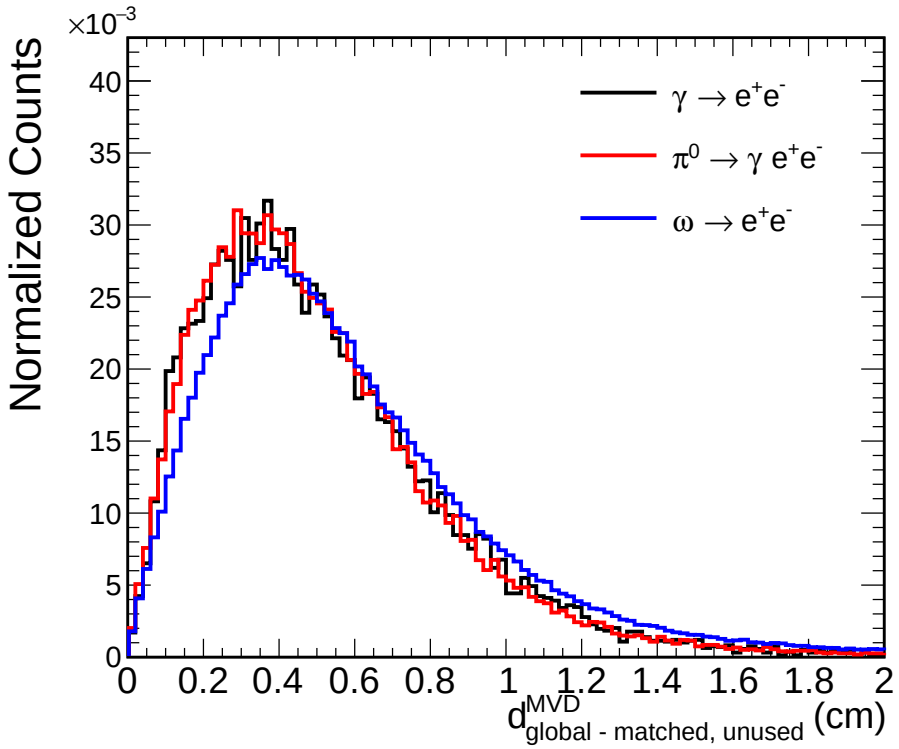

Figure 5.41.: Normalized distributions of the distance between the first `MVDHit` of the global track and the closest unused `MVDHit` in the first layer, shown for global tracks from different decays.

As for global tracks with segments as partners described in the previous section, also global tracks with fragments as partners mostly stem from low mass decays like photon conversion or π^0 Dalitz (see Figure 5.37), resulting in a small opening angle between the tracks. However, since fragments can not be reconstructed by the tracking algorithm, their momentum information is not accessible in the analysis and thus, no opening angle can be calculated. Nevertheless, the coordinates at which a fragment passes through the tracking stations should still be reconstructed locally as hits in the MVD or STS, only to then not be attached to any track. Thus, the position information of track fragments is available as single, „unused“ hits. Since the small opening angle results in the tracks hitting the first MVD station very close to each other, these decays may be rejected on the basis of this position information alone. Analogous to the matching for the opening angle cut described in the previous section, the challenge lies in finding the hit corresponding to the true decay partner fragment of the given global track. In this case, this is done by looping over all `MVDHits` in the first station, which are not attached

to any track, and selecting the one with the smallest distance to one of the global track.
The resulting distributions of the distance between the first `MVDHit` of each global track and the matched unused `MVDHit` for tracks from photon conversion, π^0 and ω are shown Figure 5.41. Evidently, there is no significant difference between the distributions and therefore no effective cut can be implemented. The similarity of the distributions is a result of the fact that they are dominated by random matches, which is caused by the large amount of unused hits in the first MVD station. This can be verified by calculating the distance between each global track and fragment in the first station with MC information, are shown in Figure 5.42.

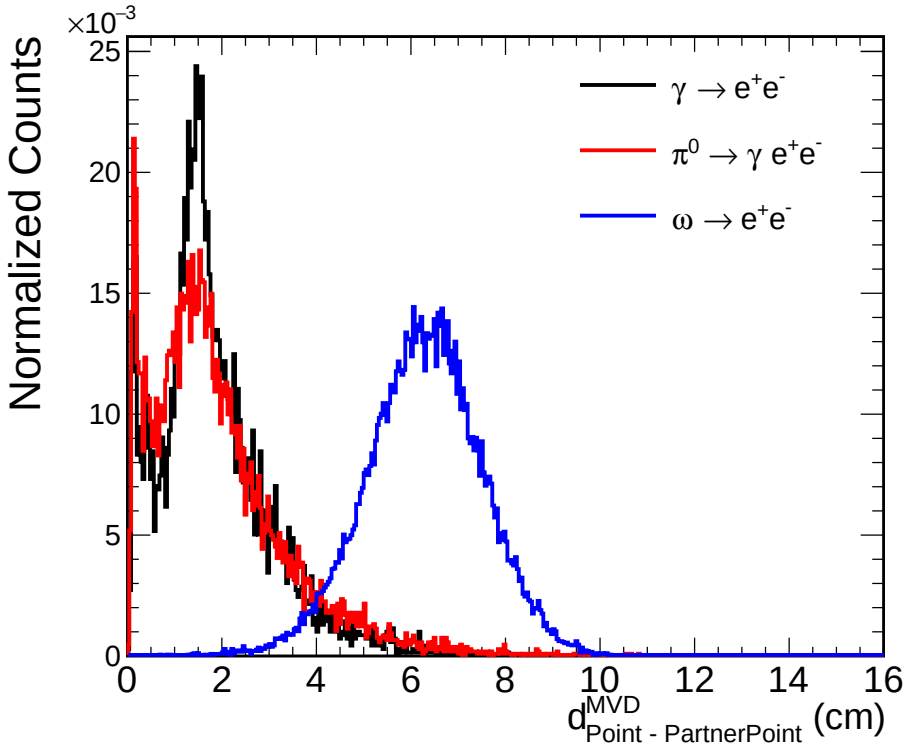

Figure 5.42.: Normalized distributions of the distance between the `MVDPoint` of the global track and its decay partner fragment in the first layer, shown for global tracks from different decays. The correct partner fragment is identified using MC information.

As can be seen from Figure 5.42, if one would be able to find the true partner fragment for each global track, it would be possible to reject the tracks from photon conversion and π^0 Dalitz decays with a cut on the distance between their `MVDHits`. While not viable for this analysis, this approach might be used in the future, for example in case the tracking of low momentum tracks

is improved, reducing the amount of unused hits in the first MVD layer.

5.4. Invariant Mass Spectra

The aim of this analysis is to reconstruct the invariant mass spectrum of the dielectron decays described in Section 5.2 with the highest possible signal-to-background ratio, in order to be able to extract fireball parameters like temperature or lifetime from the excess radiation (see Section 2.3).

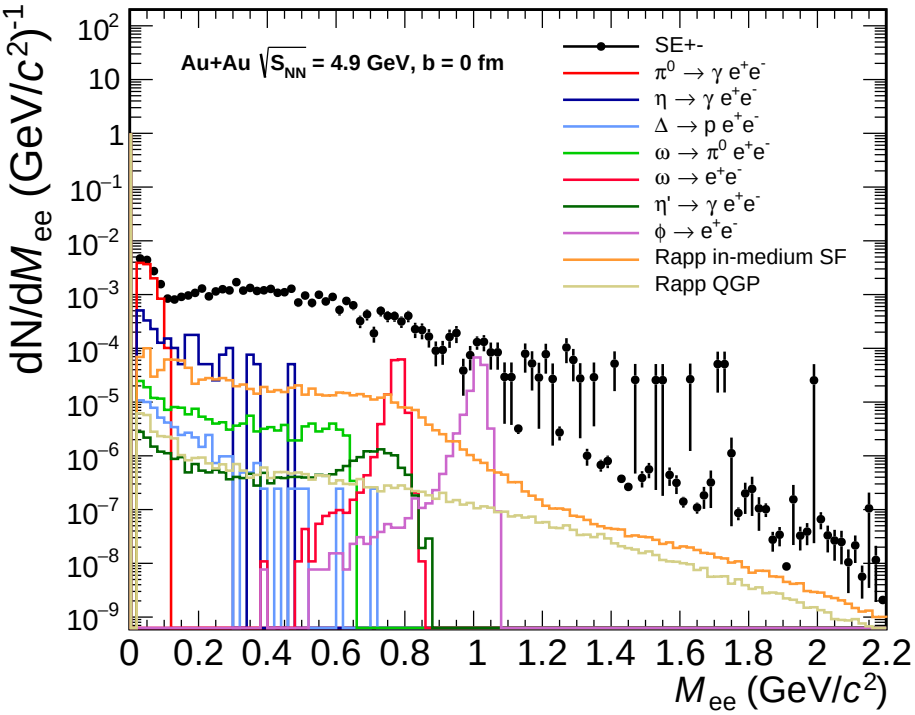

Figure 5.43.: Invariant mass spectrum of all remaining unlike signed pairs from the same event (SE+-) after applying the background rejection methods described in Section 5.3. The information from PID detectors is utilized via conventional cuts, all cuts are summarized in Table A.5. The simulated data contains 2 million Au+Au collisions at $\sqrt{s} = 4.9\,\text{GeV}$ and $b = 0\,\text{fm}$. The yields are normalized by the number of events.

This spectrum can be seen in Figure 5.43, showing the invariant mass of all pairs of oppositely charged tracks from the same event remaining in the final sample, denoted by „SE+-“[10] (black circles). By using MC information,

[10] Same Event +-

the contributions from the different mother particles are identified and plotted in color. With these the different regions of the spectrum can be identified: Below $M_{\mathrm{inv}} \sim 0.1\,\mathrm{GeV/c^2}$ it is dominated by the π^0 Dalitz decay, while for $0.1\,\mathrm{GeV/c^2} \lesssim M_{\mathrm{inv}} \lesssim 0.6\,\mathrm{GeV/c^2}$ the $\eta \to \gamma e^+e^-$ forms the highest contribution. However, in this region also decays from the in-medium modified spectral function of ρ and ω are signifcant, enhancing the yield which would be expected from dielectron decays without any medium effects. Therefore, by measuring the excess yield in this *enhancement* region, the lifetime of the fireball can be calculated (see Section 2.3.2). The enhancement region ends at $M_{\mathrm{inv}} \sim 0.6\,\mathrm{GeV/c^2}$ when the peak from $\omega \to e^+e^-$ starts to become significant, followed by one from $\phi \to e^+e^-$. For higher masses ($M_{\mathrm{inv}} \gtrsim 1.1\,\mathrm{GeV/c^2}$) only thermal contributions are relevant, possibly giving access to the fireball temperature. However, the data shown in Figure 5.43 exhibits a high variance

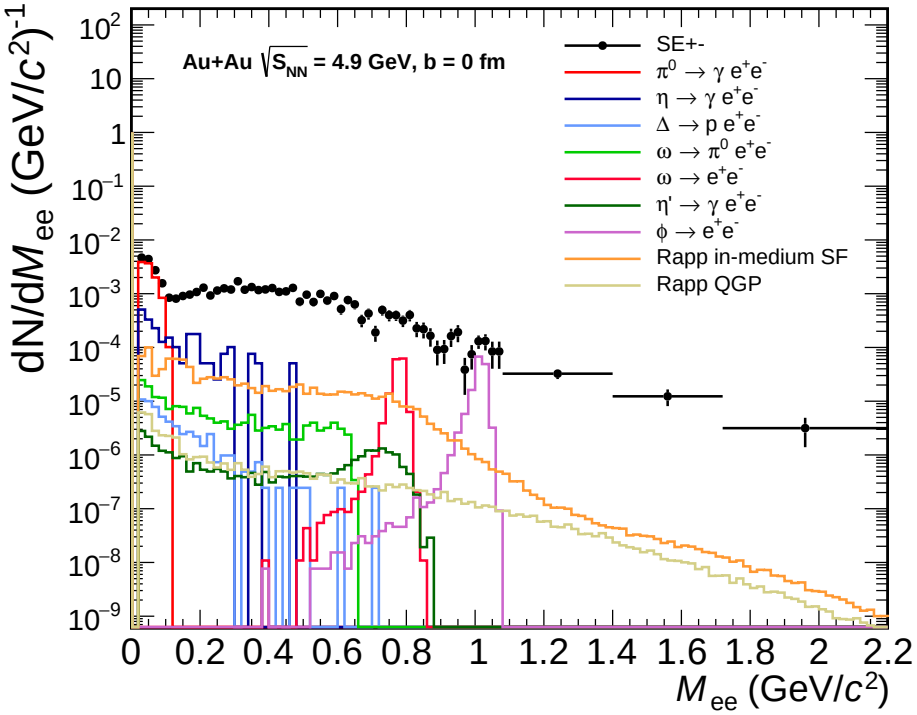

Figure 5.44.: Invariant mass spectrum of all remaining unlike signed pairs from the same event (SE+-) after applying the background rejection methods described in Section 5.3, as shown already in Figure 5.43. For $M_{\mathrm{inv}} \geq 1.08\,\mathrm{GeV/c^2}$, the histogram is rebinned to accurately reflect the distribution.

of the entries in this mass range, which is caused by low statistics in combination with the different weighting of the pairs depending on their mother particles. Due to the low amount of tracks, many bins are filled only with

pairs of Pluto tracks, which can be seen as the entries at very low yields and small statistical errors on the right side of Figure 5.43. Since these bins vastly underestimate the background, a wide rebin is needed to display a more accurate distribution, as shown in Figure 5.44.

Fortunately, the amount of remaining signal in this mass range is still well known, since only the thermal contributions are relevant, which are embedded with enhanced statistics. Thus, by approximating the background with the *random event technique* (see Section A.5) and using MC information to identify signal pairs, it is possible to extract a Signal-to-Background (S/B) ratio with finer bins, which can be seen in Figure 5.45. In the enhancement

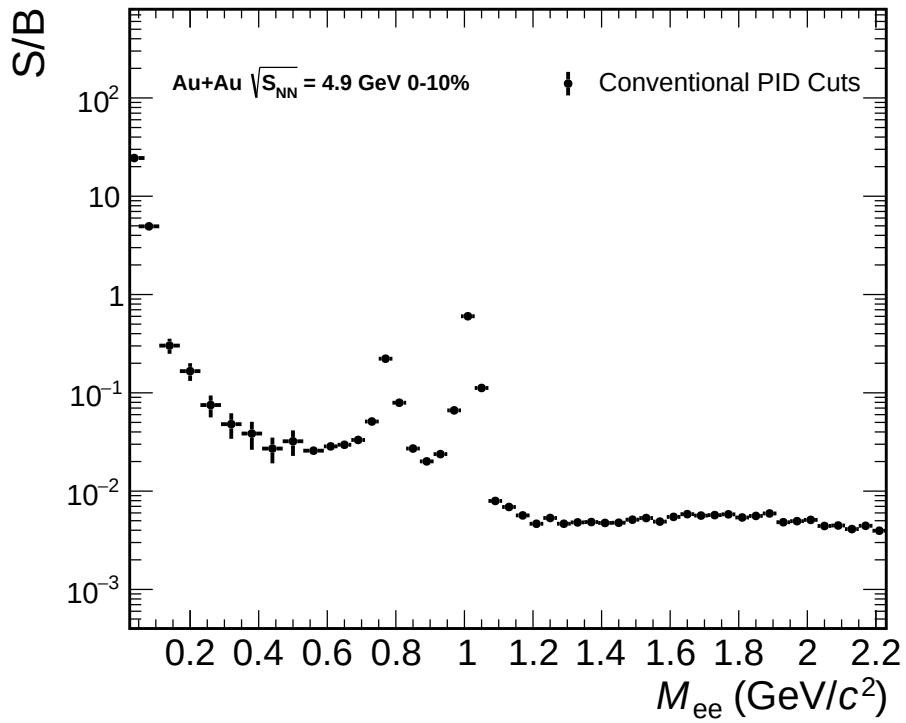

Figure 5.45.: Signal-to-Background (S/B) ratio calculated as the sum of all dilepton signals shown in Figure 5.44 identified with MC information divided by the combinatorial background approximated with 10^{10} *random events* (see Section A.5) .

region wider bins are used, due to the low statistics of the η Dalitz which is the dominant decay for this mass range. This is a result of the fact that it is taken directly from the UrQMD events and not embedded with Pluto, resulting in a higher statistical uncertainty. The S/B ratio itself is rather high considering the rarity of the signals, reaching 0.2 and 0.6 for the ω and ϕ peaks, respectively, and $\sim$ 1/200 in the IMR. The cut on the opening angle

of matched global tracks and track segments described in Section 5.3.2.3 is already included here. Its impact on the S/B ratio is shown in Figure A.19.

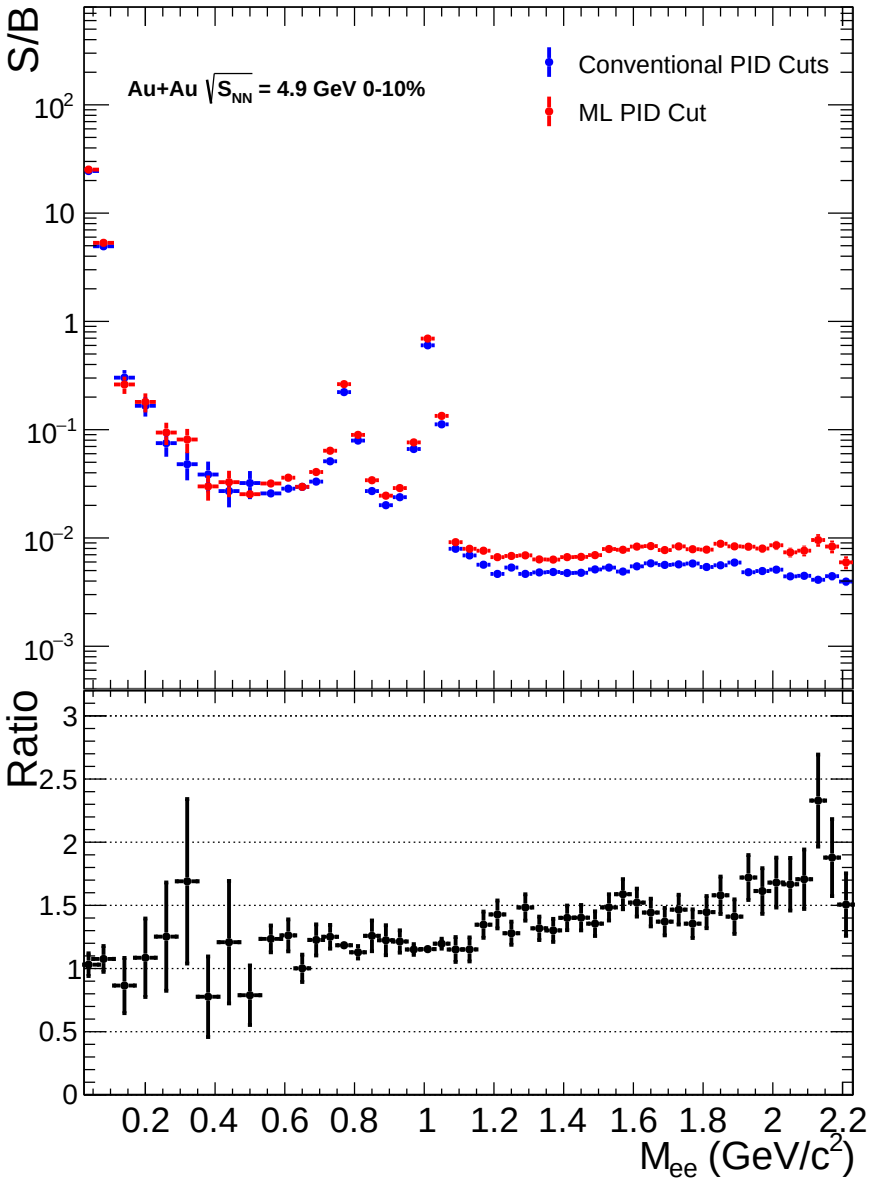

Figure 5.46.: Comparison between Signal-to-Background (S/B) ratio achieved with conventional PID cuts and with the ML classifier described in Section 5.3.1.2, calculated as the sum of all dilepton signals shown in Figure 5.44 identified with MC information divided by the combinatorial background approximated with 10^{10} *random events* (see Section A.5). The lower panel shows the ratio of $\frac{S/B_{\mathrm{ML}}}{S/B_{\mathrm{Conv.}}}$.

By using the ML classifier for PID (see Section 5.3.1.2) instead of conventional box cuts the S/B ratio can be improved even further, as shown in Figure 5.46. Except for the enhancement region, where more statistics are needed for a meaningful comparison, using the ML classifier results in a higher S/B ratio, with the improvement ranging between a factor of 1 and 2, generally increasing with the mass of the dielectron pair. Thus, S/B ratios between 1/160 and 1/100 are reached in the IMR, meaning that about 20000 to 32000 signal pairs are needed for a statistical accuracy of 10 % for the thermal signal yield. After the first year of running, CBM will gradually increase the interaction rate from 100 KHz to 1 MHz, which will allow to record the required statistics in 10 days of running. This will be further improved by optimizing efficiency for electron reconstruction and identification, as has recently been shown in Ref. [71].

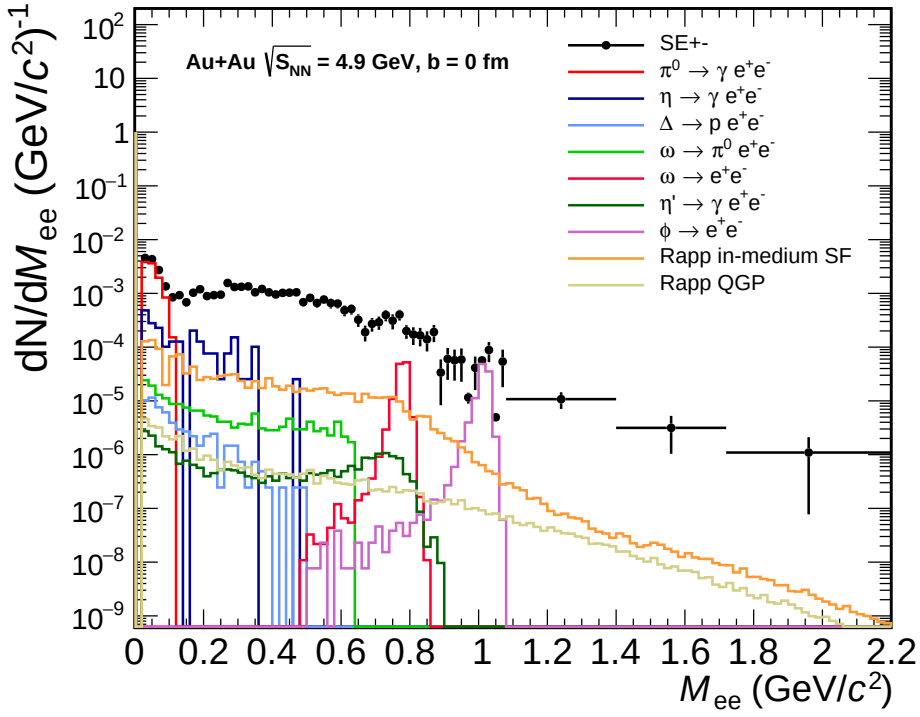

Figure 5.47.: Invariant mass spectrum of all remaining unlike signed pairs from the same event (SE+-) after applying the background rejection methods described in Section 5.3, with the information from PID detectors used as inputs for a ML classifier (see Section 5.3.1.2). All cuts are summarized in Table A.6. For $M_{\text{inv}} \geq 1.08\,\text{GeV/c}^2$, the histogram is rebinned to accurately reflect the distribution.

6. Summary

Starting in 2028, the Compressed Baryonic Matter (CBM) experiment will explore uncharted territory in the high μ_B region of the Quantum Chromodynamics (QCD) phase diagram, as it is uniquely suited to measure rare probes due to its high interaction rates. One of these rare probes is the thermal radiation of the fireball created in the collision, which is emitted in the form of virtual photons and can be accessed by their decays into lepton pairs. This radiation is of particular interest, as it is radiated throughout the whole evolution of the medium and does not partake in the strong interaction. Thus it carries information about the earlier stages of the fireball and is able to leave the medium undisturbed. It can therefore be used to extract, among others, the temperature of the fireball before hadronization, rendering it an ideal tool in the search for latent heat effects, which would indicate a first-order phase transition between the Quark-Gluon Plasma (QGP) and hot and dense hadronic matter at high μ_B and thus the existence of a critical point.
Both dilepton decay channels $\gamma^* \rightarrow e^+e^-$ and $\mu^+\mu^-$ will be measured with CBM, serving as a valuable crosscheck for systematic uncertainties. This work is focused on the analysis of the dielectron channel and its associated challenges, one of which is the large amount of hadronic background in form of pions, protons and kaons. As the yield of these particles is three to four orders of magnitude higher than the one of dielectrons from thermal radiation, exceptional Particle Identification (PID) capabilities are crucial in order to sufficiently reduce the hadronic contributions to gain access to the signal. For this reason, the CBM electron setup features two dedicated detectors for electron identification, namely the Ring Imaging Cherenkov (RICH) detector and the Transition Radiation Detector (TRD). The latter is developed and constructed by groups of the Institut für Kernphysik Münster (IKP), the Institut für Kernphysik Frankfurt (IKF) and Horia Hulubei National Institute of Physics and Nuclear Engineering (IFIN-HH) in Bucharest, Romania.
The electron identification capability of the TRD depends heavily on the amount of Transition Radiation (TR) generated by electrons passing through its radiator. Therefore, the groups from IKP and IKF conducted a testbeam campaign at Deutsches Elektronen-SYnchrotron (DESY) in 2019 with the aim to characterize the radiator performance with respect to its width. In this work, the data from this campaign is analyzed with regard to the reconstruction of energy loss spectra produced by electrons passing through the detector. Various methods to reduce the amount of undesired noise in the data are

implemented at different points of the reconstruction process, ranging from a filter based on the shape of the analog signal to cuts on the calculated position of the measured energy loss. When comparing the resulting spectrum for electrons at a momentum of $p = 3\,\mathrm{GeV/c}$ to the one measured in parallel for an ^{55}Fe source emitting photons with $E_\gamma = 5.96\,\mathrm{keV}$, the data does not match the expected distributions. The individual spectra exhibit the expected shapes, i.e. a Gaussian for the ^{55}Fe source and a Landau-Gaussian for the electrons. However, the positions of their Most Probable Values (MPVs) are observed to be shifted relative to each other. An extensive analysis of this finding is carried out in this thesis, making use of the data recorded with the ^{55}Fe source at various different operating voltages of the TRD's wire chamber, as well as the detailed simulation framework for the TRD detector response included in `cbmroot`. Ultimately, the bias in the spectra is attributed to the set trigger thresholds of the readout electronics, rejecting 70 to 80 % of the signals, predominantly at the lower end of the energy spectrum. As this bias renders an energy calibration impossible, no quantitative comparison between the performance of the different radiators can be carried out. Nonetheless, from the qualitative assessment of the data it is still possible to infer a rise in TR generation with increasing radiator width which does not saturate below 31.5 cm. Thus, this radiator width should be favored when optimizing solely for PID performance.

In the second part of this thesis, a dielectron pair analysis for the CBM experiment is carried out, based on simulated data at the highest collision energies foreseen for CBM, with $\sqrt{s} = 4.9\,\mathrm{GeV}$. The aim is to optimize methods for background rejection to improve the signal-to-background ratio, in particular in the Intermediate Mass Region (IMR) of the invariant mass spectrum, in order to access the thermal signal and extract the temperature of the medium with sufficient accuracy. For this, conventional cut-based hadron rejection is studied, using not only the two dedicated detectors for electron identification (RICH and TRD) but also utilizing information from the Time-Of-Flight System (TOF) and Silicon Tracking System (STS), resulting in a further improvement of the hadron rejection, especially at low momenta.

Based on the results of a master thesis (see Ref. [65]), a classification algorithm for electrons and hadrons using the Machine Learning (ML) library `XGBoost` is trained and implemented into `cbmroot` as an alternative to the conventional hadron rejection method. In a comparison based on the same data set and tuned to the same efficiency for signal electrons, the ML classifier achieves an increase in rejection factors for pions, protons and kaons of 2.3, 1.7 and 1.4, respectively. For the Signal-to-Background (S/B) ratio, this results in an increase of a factor of ~ 1.5 in the IMR.

Furthermore, the reduction of electron background is assessed. At first, the „standard" methods to reject electrons from photon conversions such as using the track fit to the collision vertex and the invariant mass of pair candidates are applied. Subsequently it is found, that the largest remaining

background contribution stems from *incomplete pairs*. In these cases, only one electron/positron reaches the PID detectors („global track“), while its decay partner track leaves the setup before being identified, resulting in one single electron/positron track remaining in the sample. An investigation of the topology of these incomplete pairs shows, that in most cases the particle not reaching the PID detectors is still tracked in the tracking stations („track segment“), giving access to its momentum information. By matching these segments to global tracks and implementing a rejection based on the resulting opening angle, the contribution to the electron background by this class of incomplete decays is reduced by a factor of 2.9, resulting in an increase of the S/B ratio of a factor between two and three over the entire mass range.
Using all newly implemented methods for background reduction, a S/B close to 1/100 in the IMR is reached, which is the target value for a statistically significant thermal signal with the expected number of events collected in a few years of CBM running. Thus, this work makes an important contribution to ensure that a successful measurement of the thermal dielectron continuum will be possible.

7. Zusammenfassung

Das Compressed Baryonic Matter (CBM) Experiment wird 2028 in Betrieb genommen und unerforschte Bereiche des Quantum Chromodynamics (QCD) Phasendiagramms erkunden, da es mithilfe seiner hohen Interaktionsraten in der Lage sein wird, seltene Signale mit bisher unerreichter Genauigkeit zu vermessen. Eine dieser seltenen Sonden ist die thermische Strahlung des in der Teilchenkollision entstehenden Feuerballs, welche in Form von virtuellen Photonen emittiert wird und über ihren Zerfall in Leptonenpaare detektiert werden kann. Diese Strahlung ist von besonderem Interesse, da sie zum einen über die gesamte Lebensdauer des Feuerballs abgestrahlt wird, und zum anderen nicht der starken Wechselwirkung unterliegt. Entsprechend trägt sie Informationen über die frühe Phase des Feuerballs und ist zusätzlich in der Lage das Medium störungsfrei zu verlassen. Deshalb kann sie unter anderem dazu genutzt werden, die Temperatur des Feuerballs vor der Hadronisierung zu extrahieren, was sie zu einem idealen Werkzeug für die Suche nach latenter Wärme macht, welche ein Hinweis für einen Phasenübergang erster Ordnung zwischen dem Quark-Gluon Plasma (QGP) und heißer und dichter hadronischer Materie und somit für die Existenz eines kritischen Punktes wäre.

CBM wird beide Zerfallskanäle in Dileptonen, sowohl $\gamma^* \rightarrow e^+e^-$ als auch $\mu^+\mu^-$, vermessen, da dies sehr hilfreich für die Bestimmung der systematischen Unsicherheiten ist. Der Fokus dieser Arbeit liegt in der Analyse des Dielektronenzerfallskanals und den damit verbundenen Herausforderungen. Eine davon ist der große Betrag des hadronischen Untergrunds in Form von Pionen, Protonen und Kaonen. Da die Häufigkeit dieser Teilchen um drei bis vier Größenordnungen über der von thermischen Dielektronen liegt, werden außerordentlich gute Particle Identification (PID) Methoden benötigt, um den hadronischen Anteil in ausreichendem Maße für die Extraktion des Signals zu reduzieren. Aus diesem Grund enthält der für die Dielektronenmessungen vorgesehene CBM Detektoraufbau mit dem Ring Imaging Cherenkov (RICH) Detektor und dem Transition Radiation Detector (TRD) zwei Subsysteme, deren primäre Aufgabe es ist, Elektronen zu identifizieren. Letzterer wird von Gruppen im Institut für Kernphysik Münster (IKP), im Institut für Kernphysik Frankfurt (IKF) und im Horia Hulubei National Institute of Physics and Nuclear Engineering (IFIN-HH) in Bucharest, Rumänien, entwickelt und gebaut.

Die Effektivität des TRD für die Teilchenidentifikation hängt stark von der Menge an Übergangsstrahlung (TR) ab, welche von Elektronen generiert wird, die durch den Radiator des TRD fliegen. Daher wurden von den Gruppen des IKP und IKF 2019 eine Reihe von Testmessungen am Deutsches Elektronen-SYnchrotron (DESY) durchgeführt, mit dem Ziel, die Leistungsfähigkeit des Radiators in Abhängigkeit von seiner Dicke zu charakterisieren. In dieser Arbeit werden die Daten jener Strahlzeit im Hinblick auf die Rekonstruktion der Energieverlustspektren von Elektronen im Detektor analysiert. Verschiedene Methoden zur Reduktion von Störsignalen werden an unterschiedlichen Stelle der Rekonstruktion implementiert, von einem Filter basierend auf der Form der analogen Signalkurve, bis hin zu Schnitten anhand der berechneten Position des gemessenen Energieeintrags. Beim Vergleich des resultierenden Spektrums für Elektronen mit einem Impuls von $p = 3\,\mathrm{GeV/c}$ mit dem einer ^{55}Fe Quelle, welche Photonen mit $E_\gamma = 5.96\,\mathrm{keV}$ emittiert und parallel gemessen wurde, wird festgestellt, dass die Spektren nicht den erwarteten Verteilungen entsprechen. Zwar haben die Spektren für sich betrachtet die erwartete Form (eine Gaußverteilung für die ^{55}Fe Quelle und eine Landau-Gaußverteilung für die Elektronen), jedoch sind die Most Probable Values (MPVs) der Verteilungen relativ zueinander verschoben. Daher wird eine ausführliche Analyse bezüglich dieses Befundes durchgeführt, einerseits mithilfe von Daten, welche am DESY mit der ^{55}Fe Quelle bei anderen Betriebsspannungen aufgenommen wurden, andererseits mithilfe der detaillierten Detektorsimulation, die in `cbmroot` integriert ist. Schlussendlich wird die Verschiebung der Spektren auf die Schwellwerte zurückgeführt, welche in der Ausleseelektronik im Rahmen der Messung gesetzt wurden, da diese 70 bis 80 % der zu messenden Signale zurückweisen, vor allem solche, die sich am unteren Ende des Energiespektrums befinden. Da aufgrund dieser Verschiebung eine Energiekalibration nicht möglich ist, kann kein quantitativer Vergleich der Leistungsfähigkeit der verschiedenen Radiatoren durchgeführt werden. Jedoch kann auch von der qualitativen Begutachtung der aufgenommenen Spektren abgeleitet werden, dass die Menge der generierten TR mit steigender Radiatordicke zunimmt und bis hin zu einer Dicke von $w = 31.5\,\mathrm{cm}$ nicht in eine Sättigung läuft. Wird der Detektor also einzig auf die Fähigkeit zur Elektronenidentifikation optimiert, ist ein solcher Radiator zu bevorzugen.

Im zweiten Teil dieser Arbeit wird eine Dielektronenpaaranalyse für das CBM Experiment basierend auf simulierten Daten für Kollisionen bei den höchsten vorgesehenen Energien mit $\sqrt{s} = 4.9\,\mathrm{GeV}$ durchgeführt. Das Ziel dabei ist, die Methoden für die Reduktion des Untergrunds zu optimieren, um ein besseres Signal-to-Background (S/B) Verhältnis zu erzielen. Dies ist besonders wichtig in der Intermediate Mass Region (IMR) des invarianten Massenspektrums, um dort die Signale thermischer Strahlung und somit die Temperatur des Systems mit ausreichender Genauigkeit extrahieren zu können. Dazu wird zunächst die konventionelle Methode zum Aussortieren von Ha-

dronen untersucht, welche mithilfe von einzelnen Schnitten basierend auf den Daten der Subdetektoren vorgenommen wird. Hierbei werden in dieser Arbeit nicht nur die Signale von den beiden für die Elektronenidentifikation dedizierten Detektoren (RICH und TRD) verwendet, sondern zusätzlich auch die des Time-Of-Flight System (TOF) und des Silicon Tracking System (STS). Dadurch wird eine weitere Verbesserung der Hadronenreduktion erzielt, welche besonders bei niedrigen Impulsen ausgeprägt ist.
Auf Basis der Ergebnisse einer Masterarbeit (siehe Quelle [65]) wird ein Algorithmus für die Klassifizierung von Elektronen und Hadronen mithilfe der Machine Learning (ML) Bibliothek `XGBoost` trainiert und in `cbmroot` implementiert, um eine Alternative zur herkömmlichen Methode der Teilchenidentifikation zu bieten. In einem Vergleich, bei dem derselbe Datensatz verwendet und beide Methoden auf dieselbe Effizienz für Signalelektronen eingestellt wird, erzielt der ML Klassifizierungsalgorithmus höhere Hadronenreduktionsfaktoren. Speziell konnte dieser für Pionen um einen Faktor von 2.3 erhöht werden, für Protonen um 1.7 und für Kaonen um 1.4, was zu einer Verbesserung des S/B Verhältnisses in der IMR um einen Faktor ~ 1.5 führt.
Weiterhin wird auch die Reduktion des Elektronenuntergrunds untersucht. Zunächst werden die „üblichen“ Methoden zum Aussortieren von Konversionselektronen basierend auf der Qualität der Spuranpassung zum Kollisionsvertex sowie der invarianten Masse von Paarkandidaten angewandt. Anschließend wird festgestellt, dass der größte verbleibende Anteil des Untergrund von *unvollständigen Paaren* herrührt. Dies sind Fälle, in denen nur ein Elektron/Positron die PID Detektoren erreicht („Globale Teilchenspur“), während sein Zerfallspartner den Detektor verlässt, bevor er identifiziert werden kann, was darin resultiert, dass eine einzelne Elektronen- bzw. Positronenspur verbleibt. Eine Untersuchung der Topologie dieser unvollständigen Paare zeigt, dass die Teilchenspur, welche die PID Detektoren nicht erreicht, in den meisten Fällen aber dennoch vom Trackingsystem erfasst wird („Teilchenspursegment“) und daher die Information über ihren Impuls vorhanden ist. Diese Segmente werden mit globalen Teilchenspuren zu Paaren zusammengefügt und ein Ausschlusskriterium basierend auf dem resultierenden Öffnungswinkel implementiert. Dadurch wird der Beitrag dieser Klasse von unvollständigen Paaren um einen Faktor von 2.9 reduziert, und somit das S/B Verhältnis im gesamten invarianten Massenbereich verdoppelt bis verdreifacht.
Mittels dieser neu implementierten Methoden zur Reduzierung des Untergrunds wird ein S/B Verhältnis von nahezu 1/100 in der IMR erreicht, was der Zielvorgabe für ein statistisch signifikantes thermisches Signal mit der Anzahl an Kollisionen entspricht, die in wenigen Jahren Laufzeit von CBM erwartet werden. Daher leistet diese Arbeit einen wichtigen Beitrag daran, eine erfolgreiche Messung des Dielektronkontinuums mit CBM sicherzustellen.

A. Appendix

A.1. Detector Simulation Tuning

The simulation framework for the detector response of the CBM-TRD is a highly customizable tool, which simulates the response in great detail starting from individual energy deposits in the gas volume (`TrdPoints`) supplied by `Geant3`, generating signal pulses using the SPADIC's shaper response function (Equation 4.1), checking a trigger condition and producing digis. Detailed descriptions can be found in Refs. [55] and [56]. Several parameters have to be adjusted in order to properly reflect the conditions at the measurements at DESY.

A.1.1. ADC Noise Level

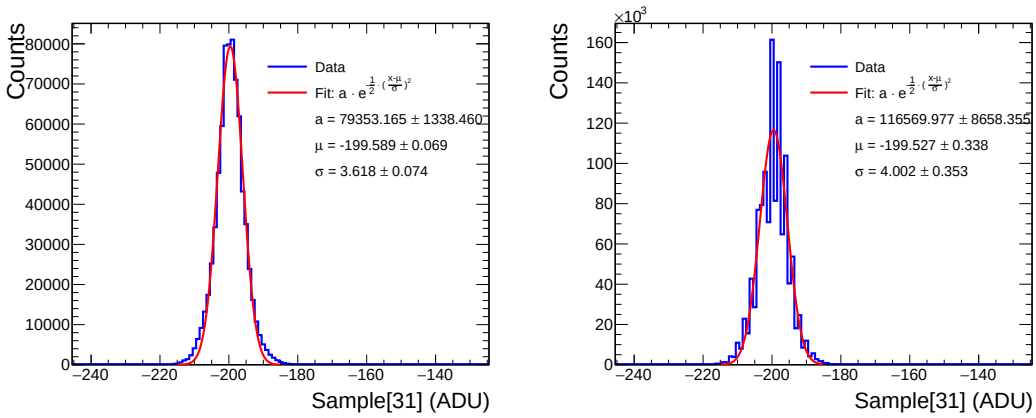

(a) SPADIC 0 Channel 16 (b) SPADIC 0 Channel 18

Figure A.1.: Last sample of all FNR signals on the two most active channels in the beam spot each fitted with a Gaussian function.

For the generated pulses, stochastic noise can be added on each ADC sample, based on a Gaussian distribution. The settable parameter in the software is called `fAdcNoise` and defines the width σ of the Gaussian in ADU. To quantify the noise level in the measurement, the distributions of the last of the 32 samples of (`sample[31]`) signals measured on the two most active channels

in the beam spot are examined. The last sample is chosen to reduce bias due to the tail of the signal. To further reduce this effect, only FNR messages are used, which in general have smaller signal amplitudes. The measured distributions are shown in Figure A.1 together with their respective Gaussian fit functions. While the fit describes the data from channel 16 very well, channel 18 shows a high fluctuation between entries in neighboring bins. This is caused by a bug in the ADC slightly favoring certain bit configurations on some channels in this specific SPADIC version (SPADIC 2.2). The cause for this is suspected to be a weakness in the interface between the ADC and the digital part of the chip [72].

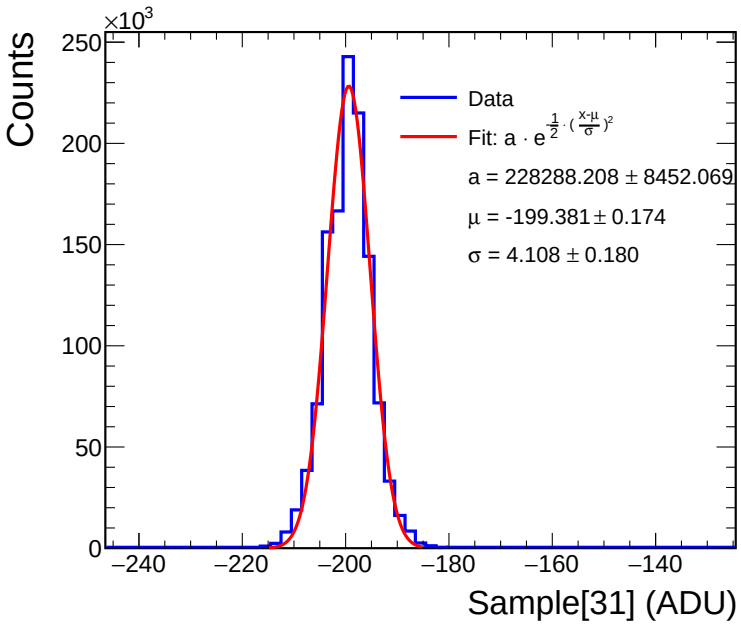

Figure A.2.: Last sample of all FNR signals on SPADIC 0 channel 18 fitted with a Gaussian function after a rebin by the factor of 2.

Therefore, the data is rebinned by a factor of two and fitted again, as shown in Figure A.2, thus resulting in values for the width of the distributions $\sigma_{\mathrm{ch16}} = 3.618 \pm 0.074\,\mathrm{ADU}$ and $\sigma_{\mathrm{ch18}} = 4.108 \pm 0.180\,\mathrm{ADU}$ for channel 16 and channel 18, respectively. As the parameter `fAdcNoise` in the simulation software is of type `integer` it is set to 5 ADU to not underestimate the width.

A.1.2. Clipping level

Even though the upper limit of the digital part of the SPADIC is 255 ADU, clipping on the analog part may occur already at lower values depending on the baseline level on each individual channel.

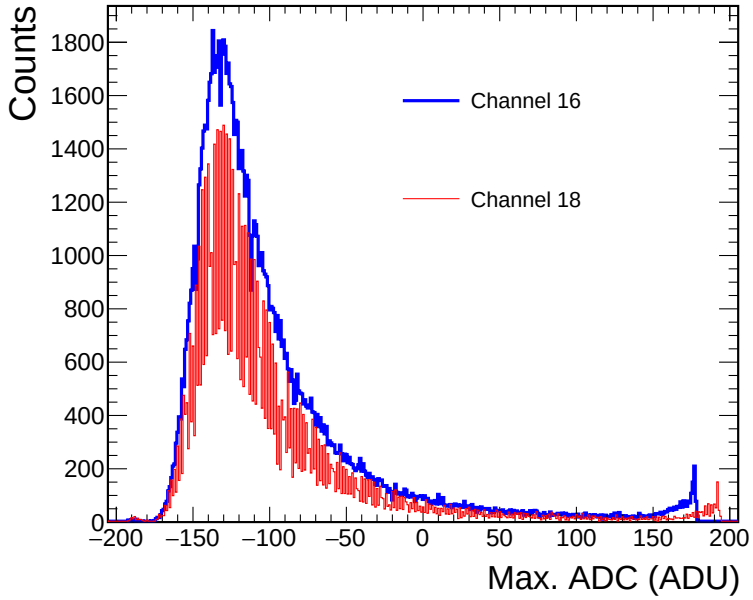

Figure A.3.: Maximum ADC value of STR signals recorded on the two most active channels in the beam spot. Only signals fulfilling the condition described in Equation 4.3 are shown.

Figure A.3 shows the maximum ADC spectra of STR signals on the most active channels in the beams spot. Evidently both channels exhibit clipping at values below 255 ADU, with 179 ADU being the highest value registered on channel 16 and 194 ADU on channel 18. However, the corresponding parameter in the simulation software `fClipLevel` is a global parameter applied to all channels and thus the lower value is chosen. To account for the baseline lying at −200 ADU the parameter is set to `fClipLevel`= 379 ADU.

A.1.3. Signal peaking time

The shaping function of the SPADIC described by Equation 4.1 with a peaking time of $\tau = 110\,\text{ns}$ is the response of the CSA to an incoming charge in form of a delta peak. In reality the charge is collected over a finite time, prolonging the pulse and shifting the position of the maximum to a later time, as the true signal will be a convolution of the chamber response and the shaping function. In the simulation framework this is simplified by generating one signal in the form of Equation 4.1 with $\tau = 110\,\text{ns}$ for each primary ionization and calculating the sum considering their respective drift times [55]. However, as this seems to not accurately describe the real measurement, as longer peaking times were observed in the measurement, which are shown

as the position of the sample containing the maximum of the signal in Figure A.4.

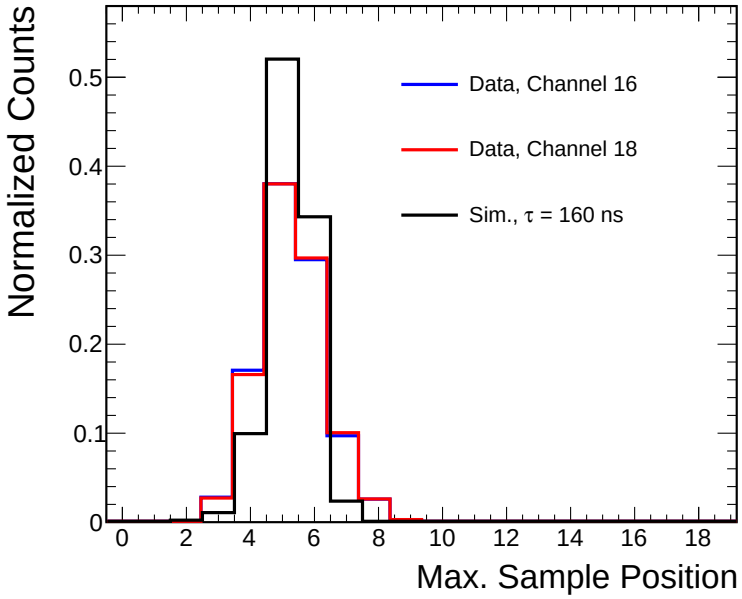

Figure A.4.: Position of the sample containing the highest ADC value of the signal on the two most active channels in the beam spot (blue and red lines) and in simulation (black line). In addition to the set trigger condition of the SPADIC and the signal shape filter described in Equation 4.3 only signals with amplitudes > 75 ADU above baseline were considered to reduce effects caused by noise.

Thus, the corresponding parameter in the simulation framework `fTau` is increased to 160 ns, at which the mean peaking times $\langle\tau\rangle$ of data and simulation are in sufficient agreement. In this case the average peak position is at sample $\langle N_{\text{max. sample}}\rangle = 5.261$ on channel 16 and $\langle N_{\text{max. sample}}\rangle = 5.279$ on channel 18, while for simulation it is at $\langle N_{\text{max. sample}}\rangle = 5.263$.

A.1.4. Gain factor

To properly adjust the gain factor controlling the amplitude two observables are considered: The charge registered on the central pad of 3-pad clusters in the beam spot, as well as the distribution of cluster sizes, which can be seen Figure A.5.

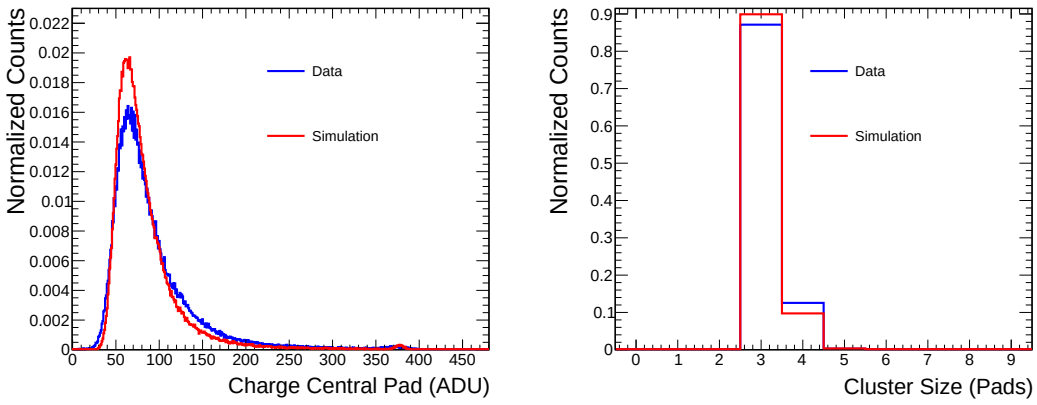

Figure A.5.: Comparison between data and simulation of charge on the central pad of 3-pad clusters in the beamspot (left) and cluster sizes (right).

Figure A.5 shows the results with the corresponding parameter `fCalibration` set to 22.79 ADU/keV (default is 59.08 ADU/keV), with the simulation exhibiting reasonable agreement with the data.

A.2. Example for the gradient boosting method

Consider a model which should predict the outputs $(y_1, y_2) = (10, 20)$. Suppose the first iteration of the classifier ϕ_0 predicts $(\hat{y}_1, \hat{y}_2) = (14, 17)$ and a simple loss function defined as

$$l(y_i, \hat{y}_i) = (y_i - \hat{y}_i)^2 \tag{A.1}$$

and therefore its gradients are

$$\frac{\mathrm{d}l}{\mathrm{d}\hat{y}_i} = -2(y_i - \hat{y}_i). \tag{A.2}$$

Plugging in the values for the desired output and the predictions gives

$$\frac{\mathrm{d}l}{\mathrm{d}\hat{y}_1} = 8 \quad \frac{\mathrm{d}l}{\mathrm{d}\hat{y}_2} = -6 \tag{A.3}$$

Then a new model is trained to predict these gradients, which then can be subtracted from the prediction of the previous model, multiplied with a learning rate λ. Suppose it predicts (10, -4) and the learning rate is set to $\lambda = 0.25$, this would result in the updated predictions $\hat{y}_i'$:

$$\hat{y}_1' = 14 - 0.25 \cdot 8 = 12 \tag{A.4}$$

$$\hat{y}_2' = 17 - 0.25 \cdot (-6) = 18.5 \tag{A.5}$$

As can be seen, the difference of the updated predictions to the desired outputs (10, 20) has been successfully reduced by adding a second model. This procedure is then repeated iteratively, until a minimum or a set exit condition (e.g. maximum number of trees) is reached.

A.3. Pair Cut Optimization

As stated in Section 5.3.2.1, the effectiveness of the `PairPreFilter` highly depends on its position in the cut sequence and needs to be optimized via trial and error. Three different configurations have been selected and their performance evaluated by conducting a full pair analysis and comparing the ratio of Pluto to conversion electrons in the final sample, as listed in Table A.1. In the „early `PairPreFilter`" configuration, the cut is applied before any other photon conversion cuts or PID, while in the „middle "sequence, the `PairPreFilter` is placed after both the χ^2/NDF to vertex and `recMVD` cuts, but still before PID. Finally, in the „late" configuration it is applied after the PID cut as well. The later the `PairPreFilter` is applied, the more conservative it should become, as the amount of random combinations below the set threshold of $m_{\text{inv, candidate}} = 0.025\,\text{GeV/c}^2$ is reduced by every previous cut.

Table A.1.: Cut sequences used for evaluation of the position of the `PairPreFilter` (marked in red).

Early PairPreFilter	Middle PairPreFilter	Late PairPreFilter
p_T	p_T	p_T
recSTSMVD	recSTSMVD	recSTSMVD
rec1TRD	rec1TRD	rec1TRD
PairPreFilter	Chi2/NDF to VTX	Chi2/NDF to VTX
Chi2/NDF to VTX	recSTS	recSTS
recSTS	recMVD	recMVD
recMVD	PairPreFilter	recTRD
recTRD	recTRD	recTOF
recTOF	recTOF	recRICH
recRICH	recRICH	RICH ANN
RICH ANN	RICH ANN	TRD Likelihood
TRD Likelihood	TRD Likelihood	TOF β
TOF β	TOF β	STS dE/dx
STS dE/dx	STS dE/dx	PairPreFilter
Opening Angle	Opening Angle	Opening Angle

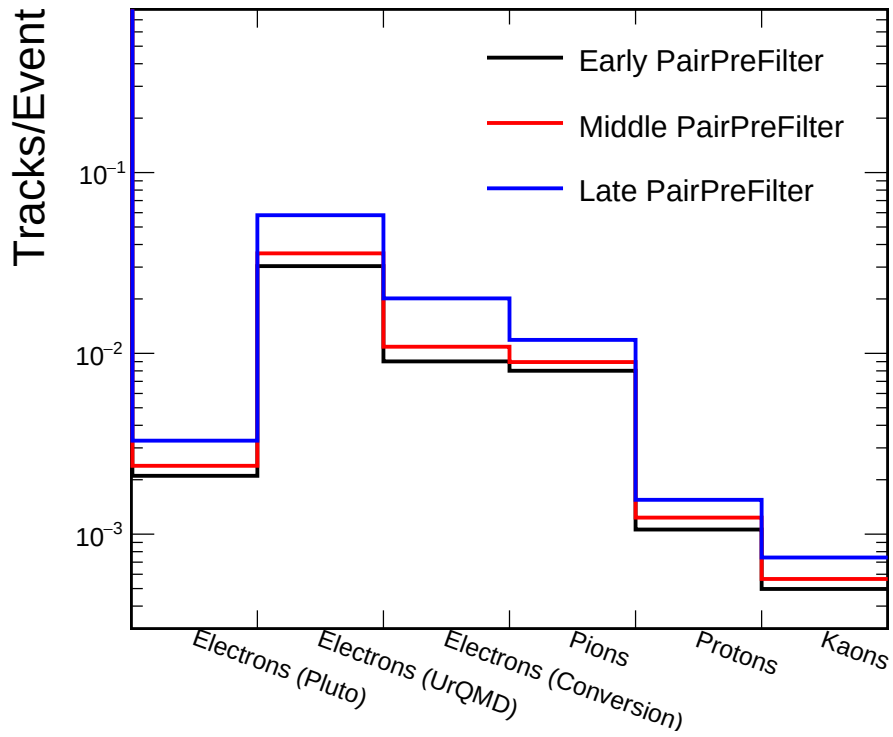

Figure A.6.: Amount of tracks per event from different particle species and sources for the three cut configurations listed in Table A.1.

The resulting amount of tracks from different sources for the three cut configurations are shown in Figure A.6. As expected, the earlier the `PairPreFilter` is implemented, the better is its conversion rejection, while also reducing the efficiency for Pluto electrons.

Table A.2.: Ratios between the amount of electron tracks from Pluto and photon conversion for the three different `PairPreFilter` configurations as listed in Table A.1.

Cut Configuration	Track Ratio $N_{\text{Pluto}}/N_{\text{Conv.}}$
Early PairPreFilter	0.233
Middle PairPreFilter	0.219
Late PairPreFilter	0.163

The achieved ratios of Pluto to conversion electrons in the final samples can be found in Table A.2. Since the „Early `PairPreFilter`“ configuration results in the highest ratio, this sequence is chosen for the analysis in this work. It is important to note that the optimal position of this cut may depend on a

multitude of parameters such as collision energy, detector geometry, other implemented cuts and physics observable. Thus it may differ from analysis to analysis and should always be evaluated with care.

A.4. Improvement of Opening Angle Cut

As stated in Section 5.3.2.3, matching each global track to the track segment with the smallest opening angle will result in vastly different opening angle distributions, depending on the mother particle of the global track. For low invariant mass decays like photon conversions or π^0 Dalitz, many of the matched segments will actually be the true decay partner, leading to a peak at small opening angles. For higher mass decays like $\omega \rightarrow e^+e^-$ on the other hand, the true opening angle is so large, that the matched segment will always be an uncorrelated particle, resulting in a broad distribution, as has been shown in Figure 5.38. Hence, if one is able to reduce the amount of random matches at small opening angles, it may increase the difference between these distributions, leading to a more effective cut.
Therefore, it makes sense to investigate if the amount of these random matches can be reduced already in the matching process on the basis of their momentum and position information. For this, the coordinates at which the global track and the matched track segment exit the tracking stations were examined.

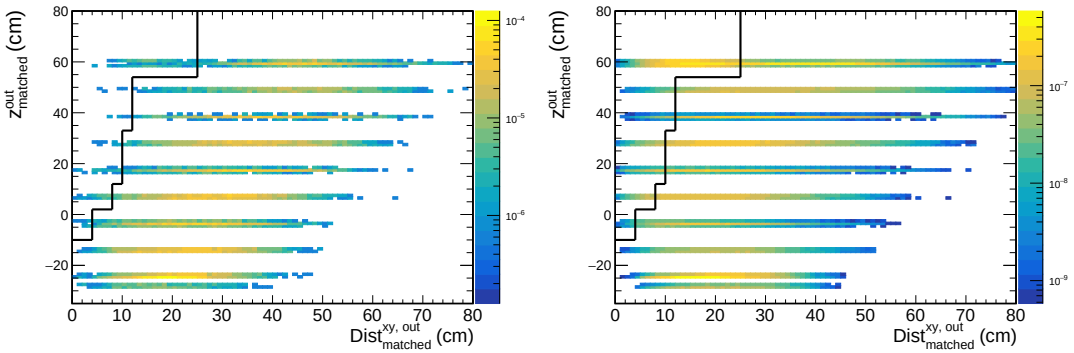

(a) $\gamma \to e^+e^-$, only true matches (b) $\omega \to e^+e^-$, only random matches

Figure A.7.: z-coordinate of the exit point of the matched track segment plotted against the distance in the xy-plane between the exit points of both tracks, as defined in Equation A.6 shown for true matches from photon conversions (left) and random matches from $\omega \to e^+e^-$ decays (right). The black line indicates a selection criterion to reduce the amount of random matches at small opening angles for the ω decay. If the matched segment lies on the left side of the line, it will be rejected and the next closest segment will be matched.

Figure A.7 shows the z-coordinate of the exit point of the track segment $z^{out}_{matched}$ plotted against the distance between the exit points of both tracks in the xy-plane, defined as follows:

$$Dist^{xy,\,out}_{matched} = \sqrt{\left(x^{out}_{matched} - x^{out}_{global}\right)^2 + \left(y^{out}_{matched} - y^{out}_{global}\right)^2} \tag{A.6}$$

In case of a true match, it is expected that the space between the tracks increases with the distance traversed inside the tracking stations, as the particles move away from each other. Therefore, if the segment leaves the tracking stations further downstream, $Dist^{xy,\,out}_{matched}$ should increase, which can be clearly seen in Figure A.7a. For uncorrelated particles on the other hand, this is not the case: Figure A.7b shows a significant amount of random matches at larger $z^{out}_{matched}$ but small $Dist^{xy,\,out}_{matched}$, especially inside the last layer of STS. Thus a selection criterion indicated by the black line was implemented: If the matched track segment lies on the left side of the line in the distribution shown in Figure A.7, it will be rejected and the next closest segment will be matched.

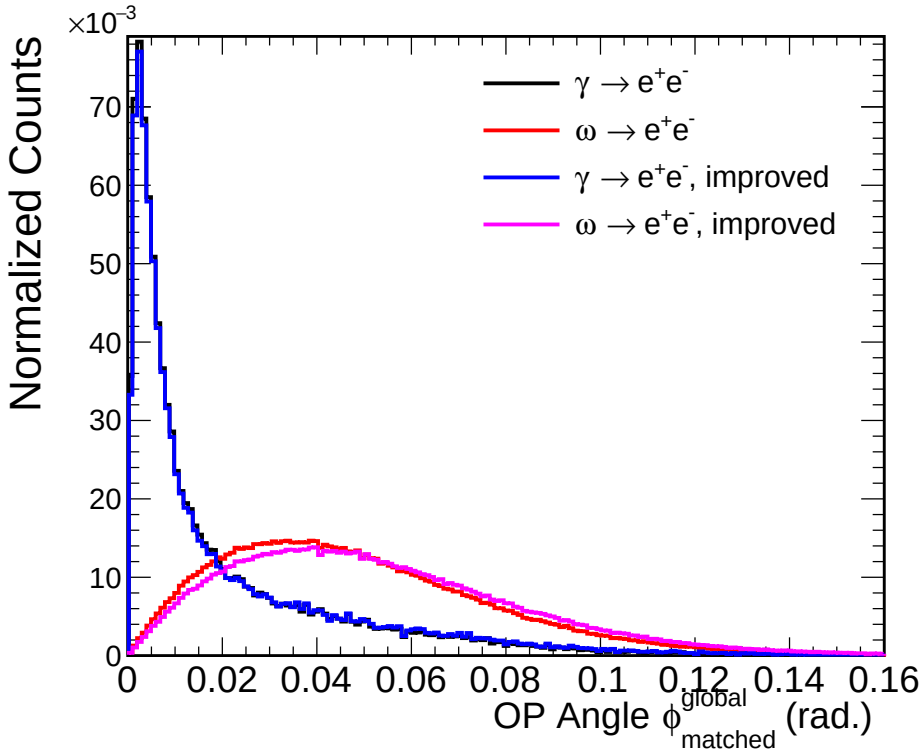

Figure A.8.: Normalized distributions of opening angles between each global track and its respective matched track segment shown for photon conversions and ω with and without the selection criterion to reduce random matches at small opening angles.

This reduces the amount of random matches at small opening angles, while having negligible impact on the true matches, as can be seen Figure A.8. For a hypothetical cut at $\phi^{\text{global}}_{\text{matched}} = 0.02\,\text{rad}$, this would result in an efficiency increase of 2.9 % for tracks from ω. While unfortunately being a rather small improvement, this selection was still implemented, and might be further optimized in the future.

A.5. Random Event Generation

Simulating the full physics of all particle tracks passing through the detector setup with `Geant` and their subsequent reconstruction in `cbmroot` is the most accurate method available for realistically modeling the functionality of the future CBM setup. However, it is also comparatively slow and requires a lot of computing resources such as CPUs, RAM or disk space, which is an issue when simulating a large number of events. Thus, in many cases it is useful to simplify the simulation chain by using approximations or

parametrizations when possible, which has successfully been implemented for various other high energy collision experiments, e.g. A Toroidal LHC ApparatuS (ATLAS) [73] or Compact Muon Solenoid (CMS) [74]. In the case of dielectron analysis for CBM, developments were made by Cornelius Feier-Riesen towards a fast simulation approach to quickly and efficiently generate vast amounts of background events by randomly sampling the multiplicity and momentum distributions of the different particles for a given cut configuration. The method works as follows [75]:

1. Run full simulation and reconstruction chain for a given number of events

2. Run pair analysis with the desired cut configuration

3. Save multiplicity and three-momentum distribution of the remaining tracks for each particle

4. Build new events by randomly sampling the multiplicity and momentum distributions

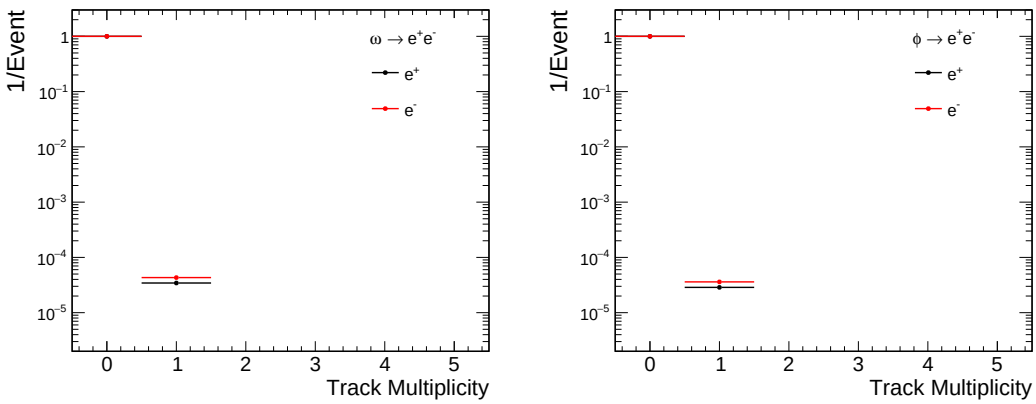

(a) Omega decay (b) Phi decay

Figure A.9.: Multiplicity distributions of electrons and positrons from ω and ϕ decays after all cuts listed in Table A.5.

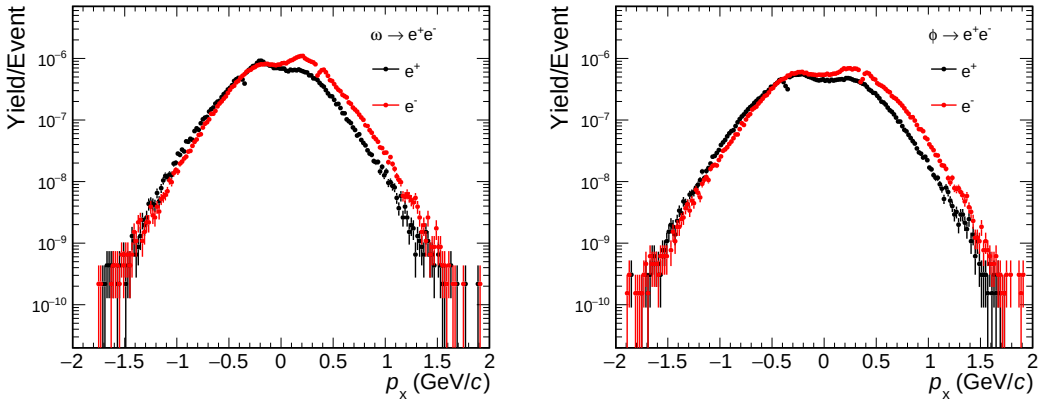

(a) Omega decay (b) Phi decay

Figure A.10.: p_x distributions of electrons and positrons from ω and ϕ decays after all cuts listed in Table A.5.

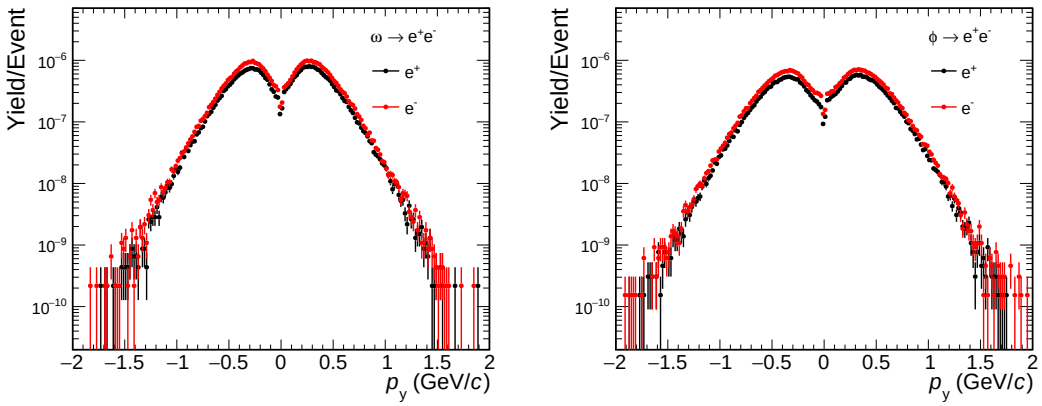

(a) Omega decay (b) Phi decay

Figure A.11.: p_y distributions of electrons and positrons from ω and ϕ decays after all cuts listed in Table A.5.

Some exemplary multiplicity and momentum distributions can be found in Figure A.9, Figure A.10 and Figure A.11. The code for the generation of random events from these distribution was developed by Cornelius Feier-Riesen for the so-called „cbm dielectron framework“ , a different analysis framework than PAPA which is part of `cbmroot` as well. For this work, it was adapted to use the output histograms provided by PAPA as input.

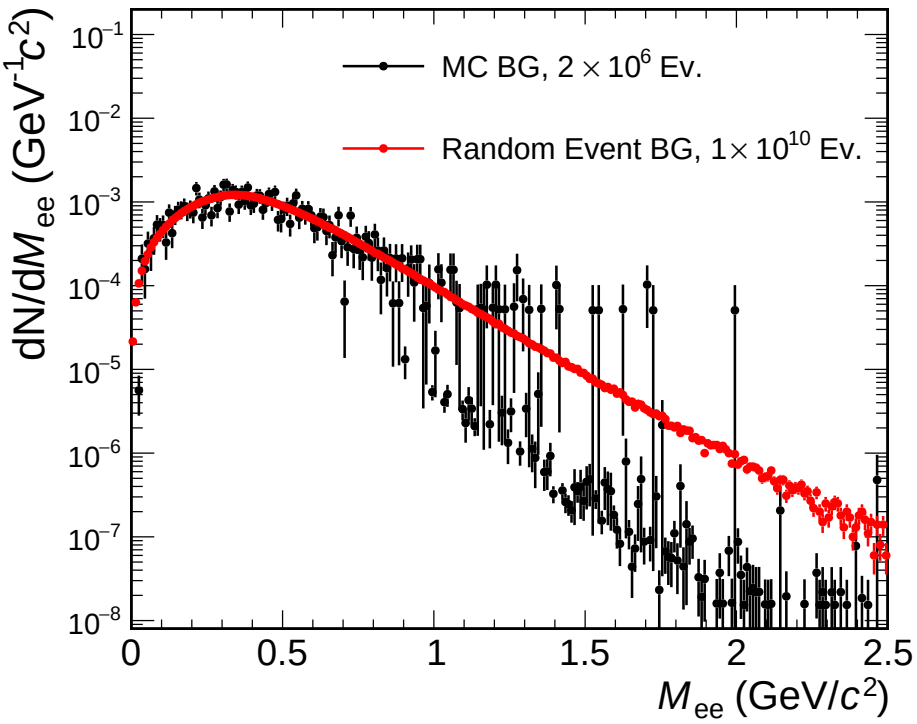

Figure A.12.: Invariant mass spectrum of the combinatorial background from „full“ MC simulations (black) and generated random events (red).

A comparison between the combinatorial background obtained with a full physics simulation and the one from random events is shown in Figure A.12. Due to the simplicity of the random event procedure, it was feasable to produce 10^{10} events, which is 4 orders of magnitude greater than the 2 Million events which were set as a good compromise between statistics, disk space usage and computation time for the full simulation chain. Thus, the statistical uncertainties for the random events are significantly smaller, reducing fluctuations. For the background obtained with the full simulation chain, these fluctuations are especially evident in the region of $M_{ee} \gtrsim 1\,\mathrm{GeV/c^2}$. Here, in most bins, only entries of pairs with at least one track from Pluto remain, which can be identified by their smaller uncertainties. While these entries give the impression of filled bins, they are actually underestimating the combinatorial background. Therefore when using the background obtained with the full simulation chain, a wide rebinning would be necessary in this mass area, which is not the case for the random event background.

A.6. Additonal Equations

Correction function for energy loss via collisions of electrons and positrons (see Equation 3.2) [40]:

$$F(\tau,\beta) = \begin{cases} 1-\beta^2+\frac{\tau^2/8-(2\tau+1)\ln 2}{(\tau+1)^2} & \text{for } e^- \\ 2\ln 2-\frac{\beta^2}{12}\left(23+\frac{14}{\tau+2}+\frac{10}{(\tau+2)^2}+\frac{4}{(\tau+2)^3}\right) & \text{for } e^+ \end{cases} \tag{A.7}$$

A.7. Additional Tables

Table A.3.: Measurement runs recorded at the DESY2019 test beam campaign using the ^{55}Fe source at different anode voltages.

Run Nr.	Anode Voltage (V)
66	−1680
67	−1710
68	−1740
69	−1770
64	−1800
70	−1830
71	−1860
72	−1890
73	−1920
74	−1950

Table A.4.: Measurement runs recorded at the DESY2019 test beam campaign used for the comparison of the different radiators. All data were recorded using an electron beam at $p = 3\,\text{GeV/c}$. The MWPC was operated at $U_{\text{anode}} = -1800\,\text{V}$ and $U_{\text{drift}} = 500\,\text{V}$. As stated in Section 4.2.5, it is can not be confirmed if the values for the radiator width written in the measurement log for run 49 and 59 are correct, which is why they are marked with questions marks.

Run Nr.	Radiator Width (cm)	Iron Source
46	31.5	yes
49	21.5 (?)	no
50	11.5	yes
54	1.5	yes
55	0	yes
59	16.5 (?)	no
61	26.5	no

Table A.5.: Cuts used for dielectron analysis with hadron rejection via conventional box cuts

Cut Class	Cut Name	Range
PreCuts	p_T	$p_T > 0.05\,\mathrm{GeV/c}$
	recSTSMVD	Nr. of STS+MVDHits > 3
	rec1TRD	Nr. of TRDHits > 0
	PairPreFilter	m_{inv} of pair candiate $> 0.025\,\mathrm{GeV/c^2}$
	Chi2/NDF to VTX	χ^2/NDF to vertex ≥ 3
	recSTS	Nr. of STSHits > 2
	recMVD	Nr. of MVDHits > 2
RECCutsPID	recTRD	Nr. of TRDHits > 2
	recTOF	Nr. of TOFHits > 0
PIDCuts	recRICH	Nr. of RICHHits > 5
	RICH ANN	80% Ele. Efficiency
	TRD Likelihood	70% Ele. Efficiency
	TOF β	$-5.28 \cdot 10^{-3} \leq \Delta\beta_{\mathrm{electron}} \leq 5.28 \cdot 10^{-3}$
	STS $\mathrm{d}E/\mathrm{d}x$	$\mathrm{d}E/\mathrm{d}x_{\mathrm{STS}} < 3 \times 10^4\,\mathrm{e}/300\mu\mathrm{m}$ for $0 \leq p \leq 1.6\,\mathrm{GeV/c}$
Segment Cut	Opening Angle	

Table A.6.: Cuts used for dielectron analysis with hadron rejection via machine learning classifier

Cut Class	Cut Name	Range
PreCuts	p_T	$p_T > 0.05\,\mathrm{GeV/c}$
	recSTSMVD	Nr. of STS+MVDHits > 3
	rec1TRD	Nr. of TRDHits > 0
	PairPreFilter	m_{inv} of pair candiate $> 0.025\,\mathrm{GeV/c^2}$
	Chi2/NDF to VTX	χ^2/NDF to vertex ≥ 3
	recSTS	Nr. of STSHits > 2
	recMVD	Nr. of MVDHits > 2
RECCutsPID	recTRD	Nr. of TRDHits > 2
	recTOF	Nr. of TOFHits > 0
PIDCuts	recRICH	Nr. of RICHHits > 5
	Global BDT Classifier (XGBoost)	50% Ele. Efficiency
Segment Cut	Opening Angle	

A.8. Additional Figures

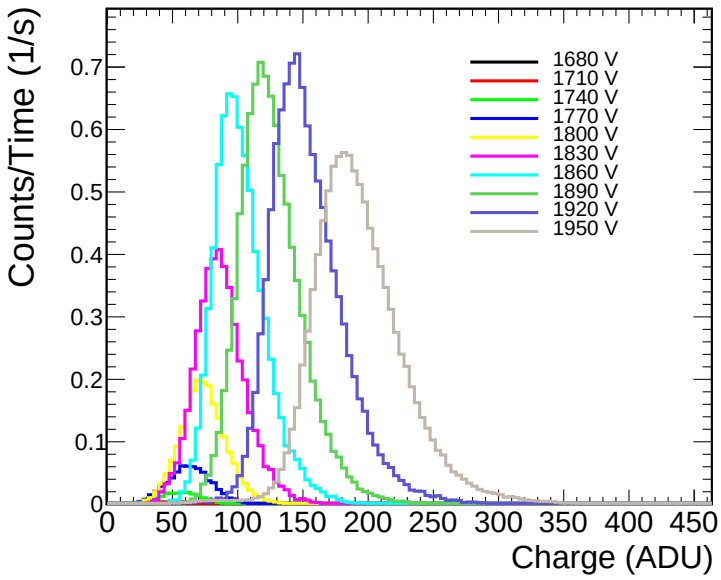

Figure A.13.: Reconstructed charge spectra at the source spot for different anode voltages, normalized by measurement time.

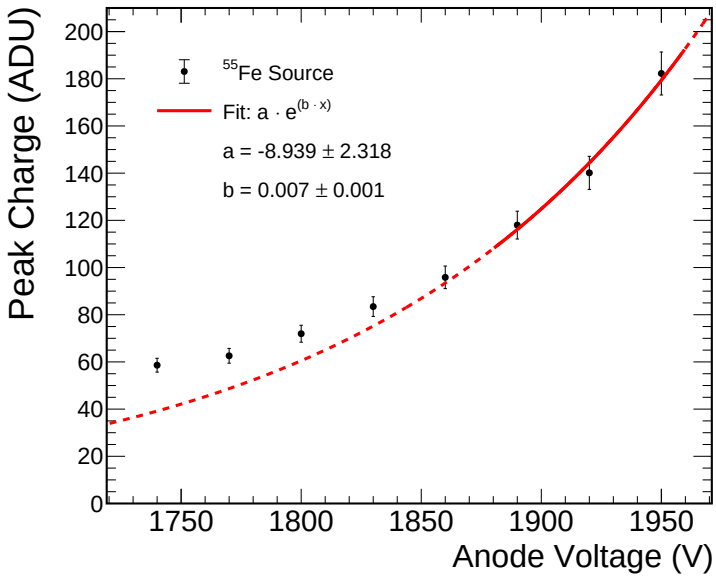

Figure A.14.: Peak positions of the reconstructed charge spectra at the source spot as a function of the anode voltage, including an exponential fit using the last three data points.

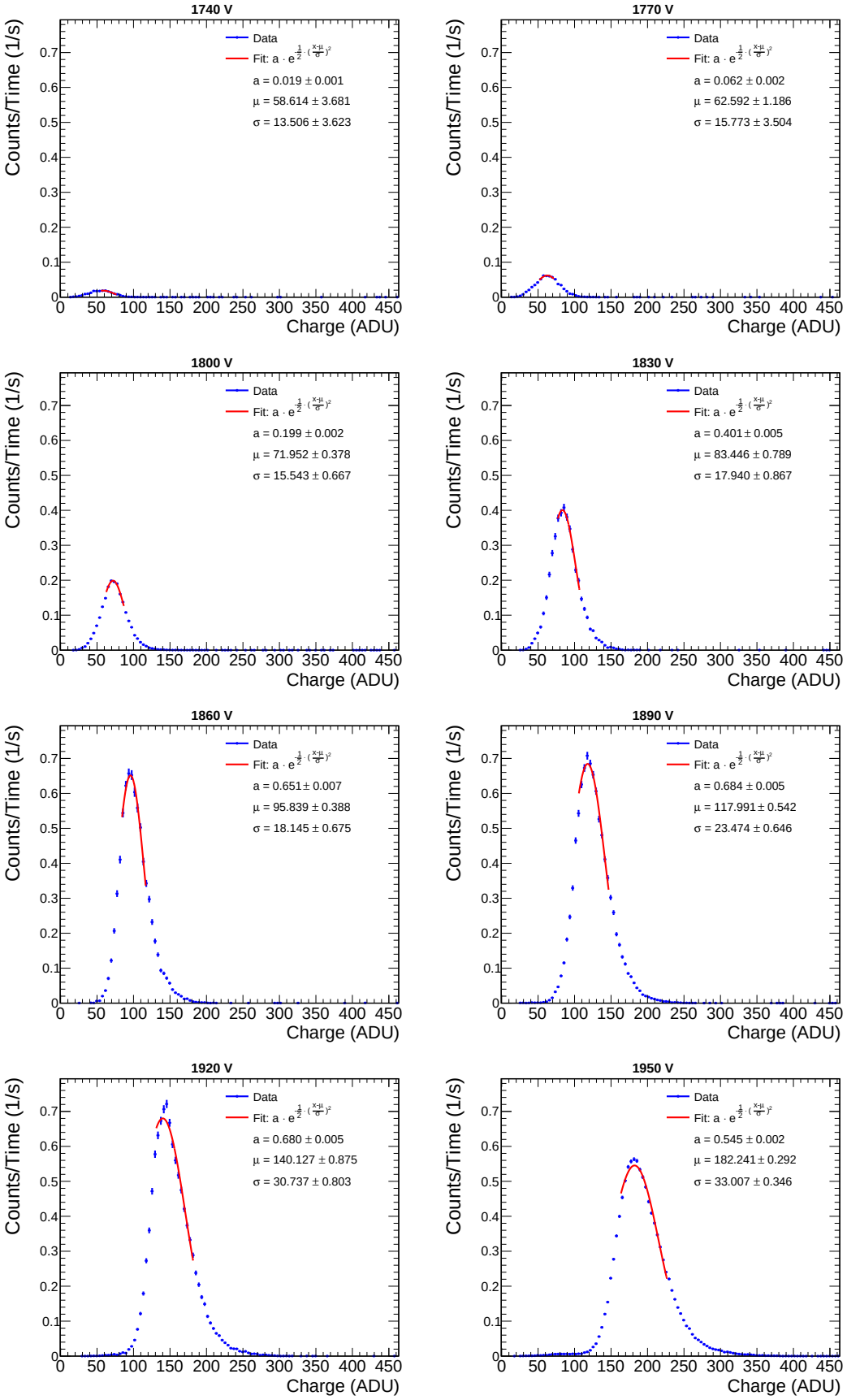

Figure A.15.: ^{55}FE spectra recorded at different anode voltages and fitted with a Gaussian function. As fit range 10 % to the left and 25 % to the right of the maximum bin is chosen.

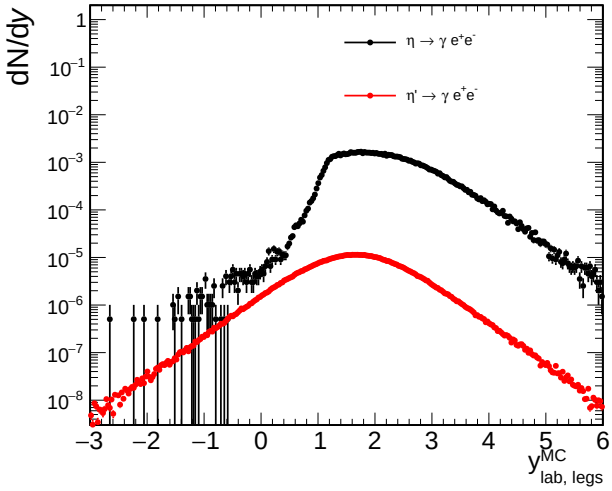

Figure A.16.: Rapidity distribution of all MC tracks of electrons/positrons in full phase space originating from the three-body-decays of η and η', normalized by the number of simulated events. The η originate from UrQMD, while the η' are simulated with Pluto.

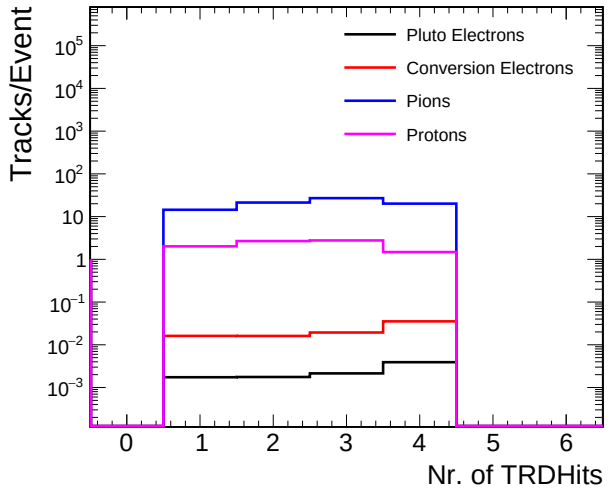

Figure A.17.: Number of `TRDHits` per track of different particle species, after all `PreCuts` are applied (see Table A.5). Note that this selection already includes a cut requiring at least 1 `TRDHit`. While its most likely for electron tracks to have 1 `TRDHit`, the distributions for pions and protons peak at 3 `TRDHits`.

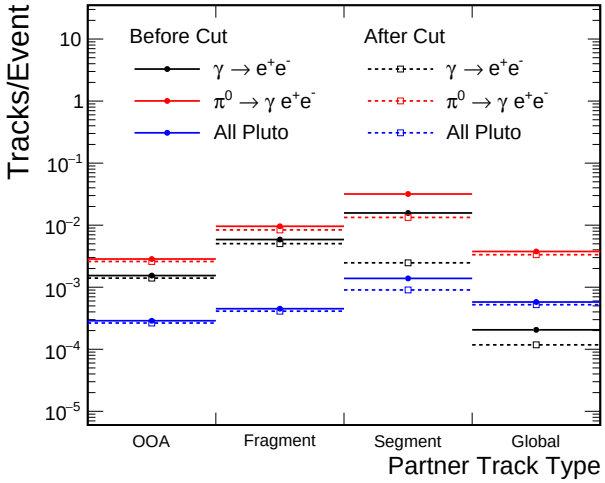

Figure A.18.: Track types of partners of global tracks from different decays before (closed symbols) and after (open symbols) the opening angle cut. For the definition of track types see the beginning of Section 5.3.2.2 and Figure 5.36. In contrast to the $\omega \rightarrow e^+e^-$ decay shown in Figure 5.40, the distribution for all pluto decays combined exhibits a similar shape as the one of π^0, since it is dominated by many low mass decays of the in-medium modified ρ^0.

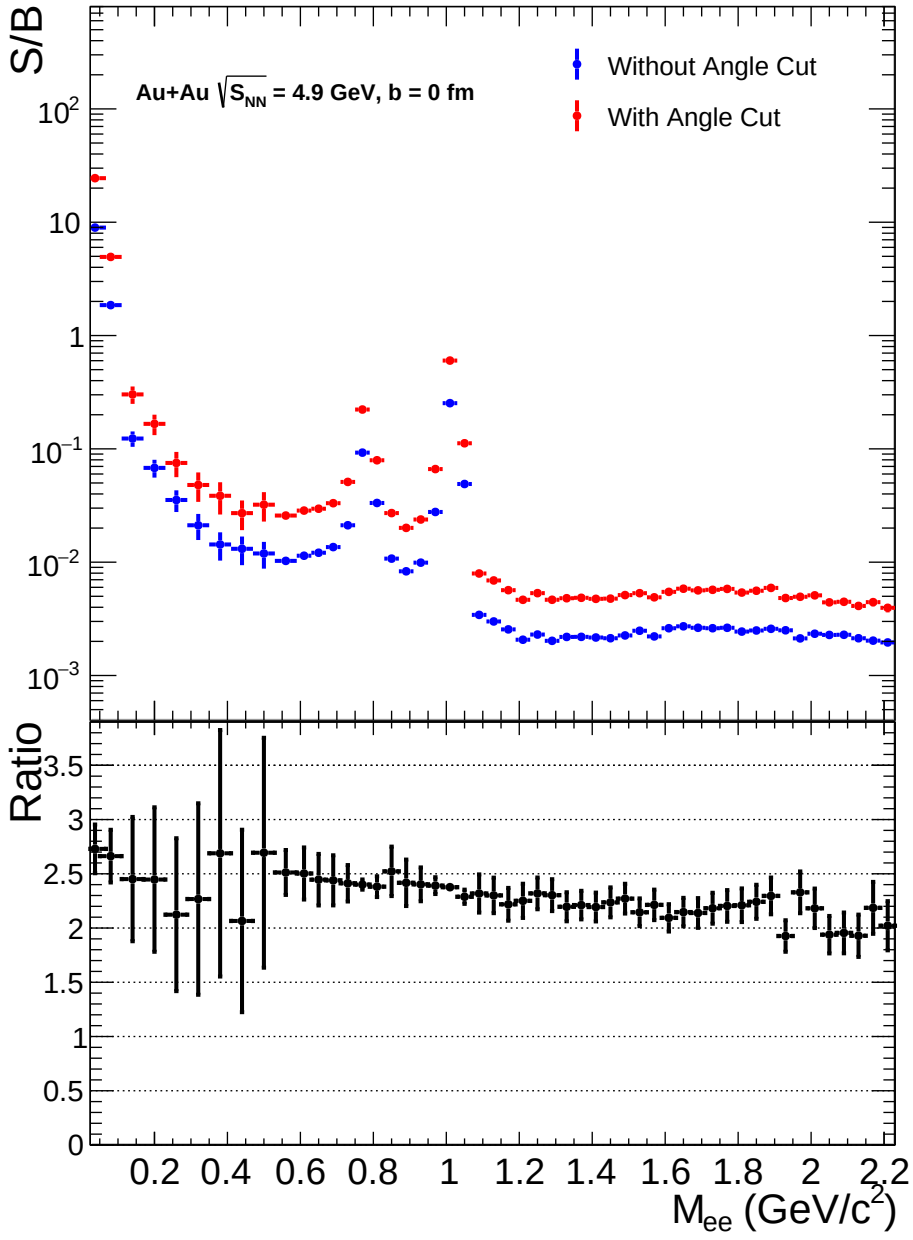

Figure A.19.: Comparison between Signal-to-Background (S/B) ratio achieved with and without the opening angle cut described in Section 5.3.2.3, calculated as the sum of all dilepton signals shown in Figure 5.44 identified with MC information divided by the combinatorial background approximated with 10^{10} *random events* (see Section A.5). The lower panel shows the ratio of $\frac{S/B_{\text{with cut}}}{S/B_{\text{without cut}}}$.

A.9. Acronyms

ADC Analog to Digital Converter

ADU ADC Unit

AFCK AMC FMC Carrier Kintex

ALICE A Large Ion Collider Experiment

AMC Advanced Mezzanine Card

ANN Artifical Neural Network

ASIC Application-Specific Integrated Circuit

ATLAS A Toroidal LHC ApparatuS

BDT Boosted Decision Tree

BNL Brookhaven National Laboratory

CAD Computer Aided Design

CBM Compressed Baryonic Matter

CBM-TRD Transition Radiation Detector for the CBM Experiment

CERN Conseil Européen pour la Recherche Nucléaire

CMS Compact Muon Solenoid

CSA Charge Sensitive Amplifier

CMOS Complementary Metal-Oxide-Semiconductor

DAQ Data AcQuisition

DESY Deutsches Elektronen-SYnchrotron

DSP Digital Signal Processor

EM ElectroMagnetic

FAIR Facility for Antiproton and Ion Research

FLES First-Level Event Selector

FLIB FLES Interface Board

FMC FPGA Mezzanine Card

FNR Forced Neighbor Readout

FPGA Field Programmable Gate Array

FSD Forward Spectator Detector

GEANT GEometry ANd Tracking

GSI Gesellschaft für SchwerIonenforschung

HADES High Acceptance Dielectron Spectrometer

IC Integrated Circuit

IFIN-HH Horia Hulubei National Institute of Physics and Nuclear Engineering

IKF Institut für Kernphysik Frankfurt

IKP Institut für Kernphysik Münster

IMR Intermediate Mass Region

LHC Large Hadron Collider

LMR Low Mass Region

MaPMT Multi-anode PhotoMultiplier Tube

MAPS Monolithic Active Pixel Sensor

MC Monte Carlo

MIP Minimum Ionizing Particle

ML Machine Learning

MPV Most Probable Value

MRPC Multi-Gap Resistive-Plate Chamber

MUCH Muon Chamber

MVD Micro Vertex Detector

MWPC Multi Wire Proportional Chamber

NA North Area

NICA Nuclotron-based Ion Collider Facility

NIST National Institute of Standards and Technology

OOA Out-Of-Acceptance

PAPA Pair Analysis Package

PE PolyEthylene

PETRA Positron-Elektron-Tandem-Ring-Anlage

PID Particle Identification

PMT PhotoMultiplier Tube

QCD Quantum Chromodynamics

QFT Quantum Field Theory

QGP Quark-Gluon Plasma

RHIC Relativistic Heavy Ion Collider

RICH Ring Imaging Cherenkov

ROC Receiver Operating Characteristic

SHM Statistical Hadronization Model

S/B Signal-to-Background

SIS SchwerIonenSynchrotron

SM Standard Model

SPADIC Self-triggered Pulse Amplification and Digitization ASIC

STR Self-TRiggered

STS Silicon Tracking System

TOF Time-Of-Flight System

TR Transition Radiation

TRD Transition Radiation Detector

TSA Time Slice Archive

UrQMD Ultra-relativistic Quantum Molecular Dynamics

List of Tables

List of Figures

Acknowledgements

During the long process of working on this thesis, and the even longer process of my journey through school and university, a countless number of people supported me, for which I want to express my deepest gratitude. I want to thank my parents Monika and Sven for everything, for always being there when I need them and for their unconditional support. They also kindled my interest in science as a child.
Nevertheless, physics seemed to me a bit dry and somewhat boring until my teacher Jörg Flothow introduced me into the world of Newtonean Mechanics in 10th grade. Thanks to his great teaching style, physics „clicked“ for me, and I was thinking about studying it after finishing school. This idea became even clearer to me during my two last years of school in the great physics *Leistungskurs* by Petra Klawikowski. When I tell people that I am doing a Phd in physics the typical reactions are "How can you do that?" and "I was bad/hated physics at school", and I always point to the great teachers I had, and how much this shaped my personal connection to physics. Thank you so much for this!
But my luck of having great educators did not end there. Prof. Rohlfing did an amazing job with his physics 1 to 3 lectures which I had the pleasure to attend in my first semesters, laying the foundation of anything I learned afterwards. With his great *Intoduction to nuclear physics* lecture, Prof. Khoukaz sparked my interest in nuclear and particle physics, causing me to join the group of the Profs. Wessels and Klein-Bösing for my bachelor thesis. Even though a lot of things did not go as expected with this thesis project, as is usual in experimental physics, their great mentorship and the welcoming atmosphere in the group made me want to stay there for my master thesis. Any doubts I may have had were washed away by being introduced to the CBM collaboration at my first (in total the 29th) CBM collaboration meeting in 2017. Being able to witness the whole scale of such a large project early in my research career, and meeting people from all over the world working on the same thing as myself was a great experience, which I am grateful for. Thank you to the whole CBM team, past and present!
When I returned for my master thesis, Prof. Andronic had taken over the group leadership, who became my mentor not only for the master project, but also my Phd. Thank you so much for giving me the opportunity to seamlessly continue working in this field I am passionate about, for all the helpful guidance, discussions and support. The door to your office was always

open, literally and figuratively. Still, you never held my hand too much or constrained me, instead I was able to shape my research on my own, while knowing that there was help if I would need it. This is a difficult balance to achieve, so thank you again, for doing it so well!
Relatively late in my studies I was introduced to Prof. Galatyuk, who made me join the CBM Dilepton group. The manner in which you made me fall in love with this (sub)field is nothing but astonishing: Like the QGP does with thermal dielectrons, you radiate your passion for these very special $e+e-$ pairs and it was truly contagious for me! Thank you so much for this, for all the amazing guidance, and for making me and my contributions feel so valued.
Many thanks also to the whole group in Münster (past and present), especially my office mates Felix, Axel, Luisa, Alexandra, but also of course Philipp K., Ruben, Peter, Ailec, Archita, Henrik, Norbert and all. You are the reasons coming to the office was always a great pleasure, with interesting and enjoyable coffee breaks, discussions, great summer and winter parties, cooking evenings, bike tours, restaurant visits and everything else.
I also want to thank Ruben, Pavish and my parents for proof reading and many helpful suggestions. And thank you to Etienne for taking the time to introduce me to the PAPA framework and still answering my emails long after your contract at the university ended. My thanks go out also to Cornelius who showed me his code for the random event generation and answered my questions so that I was able to quickly adapt it to my needs.
Lastly, it might sound corny, but I really do think the real treasure are the friends we made along the way. And nowhere else have I found more amazing friends than in this 12 year long endeavor. Chris, Tabea, Flo, Daniel, Kenny, Alex, Max, Franzi, Pavish, Hannes, Seb, Freddy, Hanna, Jan, Marie, Marie and many more. You were, and are, always there for me, in the many many great but also very bad times. I cannot express enough how precious such a loving and caring support system is, and how grateful and proud I am to call you **my** friends. I would have never made it this far without you.
I did not choose the entry quote at random. Thank you to every person mentioned above, explicitly or implicitly, for giving me the feeling of being welcomed, appreciated and valued, wanting me to stay, be it in physics, in the group of Profs. Andronic and Klein-Bösing, in CBM and the dilepton group, or in Münster, I felt truly at the place where I belong, home. Because *home is where they want you to stay longer*.

Bibliography

[1] Stephen King. *Revival*. Scribner, 2014.

[2] Lyndon Evans and Philip Bryant. LHC machine. *Journal of Instrumentation*, 3(08):S08001, aug 2008.

[3] Anton Andronic, Peter Braun-Munzinger, Krzysztof Redlich, and Johanna Stachel. Decoding the phase structure of QCD via particle production at high energy. *Nature*, 561(7723):321–330, 2018.

[4] Wolfgang Demtröder. *Experimentalphysik 4*. Springer Spektrum Berlin, Heidelberg, 2017.

[5] P. Senger for the CBM Collaboration. Probing dense qcd matter in the laboratory—the cbm experiment at fair. *Physica Scripta*, 95(7):074003, may 2020.

[6] Edmond Iancu. QCD in heavy ion collisions. In *2011 European School of High-Energy Physics*, pages 197–266, 2014.

[7] M.A. Lisa. Timescales in heavy-ion collisions. *Acta Physica Polonica B*, 47(7):1847, 2016.

[8] Sylvie Braibant, Giorgio Giacomelli, and Maurizio Spurio. *Particles and Fundamental Interactions: An Introduction to Particle Physics*. Springer Dodrecht, 2011.

[9] John F. Donoghue, Eugene Golowich, and Barry R. Holstein. *Dynamics of the Standard Model*. Cambridge Monographs on Particle Physics, Nuclear Physics and Cosmology. Cambridge University Press, 2 edition, 2023.

[10] Jana N. Guenther. Overview of the QCD phase diagram: Recent progress from the lattice. *Eur. Phys. J. A*, 57(4):136, 2021.

[11] Helmut Satz. The quark-gluon plasma – a short introduction. *Nuclear Physics A*, 862-863:4–12, 2011. The Sixth International Conference on Physics and Astrophysics of Quark Gluon Plasma (ICPAQGP-2010).

[12] Patrick Steinbrecher. The qcd crossover at zero and non-zero baryon densities from lattice qcd. *Nuclear Physics A*, 982:847–850, 2019.

The 27th International Conference on Ultrarelativistic Nucleus-Nucleus Collisions: Quark Matter 2018.

[13] M. A. Stephanov. QCD phase diagram and the critical point. *International Journal of Modern Physics A*, 20(19):4387–4392, 2005.

[14] T. Ablyazimov et al. Challenges in QCD matter physics –The scientific programme of the Compressed Baryonic Matter experiment at FAIR. *Eur. Phys. J.*, A53(3):60, 2017.

[15] Shusu Shi. *Event anisotorpy v2 at STAR*. Phd thesis, Central China Normal University, 2010.

[16] Wojciech Florkowski. *Phenomenology of Ultra-Relativistic Heavy-Ion Collisions*. 2010.

[17] Ulrich Heinz. Thermalization at RHIC. In *AIP Conference Proceedings*, volume 739, pages 163–180, 2004.

[18] Wit Busza, Krishna Rajagopal, and Wilke van der Schee. Heavy ion collisions: The big picture and the big questions. *Annual Review of Nuclear and Particle Science*, 68(1):339–376, 2018.

[19] Bengt Friman, Claudia Höhne, Jorn Knoll, Stefan Leupold, Jorgen Randrup, Ralf Rapp, and Peter Senger, editors. *The CBM physics book: Compressed baryonic matter in laboratory experiments*, volume 814. 2011.

[20] Ralf Rapp. Dilepton Production in Heavy-Ion Collisions. *PoS*, CPOD2013:008, 2013.

[21] Tetyana Galatyuk. Private communication, 2022.

[22] Sidney D. Drell and Tung-Mow Yan. Massive lepton-pair production in hadron-hadron collisions at high energies. *Phys. Rev. Lett.*, 25:316–320, Aug 1970.

[23] L. D. McLerran and T. Toimela. Photon and dilepton emission from the quark-gluon plasma: Some general considerations. *Phys. Rev. D*, 31:545–563, Feb 1985.

[24] R. L. Workman et al. Review of Particle Physics. *Prog. Theor. Exp. Phys.*, 2022:083C01, 2022.

[25] Tetyana Galatyuk. Cbm dilepton wiki page. https://cbm-wiki.gsi.de/PWG/CbmDileptonInfoFilesAuAu11000, 2022.

[26] Ralf Rapp and Hendrik van Hees. Thermal dileptons as fireball thermometer and chronometer. *Physics Letters B*, 753:586–590, 2016.

[27] Tetyana Galatyuk. Future facilities for high μ_B physics. *Nucl. Phys. A*, 982:163–169, 2019.

[28] Tetyana Galatyuk, Paul M. Hohler, Ralf Rapp, Florian Seck, and Joachim Stroth. Thermal Dileptons from Coarse-Grained Transport as Fireball Probes at SIS Energies. *Eur. Phys. J. A*, 52(5):131, 2016.

[29] Xiaofeng Luo, Qun Wang, Nu Xu, and Pengfei Zhuang, editors. *Properties of QCD Matter at High Baryon Density*. Springer, 2022.

[30] R. Arnaldi et al. Evidence for radial flow of thermal dileptons in high-energy nuclear collisions. *Phys. Rev. Lett.*, 100:022302, Jan 2008.

[31] P.M. Hohler and R. Rapp. Dileptons and chiral symmetry restoration. *Nuclear and Particle Physics Proceedings*, 276-278:253–256, 2016. 7th International Conference on Hard and Electromagnetic Probes of High Energy Nuclear Collisions.

[32] Azumi Sakai, Masayasu Harada, Chiho Nonaka, Chihiro Sasaki, Kenta Shigaki, and Satoshi Yano. Probing the QCD phase transition with chiral mixing in dilepton production. 8 2023.

[33] FAIR_GSI_de. X (formely twitter) post. https://twitter.com/fair_gsi_de/status/886125178496835585, 2017. Accessed: 14.04.2023.

[34] M. Durante et al. All the fun of the FAIR: fundamental physics at the facility for antiproton and ion research. *Physica Scripta*, 94(3):033001, 2019.

[35] The CBM Collaboration. The Transition Radiation Detector of the CBM Experiment at FAIR : Technical Design Report for the CBM Transition Radiation Detector (TRD). Technical report, Darmstadt, 2018.

[36] The CBM Collaboration. The Micro Vertex Detector of the CBM Experiment at FAIR : Technical Design Report for the CBM Micro Vertex Detector (MVD). Technical Report FAIR Technical Design Report, Darmstadt, 2021.

[37] The CBM Collaboration. The Silicon Tracking System of the CBM Experiment at FAIR : Technical Design Report for the CBM Silicon Tracking System (STS). Technical Report FAIR Technical Design Report, Darmstadt, 2013.

[38] The CBM Collaboration. The Ring Imaging Cherenkov Detector of the CBM Experiment at FAIR : Technical Design Report for the CBM Ring Imaging Cherenkov (RICH) Detector. Technical report, Darmstadt, 2013.

[39] The CBM Collaboration. The Time-of-Flight System of the CBM Experiment at FAIR : Technical Design Report for the CBM Time-of-Flight System (TOF). Technical Report FAIR Technical Design Report, Darmstadt, 2014.

[40] W. R. Leo. *Techniques for Nuclear and Particle Physics Experiments: A How to Approach*. 1987.

[41] M.J. Berger, J.S. Coursey, M.A. Zucker, and J. Chang. Estar, pstar, and astar: Computer programs for calculating stopping-power and range tables for electrons, protons, and helium ions (version 2.0.1). https://physics.nist.gov/Star, 2005.

[42] Konrad Kleinknecht. *Detektoren für Teilchenstrahlung*. Vieweg+Teubner Verlag Wiesbaden, 2005.

[43] A. Andronic et al. Energy loss of pions and electrons of 1–6 GeV/c in drift chambers operated with Xe,CO2(15%). *Nuclear Instruments and Methods in Physics Research Section A: Accelerators, Spectrometers, Detectors and Associated Equipment*, 519(3):508–517, 2004.

[44] Walter Blum, Luigi Rolandi, and Werner Riegler. *Particle detection with drift chambers*. Particle Acceleration and Detection. 2008.

[45] X. Artru, G. B. Yodh, and G. Mennessier. Practical Theory of the Multilayered Transition Radiation Detector. *Phys. Rev. D*, 12:1289, 1975.

[46] Michael L. Cherry, Gernot Hartmann, Dietrich Müller, and Thomas A. Prince. Transition radiation from relativistic electrons in periodic radiators. *Phys. Rev. D*, 10:3594–3607, Dec 1974.

[47] A. Andronic and J.P. Wessels. Transition radiation detectors. *Nuclear Instruments and Methods in Physics Research Section A: Accelerators, Spectrometers, Detectors and Associated Equipment*, 666:130–147, 2012.

[48] A. Bercuci, M. Petrovici, et al. An Enhanced Tracking Device For the Inner Region of the TRD wall : Addendum to the Technical Design Report for the CBM Transition Radiation Detector (TRD). Technical report, Darmstadt, 2021.

[49] R. Diener, J. Dreyling-Eschweiler, H. Ehrlichmann, I.M. Gregor, U. Kötz, U. Krämer, N. Meyners, N. Potylitsina-Kube, A. Schütz, P. Schütze, and M. Stanitzki. The DESY II test beam facility. *Nuclear Instruments and Methods in Physics Research Section A: Accelerators, Spectrometers, Detectors and Associated Equipment*, 922:265–286, 2019.

[50] Cyrano Bergmann. *Development, Simulation and Test of Transition Radiation Detector Prototypes for the Compressed Baryonic Matter Experiment at the Facility for Antiproton and Ion Research*. Phd thesis, Westfälische Wilhelms-Universität Münster, 2014.

[51] G. Audi, O. Bersillon, J. Blachot, and A.H. Wapstra. The NUBASE evaluation of nuclear and decay properties. *Nuclear Physics A*, 729(1):3–128, 2003.

[52] M.-M. Bé, V. Chisté, C. Dulieu, M.A. Kellett, X. Mougeot, A. Arinc, V.P. Chechev, N.K. Kuzmenko, T. Kibédi, A. Luca, and A.L. Nichols. *Table of Radionuclides*, volume 8 of *Monographie BIPM-5*. Bureau International des Poids et Mesures, Pavillon de Breteuil, F-92310 Sèvres, France, 2016.

[53] Schaltungstechnik und Simulation (SuS). *SPADIC 2.2 Manual*. Universität Heidelberg, 2019. Private Communication.

[54] Adrian Meyer-Ahrens. Auslese eines Szintillationszählers mit selbstgetriggerter Elektronik. Bachelor's thesis, Westfälische Wilhelms-Universität Münster, 2016.

[55] Etienne Bechtel. *Development of a detector simulation and reconstruction for the CBM-TRD and the analysis of thermal dielectron pairs in 12 AGeV Au+Au collisions*. Phd thesis, Johann Wolfgang Goethe Universität Frankfurt a. M., 2020.

[56] Etienne Bechtel, Daniel Giang, Cyrano Bergmann, and David Emschermann. The CBM-TRD digitizer software (rectangular pad design). CBM computing note CBM-CN-20005, 2020.

[57] Julian Book. Pair Analysis Package - PAPa. https://indico.gsi.de/event/3620/contributions/16119/attachments/11695/14338/papa.pdf, April 2016.

[58] S.A. Bass, M. Belkacem, M. Bleicher, M. Brandstetter, L. Bravina, C. Ernst, L. Gerland, M. Hofmann, S. Hofmann, J. Konopka, G. Mao, L. Neise, S. Soff, C. Spieles, H. Weber, L.A. Winckelmann, H. Stöcker, W. Greiner, Ch. Hartnack, J. Aichelin, and N. Amelin. Microscopic models for ultrarelativistic heavy ion collisions. *Progress in Particle and Nuclear Physics*, 41:255–369, 1998.

[59] M Bleicher, E Zabrodin, C Spieles, S A Bass, C Ernst, S Soff, L Bravina, M Belkacem, H Weber, H Stöcker, and W Greiner. Relativistic hadron-hadron collisions in the ultra-relativistic quantum molecular dynamics model. *Journal of Physics G: Nuclear and Particle Physics*, 25(9):1859, Sep 1999.

[60] Marcus Bleicher and Elena Bratkovskaya. Modelling relativistic heavy-ion collisions with dynamical transport approaches. *Progress in Particle and Nuclear Physics*, 122:103920, 2022.

[61] I. Fröhlich et al. Pluto: A Monte Carlo Simulation Tool for Hadronic Physics. *PoS*, ACAT:076, 2007.

[62] I Fröhlich et al. Design of the pluto event generator. *Journal of Physics: Conference Series*, 219(3):032039, apr 2010.

[63] J. Cleymans, H. Oeschler, K. Redlich, and S. Wheaton. Comparison

of chemical freeze-out criteria in heavy-ion collisions. *Phys. Rev. C*, 73:034905, Mar 2006.

[64] René Brun, F Bruyant, Federico Carminati, Simone Giani, M Maire, A McPherson, G Patrick, and L Urban. *GEANT: detector description and simulation tool; March 1994*. CERN Program Library. CERN, Geneva, 1994. Long Writeup W5013.

[65] Henrik Schiller. Application of machine learning to particle identification for dielectron analysis in cbm. Master's thesis, Westfälische Wilhelms-Universität Münster, 2022.

[66] R.D. Appuhn, K. Heinloth, E. Lange, R. Oedingen, and A. Schlösser. Transition radiation detectors for electron identification beyond 1 gev/c. *Nuclear Instruments and Methods in Physics Research Section A: Accelerators, Spectrometers, Detectors and Associated Equipment*, 263(2):309–318, 1988.

[67] Tianqi Chen and Carlos Guestrin. Xgboost: A scalable tree boosting system. In *Proceedings of the 22nd ACM SIGKDD International Conference on Knowledge Discovery and Data Mining*, KDD '16, page 785–794, New York, NY, USA, 2016. Association for Computing Machinery.

[68] Pankaj Mehta, Marin Bukov, Ching-Hao Wang, Alexandre G.R. Day, Clint Richardson, Charles K. Fisher, and David J. Schwab. A high-bias, low-variance introduction to machine learning for physicists. *Physics Reports*, 810:1–124, 2019. A high-bias, low-variance introduction to Machine Learning for physicists.

[69] Salomé Sanchez, Divish Rengasamy, Christopher Hyde, Grazziela Figueredo, and Benjmain Rothwell. Machine learning to determine the main factors affecting creep rates in laser powder bed fusion. *Journal of Intelligent Manufacturing*, 32, 12 2021.

[70] Tetyana Galatyuk. *Di-electron spectroscopy in HADES and CBM: from p+p and n+p collisions at GSI to Au+Au collisions at FAIR*. Phd thesis, Johann Wolfgang Goethe Universität Frankfurt a. M., 2009.

[71] Pavish Subramani. *Performance qualification of the DIRICH readout system and development of a novel electron reconstruction scheme for the CBM experiment*. Phd thesis, Bergische Univeristät Wuppertal, 2025.

[72] Peter Fischer. News from SPADIC ASIC testing. https://indico.gsi.de/event/11003/contributions/46411/attachments/32327/41234/2020_08_21_Status_lowres.pptx.pdf, August 2020.

[73] The ATLAS Collaboration. AtlFast3: The Next Generation of Fast Simulation in ATLAS. *Comput. Softw. Big Sci.*, 6(1):7, 2022.

[74] Rahmat Rahmat, Rob Kroeger, and Andrea Giammanco. The fast simulation of the CMS experiment. *J. Phys. Conf. Ser.*, 396:062016, 2012.

[75] Cornelius Feier-Riesen et al. Implementation of fast simulation techniques to simulate enhanced background for low-mass di-electrons. Technical Report CBM Progress Report 2023, Darmstadt, 2024.

Declaration of Academic Integrity

I hereby confirm that this thesis on *Dielectron Performance of the Compressed Baryonic Matter Experiment* is solely my own work and that I have used no sources or aids other than the ones stated. All passages in my thesis for which other sources, including electronic media, have been used, be it direct quotes or content references, have been acknowledged as such and the sources cited.

_____

(date and signature of student)

I agree to have my thesis checked in order to rule out potential similarities with other works and to have my thesis stored in a database for this purpose.

_____

(date and signature of student)